CHAPTER 7

Growth mechanism and microstructure of nanostructured CeO$_2$ and doped-CeO$_2$: (Gd^{3+}, Zr^{4+}) films by CSD

7.1 Motivation

In the previous chapter we have achieved high quality TFA- YBa$_2$Cu$_3$O$_7$ film on processed vacuum deposited CeO$_2$ cap layers. However, for the cost-effective production of high-temperature superconductor applications, physical vapor deposition-derived ceria cap layer may be replaced by MOD grown film, but some problems have to be overcome [139].

Previous studies on epitaxial growth mechanism and microstructure evolution of nanostructured CeO$_2$ films on (100)-YSZ substrates deposited by chemical solution, showed that films grown in a reducing 95%Ar/5%H$_2$ (Ar/H$_2$) atmosphere were inherently granular as a result of a grain growth inhibition mechanisms induced by grain boundary contamination with C, see Fig. 7-1. Incorporation of carbon was caused by inefficient reactions of decomposition of C-rich precursors [38].
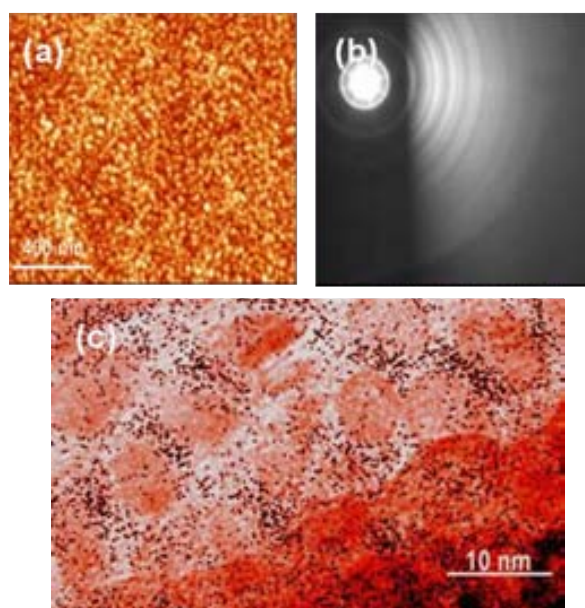
Fig. 7-1 Morphological and microstructural characterization of MOD-CeO$_2$ film grown in 95%Ar/5%H$_2$ atmosphere (a) Typical atomic force microscopy (AFM) image exhibiting a granular morphology with rounded grains. (b) RHEED image exhibiting a ring pattern indicating a disordered surface. (c) EELS mapping of the C distribution through the cross-sectional area, superposed on XTEM image viewed along the <100> direction of the mapped area, showing a nanometric granular mictrostructure [70].

Thermal processing at 1000ºC under oxidizing atmospheric conditions, which enhanced atom mobility in ceria, was required to consume the missoriented grains allowing the epitaxial grains to grow to the surface. This transformation yields to a whole film reconstruction stabilizing (001) polar surface [38]. Indeed, this process allowed us to successfully grow TFA-YBCO films on MOD CeO$_2$ cap layer on IBAD-YSZ/SS substrate [48]. But unfortunately, these post processing conditions are not compatible with Ni-NiW substrates because uncontrolled oxidation of the Ni-alloy occurs. Thus, there is a clear need to develop an alternative route to enhance mobility in our MOD-CeO$_2$ films to unblock granular growth and eliminate C impurities preserving reducing conditions for coated conductor development.

Based on the results obtained on sputtering-CeO$_2$ films described in the previous chapter, our purpose in the following discussion will be to favour epitaxial growth and development of atomically flat terraced surface of CeO$_2$ cap layer in reducing atmosphere. At the same time it would allow us to establish a better understanding of ceria kinetics growth process. In this context it was necessary to look into number of different topics such as diffusion, grain boundary mobility, and chemical properties of pure and doped ceria [183].

7.2 Mobility in CeO$_2$ films

It is well established that the elimination of grain boundary area within the polycrystalline film is the driving force for MOD-CeO$_2$ epitaxial growth [38,176]. For changes in microstructure it is necessary that the atoms could jump from its present site to a neighbouring site, i.e., diffusion. In Fig. 7-2(a) it is schematized an individual atomic jump from grain A to grain B across the boundary. Diffusion process was well described by Fick's laws which in the simplest case relates the flux of particles, J, with the concentration gradient, dC, through a proportionality constant termed D: diffusivity,

$$J = -D\left(\frac{dC}{dx}\right)$$ Eq. 7-1

The diffusivity is a material property and it is perhaps the most useful parameter for characterizing the rate of diffusion. Moreover, the jump frequency or atoms diffusion is a thermally activated process which could be expressed by Eq. 7-2

$$D = D_0 \exp\left(\frac{-Q}{RT}\right)$$ Eq. 7-2

where D_0 is a constant and Q is an experimentally determined activation energy, see Fig. 7-2(b). Notice that the influence of defect concentration, crystal structure and composition of the medium in which diffusion is taking place has not yet been taken into account. In fact Q contains other energy terms such as defect formation and migration energy, which in turn depends on the availability of jumps sites [207].
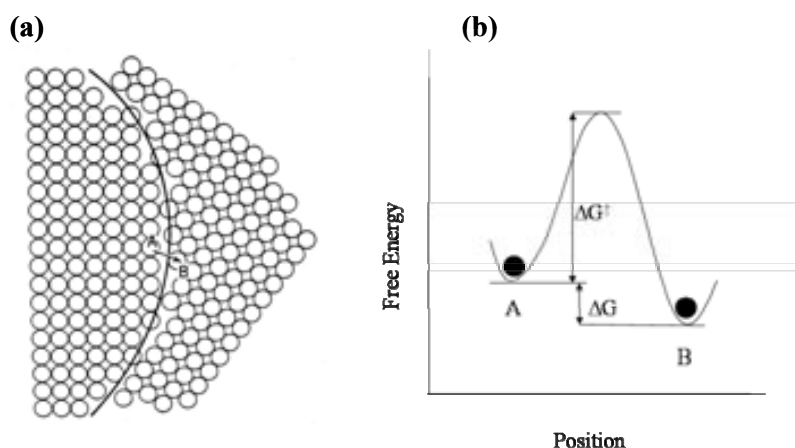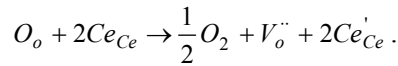

Fig. 7-2 (a) Structure of boundary (b) energy change for atomic jump, ΔG [207]

Referring back to CeO$_2$ material, it is well known that in CeO$_2$ takes place several defect reaction along with charge balance since Ce^{4+} can easily reduce to Ce^{3+}, recall Eq-6.1 :

$$O_o + 2Ce_{Ce} \rightarrow \frac{1}{2}O_2 + V_o^{..} + 2Ce_{Ce}' \, .$$

Consequently, it is expected that the formation of these defects would modify atom diffusion and therefore it could provide us a powerful tool to handle mobility in our CeO$_2$ films. To do that it is firstly required a good knowledge of the mechanisms that control or change this defect reaction.

Applying the law of mass action (assuming no interaction between the various defects) on Eq-6.1 gives,

$$\left[V_o^{..}\right]\left[Ce_{Ce}'\right]^2 P(O_2)^{1/2} = cons\tan t \qquad \text{Eq. 7-3}$$

Considering the above reaction, it is easily understood that oxygen partial pressure, P(O$_2$), will naturally affect the equilibrium by changing the concentration of oxide vacancies [208,209].

Chen and coworkers by investigating the microstructure of CeO$_2$ pellets synthesized at different oxygen partial pressure atmospheres found out an inverse dependence on mobility data [210]. Indeed, they associated enhancement in mobility with oxygen vacancy formation, being consistent with Eq. 7-3. Moreover, this mobility data was used to deduce the diffusion mechanism in CeO$_2$ and they suggested an interstitial mechanism controlled by cation diffusion [211].

The same authors carried out an alternative strategy to increase mobility in CeO$_2$ lattice. They doped CeO$_2$ with metal oxides with lower valencies, e.g. by dissolution of Sr^{2+},Ca^{2+}, Gd^{3+},

$$Gd_2O_3 \rightarrow 2Gd_{Ce}' + V_{\ddot{o}} + 3O_o \qquad \text{Eq. 7-4}$$
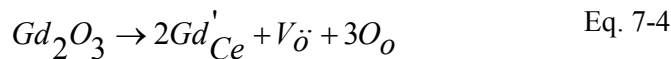
From the above equation it is deduced that by the incorporation of Gd^{3+} into ceria lattice, the dopant agent occupies Ce^{4+} site of host lattice and therefore by charge compensation oxygen vacancies are formed.

In both studies (P(O$_2$) and dopant agent) they found that oxygen vacancies are the key parameter to introduce mobility in CeO$_2$ specimen [211]. In addition, the grain boundary mobility in CeO$_2$ is further influenced by the dopant concentration, valence and ionic radius, as it is further exposed below.

7.2.1 Concentration of dopant

(a) At low dopant concentration mobility is controlled by the diffusion of host atoms across the boundary plane, as is shown in Fig. 7-2(a), the mobility is termed intrinsic. Here, aliovalent dopant can create available sites for atom diffusion by charge-compensating effect and, as a consequence, enhances grain boundary mobility reducing its associated activation energy (Q).

(b) At high concentration of dopants the accumulation of solute ions in the structural core and /or the vicinity of grain boundaries reduce grain boundary mobility to the extent at which the dopants accumulate at the grain boundaries. This is generally attributed to the formation of associations between dopants and oxygen vacancies and /or the ordering of oxygen vacancies [212]. As a result, the solute distribution should be carried along with the moving boundary [213] and the mobility is controlled by solute drag through the lattice [214]. Solute diffusion in the near boundary region is usually slower than the intrinsic diffusion of host atoms across the boundary plane, and becomes rate-limiting. Actually, this is the role of carbon in our MOD-CeO$_2$ films.

7.2.2 Nature of dopant

In choosing the type of cationic dopant, we have taken into account the following facts;
(1) Rare-earth precursors with a trivalent cation are known to be the best possible dopants for ceria because rare-earth elements can easily replace cerium on its regular site due to the closeness in their electronegativity to that of cerium [215].
(2)The structural integrity of the fluorite lattice is best preserved if the lattice parameter of the dopant is the same as that of ceria and there is no variation in the lattice parameter after doping, see Table 7-I. This background suggests that Gd could be an excellent candidate as dopant for CeO$_2$ [183].

Table 7-I Ionic radius and lattice parameter
of M$_n$O$_m$ [211,216]

M	Ionic Radius (Å)	M$_n$O$_m$ lattice parameter(Å)
Ce^{3+}	1.07	3.891 ; 6.059
Ce^{4+}	0.97	5.411
Gd^{3+}	1.05	10.812
Zr^{4+}	0.84	5.14

Finally, it is very important to consider that besides the above strategies to enhance mobility in CeO$_2$, chemical solution deposition and particularly MOD process offers the possibility to modify final microstructure by tuning processing conditions, chemistry of precursors and solvents in comparison to physical deposition methods. The influence of chemistry of precursors have been earlier investigated in our group by Cavallaro [139], therefore we are going to focus on the processing conditions and to probe the influence of solvents.

Prompted by these findings, to surmount the energy barriers for grain boundary mobility, under the particular experimental constraints of the present study, we proposed three approaches:

(a) firstly, it was investigated the influence of slightly oxidizing atmosphere during CeO$_2$ growth, then

(b) it was investigated the influence of solution chemistry precursor [66],

(c) and finally, we studied the effect of trivalent and tetravalent cations on CeO$_2$ growth and microstructure based on studies of defect interaction in boundary mobility and cation diffusivity in CeO$_2$ [210,211].

In all these approaches, CeO$_2$ properties have been studied from the standpoint of cap layer application for YBCO coated conductor. However, YBCO growth on these (doped)-CeO$_2$ cap layers will be described in the next chapter.

7.3   Effect of atmosphere on CeO$_2$ growth

The impossibility of using a pure oxidizing post-processing atmosphere to unblock grain boundaries and to reconstruct CeO$_2$ surface in technical substrates made us find an alternative route to enhance epitaxial growth of CeO$_2$ and stabilize (001) surface as well, by introducing different combinations of oxygen level in the gas process. Based on Eq. 7-3 it was believed that low concentration of oxygen in the carrier gas could be effective to increase mobility in CeO$_2$ lattice and consequently clean carbon from grain boundaries and enhance grain reorientation favouring epitaxial CeO$_2$ growth. CeO$_2$ precursor solution preparation is described in section 3.3.3.1.

Two approaches have been investigated: the one-step and the two-step processes. Briefly, in the two step process, the metal salt solution has been directly heated in oxygen in an initial decomposition step. Once the organic precursor should be completely decomposed, the oxygen gas has been changed to Ar/H$_2$ (to preserve metallic substrate from oxidation) and the film has been subsequently heated to high-temperature crystallization step. Based on weight losses measurements performed in O$_2$ atmosphere, Fig. 7-3 (a), CeO$_2$ precursors are fully decomposed

around 210ºC, whereas in Ar/H$_2$ atmosphere the decomposition ends ~600ºC. Therefore, in our case, a temperature of 300ºC was established for the initial decomposition step and then, precursor films were heated up to 900ºC for 8 hours, (see Fig. 7-3 (b)). Alternatively, in the one-step process (heating profile described in Fig.3-16 (b)), organic removal and crystallization are accomplished in the same processing atmosphere at 900ºC for 8 h: Ar/H$_2$/H$_2$O mixture, (adding water vapour (P(H$_2$O)=2.2%) in the former gas (95%Ar/5%H$_2$)), supported by the good results obtained on processed sputtering-CeO$_2$ in Ar/H$_2$/H$_2$O atmosphere in the previous chapter [217]. The influence of atmosphere on CeO$_2$ epitaxial growth, was investigated in comparison with a CeO$_2$ film grown at 900ºC for 8h in Ar/H$_2$ and in O$_2$ following the work started in the group [139]. At this point we should remark that all samples have been synthesized from the same precursor solution using acetic acid as solvent (section 3.3.3.1).
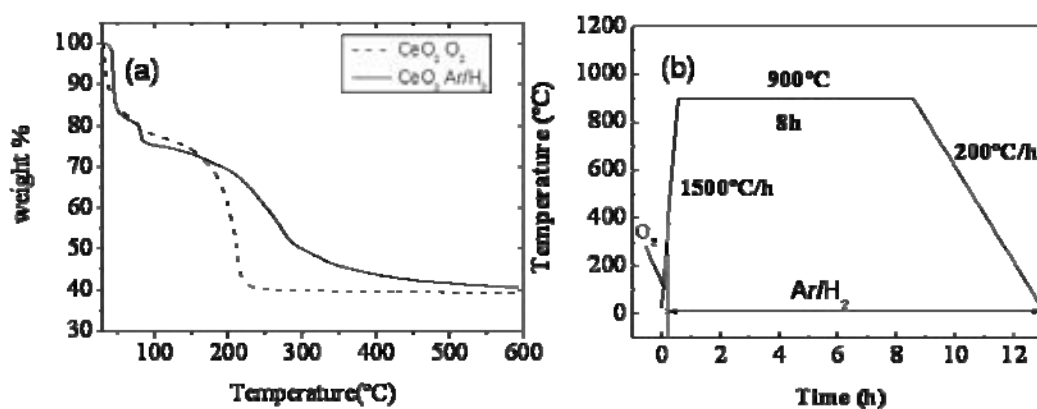

Fig. 7-3(a) TGA of CeO$_2$ precursors dissolved in acetic acid. The heating rate was 300º C h^{-1} between 35ºC and 300ºC and 1500ºC h^{-1} between 300ºC and 600ºC performed in O$_2$ (dashed line) and performed under Ar/H$_2$ atmosphere (straight line). (b) Heating profile of two step processing CeO$_2$.

7.3.1 Structural and morphological characterization

In Fig. 7-4 it is shown XRD θ-2θ scans measured from 25 to 38º. A considerable weak (h00) CeO$_2$ reflections at 2θ = 33.3 º have been detected for the three reducing atmospheres here investigated (Ar/H$_2$, Ar/H$_2$/H$_2$O and O$_2$–Ar/H$_2$). Furthermore, very weak off-axis (111) CeO$_2$ peak was also present, indicating the existence of misoriented grains. In this figure it has been also included a θ-2θ scan from CeO$_2$ processed in O$_2$ for 8h at 1000ºC (in green). Based on XRD and TEM investigations [38], we considered this sample 100% epitaxial and thus, will be referred to as reference sample.

We would like to note that contrary to what predicted Eq. 7-3 and Chen [210,211], oxygen processing atmosphere strongly enhanced mobility in MOD-CeO$_2$ film. This is not surprising considering that our system contains C impurities and this parameter is not considered in the reported bibliography. We suggested that the main role of oxygen in this system is the elimination of carbon and consequently facilitate film reconstruction resulting fully epitaxial film.
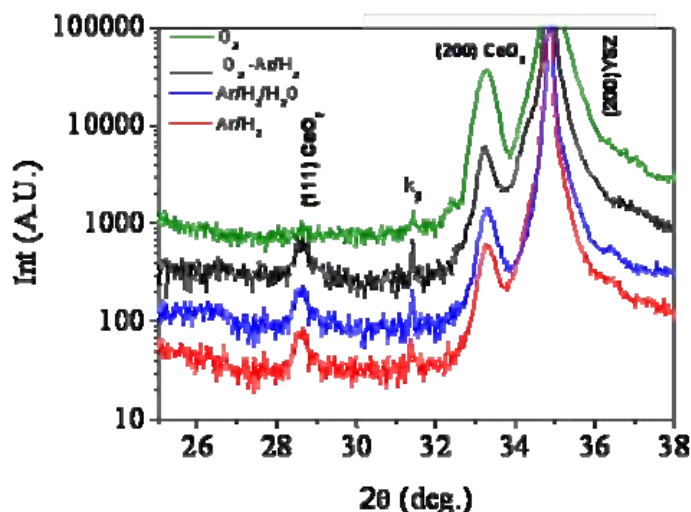

Fig. 7-4 θ/2θ XRD patterns of MOD-CeO$_2$ films grown under different atmospheres: Ar/H$_2$ (in red), under Ar/H$_2$/H$_2$O (blue), under O$_2$ and Ar/H$_2$ (black) and under oxygen (green). All the films were grown at 900ºC for 8 h.

By comparing the area of (h00) CeO$_2$ Bragg line reflection of the different samples here studied with the area of (h00) CeO$_2$ Bragg line reflection from reference sample, we have determined quantitatively the degree of epitaxial fraction of our CeO$_2$ films processed in different atmosphere. We have selected XRD θ-2θ (400) CeO$_2$ peak since it provides higher separation from YSZ peak substrate than (200) CeO$_2$ peak although this reflection is not shown in Fig. 7-4 because its corresponding 2θ value is 69.7 º. Table 7-II displays the evolution of this parameter. It reflects that no significant improvement has been achieved from the viewpoint of epitaxial fraction by incorporation low content of oxygen in the processing gas.

Typical ϕ-scans of the (111) CeO$_2$ reflection from these films showed four peaks 90º apart signalling a unique in-plane orientation (Fig. 7-5). Further investigation of the peaks revealed that consist of two contributions, one broad peak and a superposed narrow one. By contrast, for film grown in pure oxygen atmosphere the broad contribution disappears. Earlier TEM investigations identified the narrow contribution to heterogeneously nucleated epitaxial

grains whereas the broad contribution was attributed to grains nucleated on top of the epitaxial grains with poor texture [139]. These results are well consistent with epitaxial fraction listed in Table 7-II

Table 7-II Summary of percentage of epitaxial fraction for different processed MOD-CeO$_2$/YSZ samples

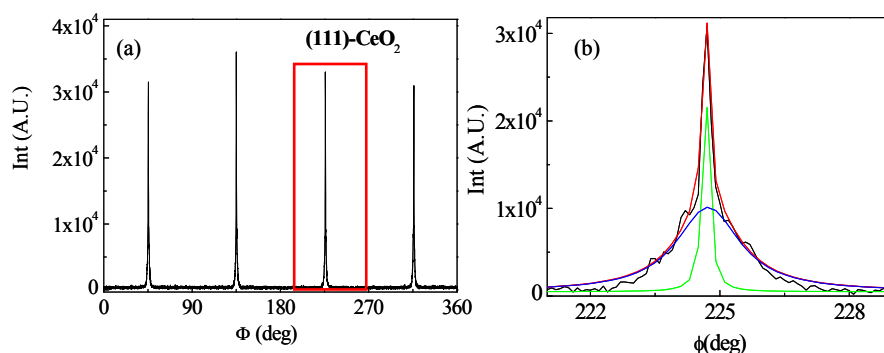| Processing atmosphere	% epitaxial fraction (± 2)
Ar/H$_2$	19
Ar/H$_2$/H$_2$O	20
O$_2$- Ar/H$_2$	28
O$_2$	100

Fig. 7-5 In-plane texture of CeO$_2$ film (a) ϕ-scan of the (111) reflection (b) detail of one peak of ϕ-scan showing two contributions $\Delta\phi_{(1)} = 1.4°$ (blue) and $\Delta\phi_{(2)}=0.2°$ (in green).

In collaboration with IFW-Dresden, further texture assess was carried out by x-ray diffraction pole figure analysis. The (220) CeO$_2$ peak was selected because it provides a clear separation of the YSZ peaks and they also give a high intensity. Pole figure analysis of CeO$_2$ film processed in Ar/H$_2$ and CeO$_2$ film processed in O$_2$ followed by Ar/H$_2$ are displayed in Fig. 7-6. From pole figure of CeO$_2$ grown in Ar/H$_2$ it can be deduced that the grains are not aligned in a preferred orientation. Thus, the film is non-textured, Fig. 7-6(a). From pole figure of CeO$_2$ grown in O$_2$ followed by Ar/H$_2$ it can be scarcely detected four poles among a randomly oriented matrix, therefore it is partially textured, Fig. 7-6(b). They agree well with structural data presented above. These results suggest that low content of oxygen in the processing atmosphere is not enough to enhance mobility in CeO$_2$ film to attain fully epitaxial growth.
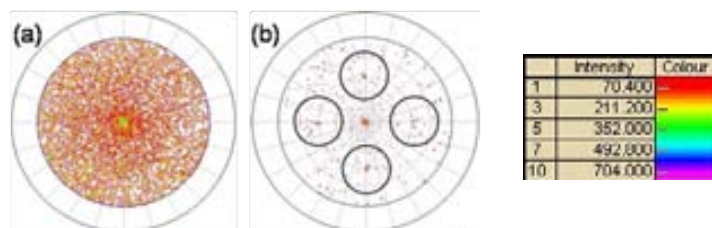
Fig. 7-6 X-ray diffraction pole figures of (220) CeO₂ planes from (a) CeO₂ grown in Ar/H₂ atmosphere and (b) CeO₂ grown in O₂ followed by Ar/H₂ atmosphere.

Structural and morphological properties of these films were further studied by RHEED and AFM analysis. AFM images are shown in Fig. 7-7. All films processed under low content of oxygen presented surface morphology dictated by rounded grains, Fig. 7-7(a-c), far from the terraced one found in samples grown in pure oxygen atmosphere, Fig. 7-7(d) [38]. Surface roughness varied from rms ∼ 2.5 nm for two step growth atmosphere to rms = 6.5 nm for Ar/H₂/H₂O growth atmosphere. Previous studies carried out on CeO₂ cap layer requested atomically flat area rather than low rms value to reach high quality of TFA-YBCO film (chapter 6, [38]). Consequently, we have focused on the quantification of atomically flat area of these films.
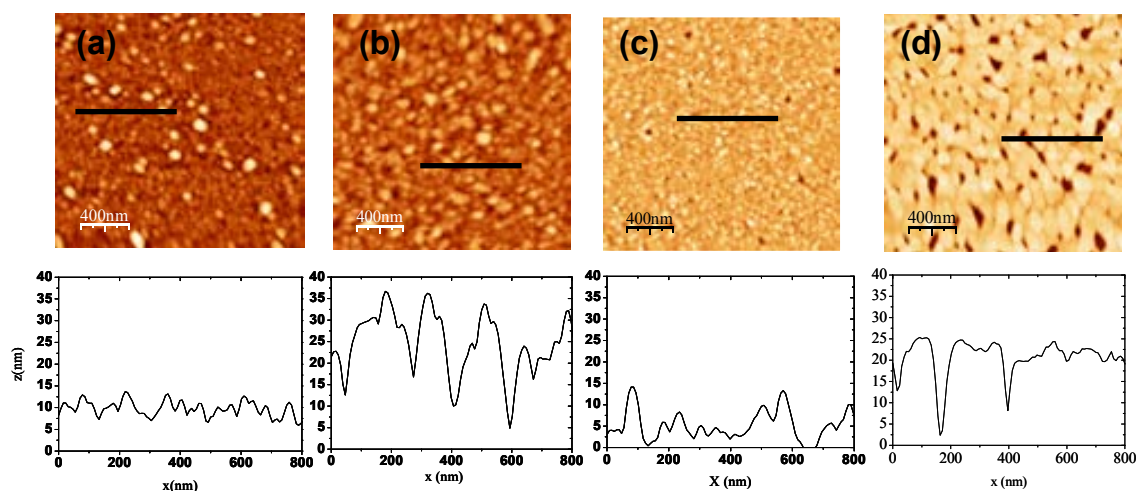

Fig. 7-7 2x2 µm scans of AFM of (a) CeO₂ under Ar/H₂ rms =3,2 nm, (b) CeO₂ under Ar/H₂/H₂O rms =6,5 nm, (c) CeO₂ under O₂ - Ar/H₂ rms =2.5 nm (d) CeO₂ under pure O₂ rms =4.4 nm

We have quantitatively estimated this parameter for the three samples here presented and we have obtained in all cases percentages lower than 13%. In particular, in Fig. 7-8(a) it is shown a typical binary image obtained from CeO₂ sample processed in Ar/H₂ atmosphere. We

166

would like to note that CeO$_2$ film grown under pure oxygen atmosphere shows 70% of atomically flat terraced surface, see Fig. 7-8(b).
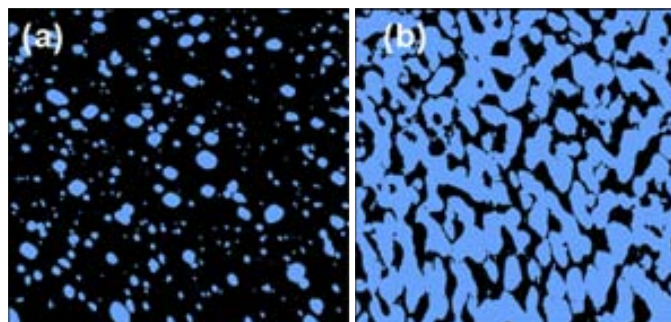

Fig. 7-8 Binary image from AFM topographic image (a) from CeO$_2$ film grown under Ar/H$_2$ atmosphere Fig. 7-7 (a) with 13% of atomically flat area; and (b) from CeO$_2$ film grown under pure O$_2$ atmosphere, Fig. 7-7 (d) with 70% of atomically flat area.

RHEED patterns performed along the <100> and <110> substrate directions are shown in Fig. 7-9. Inspection of RHEED images for ceria grown under Ar/H$_2$/H$_2$O and Ar/H$_2$ revealed a ring pattern, indicating a randomly oriented surface (Fig. 7-9(a) and (b)). These results agree well with the pole figure measured from Ar/H$_2$ processed CeO$_2$ film. In contrast, ceria grown under O$_2$ + Ar/H$_2$ presents a spotty like pattern, Fig. 7-9 (c). It is an indication of textured surface. Even though this result is in apparent disagreement with the pole figure presented above, Fig. 7-6(b), if we look in detail the RHEED pattern in Fig. 7-9 (c), we will find a weak background signal which is attributed to randomly oriented grains. Therefore these two contributions superposed correlate well with the XRD results and to the percentage of epitaxial fraction quantified above.

Finally, by comparison, it has been included a RHEED pattern from reference CeO$_2$ film shown in Fig. 7-10. Spotty pattern identifies textured grains but differing from O$_2$+Ar/H$_2$ processed CeO$_2$ films, here the shape of the spots are elongated, called streaks. This indicates that there are regions in the surface which are atomically flat, i.e. 2D contribution.

As a result, we can identify an evolution from 3D (rounded grains) to 2D surface (flat regions) by increasing the content of oxygen in the former gas confirming the surface morphology observed previously by AFM in Fig. 7-7.

It is interesting to emphasize that CeO$_2$ films with low epitaxial fraction displays surface morphology governed by rounded grains. As far as surface morphology evolutes to terraced morphology the epitaxial fraction strongly increases. Therefore, the investigations here reported on MOD-CeO$_2$ samples allow us to establish a correlation between epitaxial fraction computed

from XRD θ-2θ scan measurements and surface morphology investigated by AFM and RHEED analysis. All along this chapter we are going to explore the validity of this scenario.
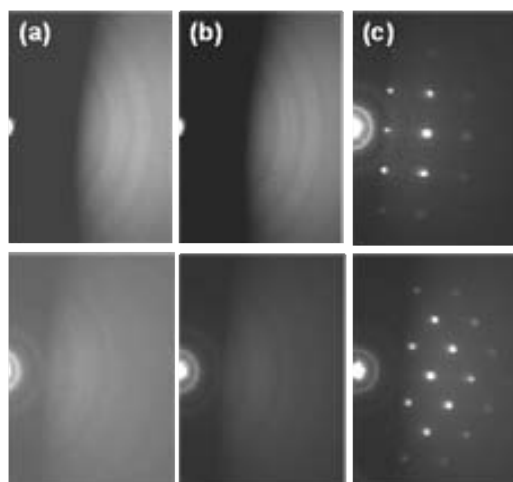

Fig. 7-9 RHEED image of CeO$_2$-MOD buffer layer on YSZ single crystal grown in (a)Ar/H$_2$ (b) Ar/H$_2$/H$_2$O and (c) O$_2$ and Ar/H$_2$ double step process. Images above correspond to <100> direction and images below correspond to RHEED pattern along <110> direction of the substrate.
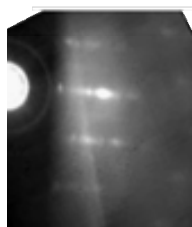

Fig. 7-10 RHEED pattern along the <100> substrate direction of CeO$_2$ film on YSZ single crystal substrate grown under pure oxygen atmosphere [38]

Then, XPS measurements were carried out in order to investigate if the gas processing atmosphere has induced changes in the chemical surface composition that could give us an evidence to understand the blocking mechanism of CeO$_2$ epitaxial growth.

7.3.2 Chemical surface characterization

XPS measurements have been performed in the three samples differently grown after being exposed to air. XPS operating conditions for recording spectra were described in 2.1.3, as well as the processing data acquired.

C(1s) spectra is shown in Fig. 7-11, Ce(3d) is shown in Fig. 7-13 and O(1s) spectra is shown in Fig. 7-14.

In C(1s) spectra, all samples show a main peak at 285.1 eV assigned to C adsorption from environment (contamination carbon, specially hydrocarbons). However Ar/H$_2$ processed ceria, and in less extension Ar/H$_2$/H$_2$O, show a low binding energy feature on the main C(1s) peak, namely C$_{282.5}$ in Fig. 7-11. Chemical shift observed in XPS spectra is the result of the overall electronegativity by which the analysed element is surrounded. Peak shape and peak position of C$_{282.5}$ is very close to the values usually reported for carbide compounds [218], and therefore is likely due to Ce-C bond. Moreover, the existence of CeC$_2$ and Ce$_2$C$_3$ compounds has been known for several years [219]. Based on previous studies performed in our group [38] we suggest that carbon from organic precursors captured (at least) in ceria surface, resulted in carbide formation due to the reducing processing conditions.
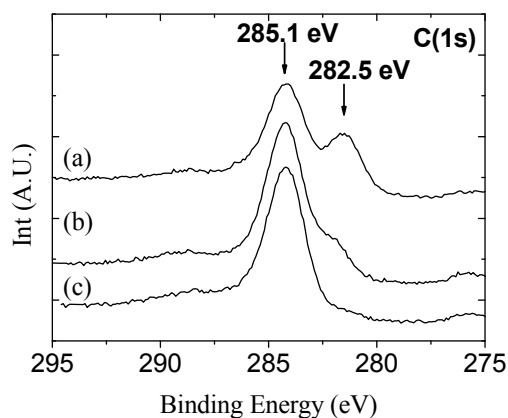

Fig. 7-11 C (1s) XPS spectra of MOD-CeO$_2$ film on YSZ single crystal grown at 900ºC for 8 hours in Ar/H$_2$ (a) in Ar/H$_2$/H$_2$O(b) and in O$_2$ followed by Ar/H$_2$ (c).

We have estimated the percentage of carbide content retained in ceria for each processing atmosphere here evaluated. We calculated the atomic percentage of C, O and Ce with the software package Eclipse using Shirley base line and the following sensitivity factors: Ce3d: 12.06, O1s: 0.66 and C1s: 0.25 (reported in detail in section 2.1.3.1.3). From the above

considerations we obtained a percentage of carbide of 33% in Ar/H$_2$ atmosphere, 15% in Ar/H$_2$/H$_2$O atmosphere and <5% in two step annealing process (i.e O$_2$ and Ar/H$_2$ atmosphere). From these calculations it is clearly seen that in wet atmosphere carbide content has been slightly reduced and in O$_2$:Ar/H$_2$ atmosphere it has been almost completely eliminated (near de surface). Hence, it has been suggested that pure oxygen atmosphere favoured the elimination of trapped carbide.

Since previous studies have shown that by the elimination of carbon, ceria film evolutes from partially to totally epitaxial film [38], here we have investigated the dependence of the percentage of carbide content on the CeO$_2$ epitaxial fraction previously determined by XRD analysis. Fig. 7-12 shows that higher percentage of carbide content in CeO$_2$ films yields to lower epitaxial fraction. These results evidence and support that carbon retained in the film does block the epitaxial growth in MOD-CeO$_2$ films. Thus, we have established that as long as reducing atmosphere was replaced by pure oxygen gas C trace was disappeared and polycrystalline matrix evolutes to epitaxial film.

However from these results we cannot conclude that carbides have been completely eliminated through the whole thickness because the XPS technique is only sensitive to the surface of the films.
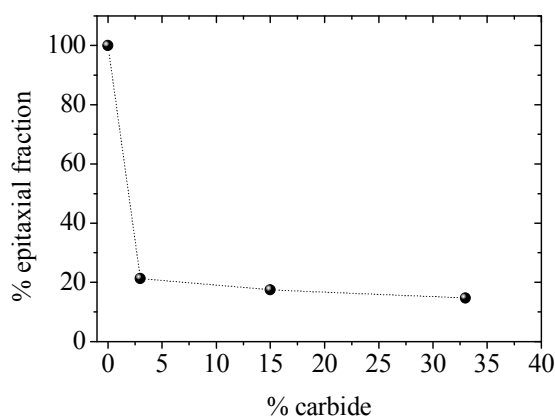

Fig. 7-12 Representation of percentage of epitaxial fraction in MOD-CeO$_2$ on YSZ single crystal on percentage of carbide retained from samples processed at different atmospheres.

Concerning Ce(3d) spectra we observe that Ce^{4+} is the main oxidation state in all samples, however slight contribution of Ce^{3+} from samples grown in Ar/H$_2$ and Ar/H$_2$/H$_2$O atmosphere has been detected, indicated by arrows in Fig. 7-13. For these samples it was determined the percentage of Ce^{3+} following the quantitative approach described in section 2.1.3.1. We have obtained that sample grown in Ar/H$_2$ contains 10% of Ce^{3+}, sample grown in Ar/H$_2$/H$_2$O contains 7% of Ce^{3+} and in sample grown in O$_2$ followed by Ar/H$_2$ contains <2% of

Ce^{3+}. It is interesting to note that samples grown in Ar/H$_2$ and Ar/H$_2$/H$_2$O atmospheres we previously identified the presence of carbide whereas sample grown in O$_2$ followed by Ar/H$_2$ does not. From these results it has been computed the ratio carbide : Ce^{3+} in order to find out if all carbide are bound to Ce^{3+} specimen (Ce$_2$C$_3$). In both cases we obtained higher content of carbide than the expected by evaluating the stoichiometric ratio in Ce$_2$C$_3$. Therefore, we have proposed that carbide specimen might be bound to Ce^{3+} and Ce^{4+}.
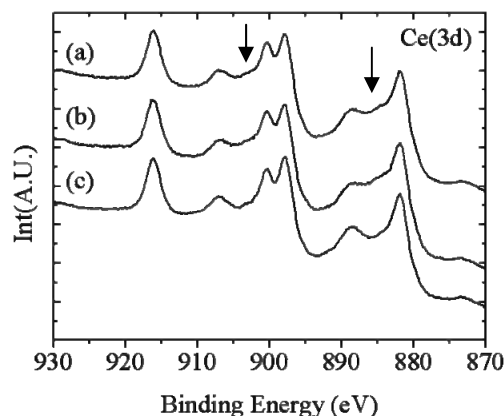

Fig. 7-13 Ce(3d) XPS spectra of MOD-CeO$_2$ film on YSZ single crystal grown at 900ºC for 8 hours in Ar/H$_2$ (a) in Ar/H$_2$/H$_2$O (b) and in O$_2$ followed by Ar/H$_2$ (c).

Fig. 7-14 shows the corresponding O(1s) spectra. Main peak is around 529.7 eV, due to lattice oxygen. It is very similar to the reported value for pure CeO$_2$ [220]. The shoulder peak at about 532.2 eV, as already mentioned in section 6.3.2.4, originates from a combination of a number of species, including surface hydroxyl groups and adsorbed water. It results from the exposure of the samples to air. Thus, from O(1s) spectra, gas processing atmospheres do not cause any remarkable difference.

The combination of these probes allows us to confirm the inefficiency of using only a slightly oxidizing processing atmosphere to enhance mobility to obtain fully epitaxial growth of CeO$_2$ film.
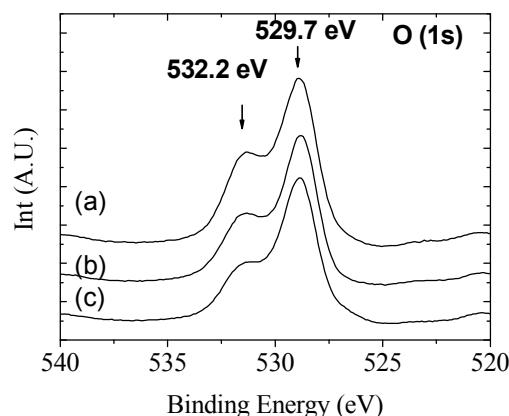
Fig. 7-14 O (1s) XPS spectra of CSD-CeO$_2$ film on YSZ single crystal grown at 900ºC for 8 hours in Ar/H$_2$ (a) in Ar/H$_2$/H$_2$O (b) and in O$_2$ followed by Ar/H$_2$ (c).

In summary, it can be concluded from XRD and AFM investigations that CeO$_2$ grown in Ar/H$_2$/H$_2$O or Ar/H$_2$ atmospheres resulted an untextured film exhibiting a granular surface. These results have been correlated by carbon impurities detected by XPS analysis which probably hinders mobility in CeO$_2$ lattice blocking the epitaxial growth. Using the two step process, low temperature O$_2$ anneal followed by Ar/H$_2$ growth, the carbide content form the surface was minimized. It is very likely that pure oxygen atmosphere enhanced the movement of grain boundaries simultaneously by favouring the elimination of carbon. However, from XRD θ-2θ scan and pole figure measurements and RHEED images it was observed that still some fraction of the film remained randomly oriented which suggested that carbon throughout the film thickness has not been successfully eliminated. The presence of carbon-containing species on or near the surface can inhibit the epitaxial growth of subsequent YBCO layer since underlying layer is not completely epitaxial. Therefore, these growth conditions make this buffer layer not suitable for YBCO CC- fabrication.

7.4 Influence of precursor solution on the final film quality

The presence of impurities (water, acids, C$_x$H$_x$, C$_a$H$_b$O$_c$) is one of the main drawbacks of the chemical methodologies, giving final oxide films with a substantial decrease in their properties, as we previously observed in the preparation of TFA-YBCO and now in CeO$_2$ films. Thus, the search for chemical precursors that produce films with a lower content of impurities

and good reproducibility is an area of permanent interest in the field of the synthesis of metal oxide films.

Here, we proposed the replacement of acetate precursors for propionates by modifying the solvent: glacial acetic acid has been replaced by a mixture 1:1 of propionic acid and isopropanol (see section 3.3.3.2). They give a stable solution for a long time ($\sim$ 3 months versus 2 days of acetic acid based solution). The comparison of XRD θ-2θ scan obtained for CeO$_2$ films derived from both acetic acid and propionic acid is shown in Fig. 7-15. These scans indicate the presence of (h00) peaks for CeO$_2$ films fabricated from both solvents. The CeO$_2$ film fabricated from propionates displays higher intensity of (200) peak and, in addition, it does not show (111) texture reflection. We calculated the percentage of epitaxial fraction from (400) CeO$_2$ Bragg line reflection by using as a reference specimen MOD-CeO$_2$ processed in O$_2$ using acetic acid as solvent. We obtained ~38% of epitaxial fraction. Even though the epitaxial fraction has been improved from original specimen (~19%), it is clear that further investigation has to be carried out.
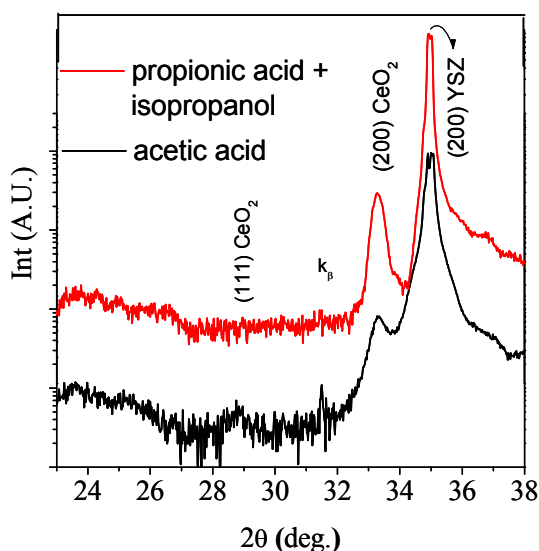

Fig. 7-15 (a) θ/2θ scan of MOD- CeO$_2$ buffer layer on YSZ single crystal grown at 900ºC for 8 h in Ar/H$_2$, from new solvent propionic acid and isopropyl alcohol (in red), and from glacial acetic acid (in black).

AFM image of CeO$_2$ film derived from new precursor solution, shows a uniform general appearance with fine grain size which have a globular shape (~15% of flat grains), Fig. 7-16 (a). The morphology actually appears very similar to that of CeO$_2$ films presented earlier, Fig. 7-7 (a). When surface texture was investigated using RHEED we observed clear spots with a high background, indicative of an inhomogeneous surface (random and good oriented grains) Fig.

7-16 (b), being in well agreement with partially epitaxial film detected from XRD θ-2θ scan analysis. We demonstrate that just replacing acetates by propionates precursors, keeping Ar/H$_2$ atmosphere, ceria surface have changed from untextured to partially textured. This experimental result corroborates the importance of precursor choice because it can drive the microstructure and properties of the film, as we already introduced in section 1.2.3.1.

We suggest that propionic acid and isopropanol solvents besides increasing lifetime solution, may help to promote a decomposition pathway of organic precursor through formation of propylene as a reaction product. As a result, it is likely that this controlled decomposition favours the elimination of carbon content, and therefore, we assume that exist a reduction of the activation energy (Q) associated to grain boundary migration (recall Eq. 7-2). This appears to be the reason of slightly enhancement of epitaxial fraction of CeO$_2$ (38% vs 19%).

However, since there is room to improve CeO$_2$ film quality, in the next section we are going to work on modifying this 'new' precursor solution.
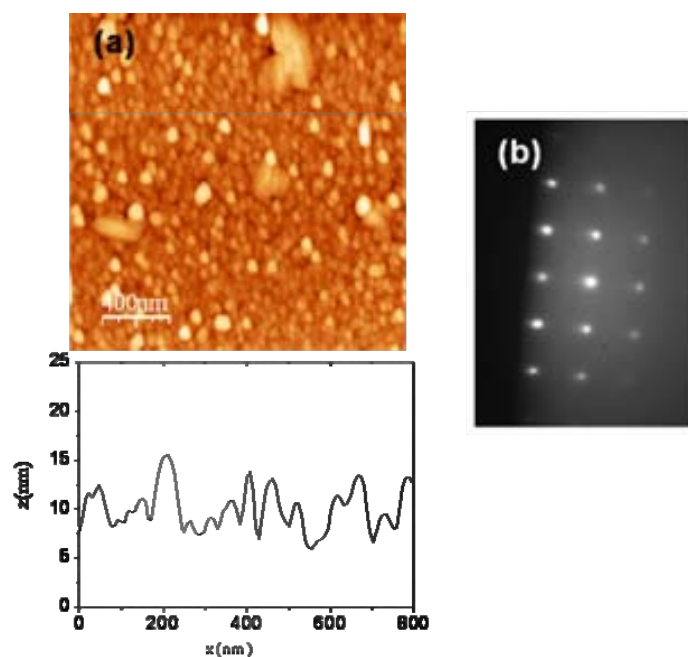

Fig. 7-16(a) AFM image of CeO$_2$ buffer layer on YSZ single crystal deposited from propionic acid and isopropyl alcohol precursors. Rms (2 x2 μm scan) =3.2 nm. Profile scan of the previous AFM image showing granular surface morphology and (b) RHEED pattern along the <100> substrate direction.

As a final remark, it is important to note that recently promising results on nitrates-based precursors have been obtained, also in our laboratory [221]. Little research has been done on producing films from nitrate solutions because of several problems, including the hydroscopic nature of the reagents, the necessity of decomposing nitrates from the film during heat treatment, and difficulty in getting the solution to wet the oxide substrate. However, the addition

of polyvinyl acetates (PVA) makes the solution viscous enough to form a soaplike film and no drop off in YBCO performance has occurred. Further investigation is now on the way.

7.5 Effect of dopant

During the past 10 years, Gd-doped ceria oxides have been of special interest because of their applications to high-temperature fuel cells and oxygen sensors and there are several books and numerous review articles that cover this topic [222,223,224,183]. Recently, other authors have chosen this film as a promising buffer layer for YBCO coated conductor with the aim of avoiding crack formation of CeO_2 [225]. However, J_c value of TFA-YBCO on MOD-Gd doped CeO_2/Ni tape was about 10^5 A/cm^2 at 77K [226]. But in thesis, the aim of doping ceria is the enhancement of grain boundary mobility through oxygen vacancies formed by charge compensation favoring the elimination of both carbon contamination and grain boundaries in the nanocrystalline film [38,211].

7.5.1 Gadolinium doping in CeO_2

The first purpose of this work was to synthesize and optimize gadolinium-doped ceria cap layer on YSZ monocrystalline substrates, as a model system in view of the development of coated conductor architectures based con LZO (pyrochlore)/Ni-NiW substrates, by chemical solution deposition [227]. The results on the structural and morphological properties and also surface chemical modification will be presented and discussed in this section.

7.5.1.1 Optimization of Gd- content

In choosing the right amount of dopant, we must consider solubility data to obtain a true solid solution with cubic fluorite structure and preserve good lattice matching with YBCO. Fluorite structure is very tolerant to dissolution of lower valent metals above 40% [228,215], there is, however, a lot of contradicting information in the literature about the solubility limits.

Therefore, in order to investigate the range of compositions in which good epitaxial growth is obtained, we prepared $Ce_{1-x}Gd_xO_{2-x/2}$ solid solution films with a thickness of 30 nm, henceforth indicated as CGO. They have been fabricated on YSZ single crystal substrates with different Ce and Gd compositions following the procedure described in section 3.3.3.3, i.e, 900ºC for 8h in Ar/H_2 atmosphere, in which propionic acid and isopropanol were used as common solvents. From now, samples will be identified in accordance to the percentage of

gadolinium content, thus x=0.001 as CGO01, x=0.01 as CGO1, x=0.1 as CGO10, x=0.2 as CGO20 and x= 0.4 as CGO40.

7.5.1.1.1 Structural characterization

It is very important to mention that from now to the end of this Thesis XRD analysis have been performed in a PHILIPS PW 3710 MRD from 'Serveis Científico-tècnics de la Universitat de Barcelona (see section 2.2.1).

The results from XRD θ-2θ scan indicated that the films were grown with c-axis perpendicular to the surface of the substrate for all compositions here studied (x=0.001, x=0.01, x=0.1, x=0.2 and x=0.4). For example, in Fig. 7-17 (a) it is shown a typical XRD θ-2θ scan of a CGO10 film. The peaks at 34.93º and 73.80º are reflections associated with the substrate YSZ (200) and (400) respectively as well as the reflections identified as K$_\beta$ in the θ-2θ scan in Fig. 7-17 (a). In addition to the substrate peaks, only two diffraction peaks from the film are observed at about 33.17 º and 69.60 º, which corresponds to the (200) and (400) reflection of CGO, proving some epitaxial growth. The broad feature around 2θ ≈53º is an instrumental artifact. Fig. 7-17 (b) shows the evolution of I(200) of CeO$_2$ Bragg line reflection with percentage of Gd^{3+} incorporated. Maximum degree of epitaxy was observed for CGO10 film.
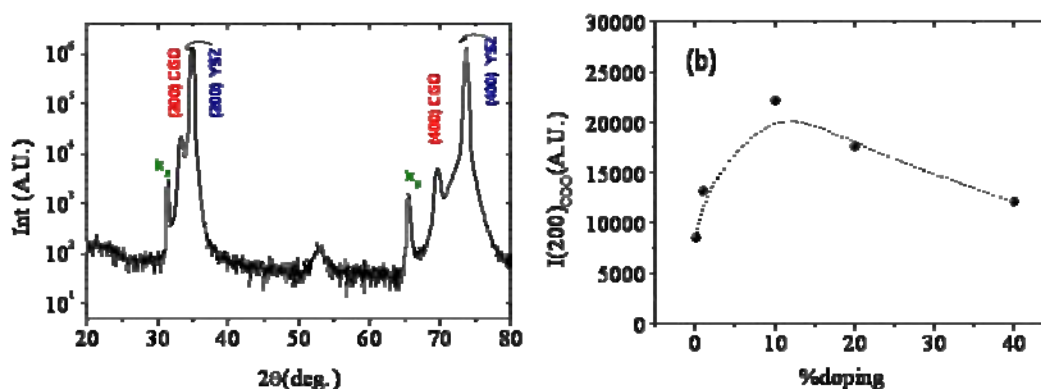

Fig. 7-17 (a) Typical XRD θ-2θ scan for the 10% Gd-CeO$_2$ epitaxial film on YSZ single crystal. The 2θ scan indicates a single phase and highly oriented with cubic fluorite structure like that of pure CeO$_2$. bl-857 (b) (200) CeO$_2$ intensity reflection peak from θ-2θ scan dependence on Gd percentage doping.

We have quantified the percentage of epitaxial fraction in CGO solid solutions by integrating (400) CeO$_2$ peak reflection from θ-2θ scan, as we described in section 7.3.1. It is very important to mention that the reference sample employed to calculate the epitaxial fraction in the previous samples has been changed. Some doped CeO$_2$ films displayed higher epitaxial fraction than pure CeO$_2$ film processed in O$_2$. We anticipate that Zr-doped CeO$_2$ film grown in

O$_2$ atmosphere displays maximum epitaxial fraction and therefore it has been adopted as reference sample. This sample will be further characterized in section 7.5.2.

Table 7-III shows that the epitaxial fraction increases on incorporation of Gd^{3+} reaching a maximum for 10% of Gd^{3+} but then, decreases again at higher Gd^{3+} concentration, following, as we expected, the I(200) Bragg line trend found in Fig. 7-17(b). We would like to remark that doping CeO$_2$ with 10% of gadolinium represents an improvement in the epitaxial fraction of a factor ~ 2 from undoped CeO$_2$ film.

Table 7-III List of the percentage of epitaxial fraction for CGO films

Sample	% epitaxial fraction (± 2)
CeO$_2$	39
CGO01	39
CGO1	38
CGO10	77
CGO20	44
CGO40	24

For CGO films with percentage of epitaxial fraction lower than 44% we have observed bimodal ϕ-scan line shape, revealing the existence of grains with different degree of texture (recall 7.3.1). Instead, CGO10 solid solutions with 77% of epitaxial fraction offers a ϕ-scan from (202) reflection with single and narrow contribution with $\Delta\phi = 1.4°$, see Fig. 7-18.
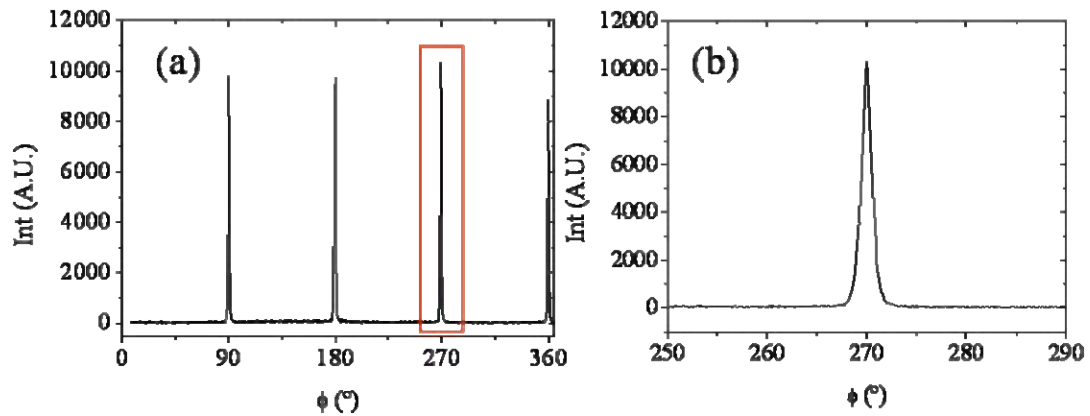
Fig. 7-18 (a) ϕ−scan taken through the (202) reflection corresponding to a CGO10 film grown on YSZ single crystal substrate. (b) detail of one of the four peaks observed in (a)

This effect on epitaxial fraction depending on the percentage of gadolinium content is the first indication that incorporation of gadolinium on CeO$_2$ lattice modifies the activation energy for grain boundary mobility. The dramatic increase of epitaxial fraction from 1 to 10% of gadolinium is believed to be due to oxygen vacancies formed when Gd^{3+} is incorporated in CeO$_2$ lattice, as predicted Eq. 7-4. By increasing defect concentration ($V_o^{\cdot\cdot}$) it is likely that more available jumps sites will be available minimizing the activation energy for grain boundary mobility. Low gadolinium content, 0-1%, might generate few oxygen vacancies to move carbon trapped in grain boundaries and we suggest that C diffusion still governs the mobility of atoms across the grain boundary obstructing the transport necessary to achieve epitaxial film, as was previously described in undoped MOD-CeO$_2$ films.

With increasing Gd content above 10% the decrease in the epitaxial fraction is not explainable in these terms. For a better understanding of the effect of Gd content on lattice and grain boundary mobility, further structural and morphological analysis are required. Therefore, it was calculated the lattice parameter for all Gd concentrations here investigated as could be seen in Fig. 7-19. Lattice parameter was determined from the (400) CeO$_2$ Bragg line reflections of XRD θ-2θ scans.

Like a simple solid solution CGO lattice parameter should follow Vegard's rule, i.e., a linear relationship between lattice parameter and the concentration of the solute. Hence, for comparison, the theoretic Vegard line for Gd^{3+} [229] is also shown in Fig. 7-19. We point out two observations: Firstly, the smaller lattice constant detected even for pure CeO$_2$ films. This modification can be easily understood considering the misfit with the underlying substrate, YSZ (a=5.14 Å) ε= 4.9%. To accommodate such large lattice mismatch, misfit dislocations are probably formed at the interface leading to a semicoherent interface. These results contrast with

perovskite multilayers in which we observed a fully relaxed epitaxy (see Fig. 5-13). Secondly, the calculated lattice parameters fit 'well' to Vegard's law for Gd^{3+}≤ 20 %, but for above 20 % the lattice constant decreases slightly as the Gd^{3+} content increases Fig. 7-19(b). This is in agreement with the report of Tianshu and coworkers [230] who observed similar deviation of the Vegard's law at Gd^{3+} concentrations of 25% in a comparative study on the effect of Gd^{3+} content on CGO ionic conductivities.
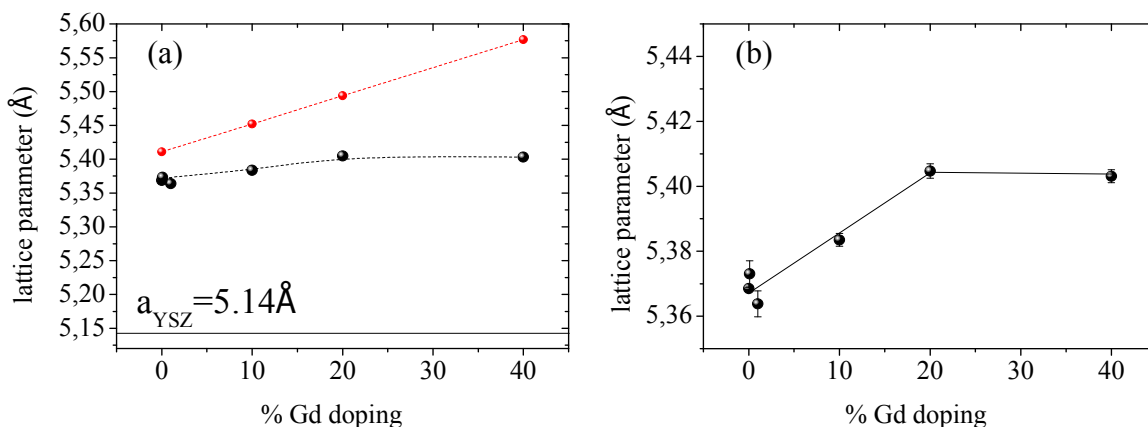

Fig. 7-19 Gd content dependence of lattice constant for CGO cap layer on YSZ single crystal grown at 900ºC in Ar/H$_2$ for 8h (black) compared with Theoretical Vegard's rule (red). (b) Magnification of experimental dependences of lattice parameter on Gd content.

However, it is interesting to note that other authors have observed differences in the compositions corresponding to the maximum lattice constant depending on the sample preparation methods and sintering conditions [228,231,232]. Nonetheless, based on [183] it seems reasonable to assume that the saturation value above 20% determines the solubility limit and thus, above 20% ceria-based solutions might have a mixed structure or a transition structure combined with both cubic type (C-type polymorphism [197]) resulting from the segregation of gadolinium atoms (Gd$_2$O$_3$), and fluorite type [230,213]. In Fig. 7-20 it is shown a representative fluorite –type structure and C-type structure.
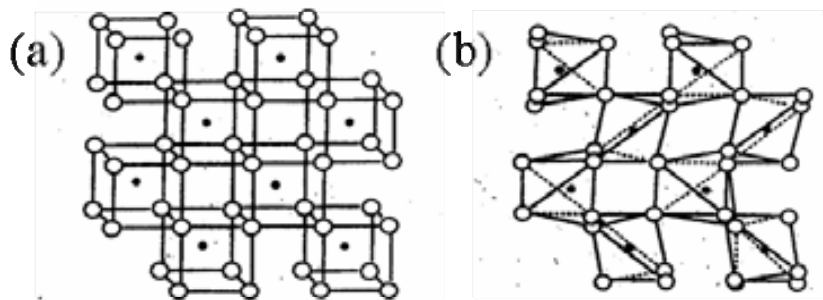
Fig. 7-20 Schematic structure of (a) fluorite-type RO₂. (b) C-type R₂O₃. The solid dots indicate the metal atoms [233].

Unfortunately, XRD analysis cannot confirm the development of C-type structure in ceria-based solutions due to the close relationship between Gd₂O₃ C-type and CeO₂ fluorite structures. It might be more reasonable to suppose that for the composition x>0.2, the lattice constant calculated from XRD patterns provides an average value arising from the fluorite solid solution (dopant ionic size tends to expand the unit cell) and the microdomains of C-type Gd₂O₃ (attractive defect interaction tends to contract the unit cell, it has been proposed the formation of a cluster composed of oxygen vacancies and Gd ions [234]).

For 20% of Gd^{3+} concentration, even though lattice parameter has been increased from 10% of Gd^{3+}, it is still altered in comparison with theoretic Vegard's rule. In addition, we recall that from XRD θ-2θ scan it was deduced a decrease in the epitaxial fraction for this particular composition (see Table 7-III). From these results it is derived that exist a blocking contribution that obstructs (in less extension than CGO40 film) the atomic mobility. Based on reported work we proposed that electrostatic interaction between solute and vacancy could interfere the oxygen diffusivity [213,216]. This regime was already introduced in section 7.2 and it is known as solute drag regime (see 7.2.1). Moreover, these interactions are considered as possible driving force for segregation at higher dopant concentration [235], being consistent with the hypothesis formulated above for CGO40 composition.

In conclusion, the above structural data hints 10% of Gd^{3+} as the most suitable concentration for high quality CGO epitaxial growth. However, for the application of CGO films as cap layer in coated-conductor architectures, the control of surface topography becomes essential. Thus, AFM were performed in these solid solutions. At the same time, this analysis will be complemented with XPS investigations and both would provide more information on the role of Gd^{3+} on CeO₂ films

7.5.1.1.2 Surface morphology characterization

From the AFM images carried out on CGO films shown in Fig. 7-21, we investigated the effect of dopant concentration on its surface morphology. Qualitatively we observed that surface morphology for CGO10, Fig. 7-21(c), exhibits larger and flatter grains in comparison with CGO01, CGO1, CGO20 and CGO40, Fig. 7-21(a),(b),(d) and (e) respectively .
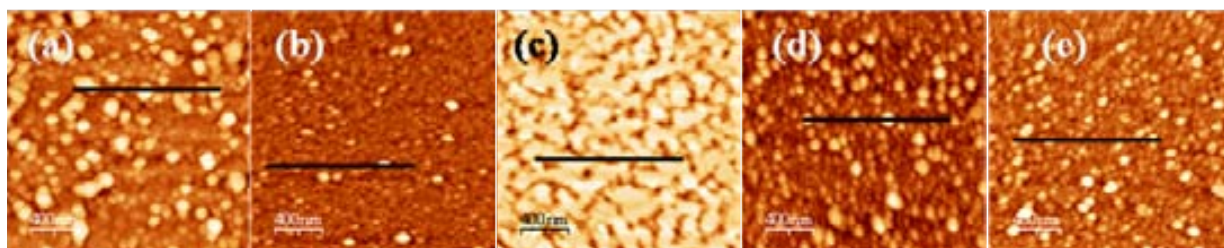

Fig. 7-21 Typical AFM images for CGO solid solution after growth under Ar/H₂ atmosphere (a) x= 0.001 with a rms=5.6nm, (b) x=0.01 with a rms=3.4nm, (c)x=0.1with a rms=4.1 nm, (d) x=0.2 with a rms =5.2 nm and (e) x=0.4 with a rms=2.2 nm. The scan range is 2 x 2 μm.

This trend could be easily distinguished from the corresponding profile scans performed in these topographic AFM images. In Fig. 7-22 are displayed profile scans performed from CGO01, CGO1, CGO20 and CGO40. In Fig. 7-23(a) it is illustrated the profile scan from CGO10. Profile scans in Fig. 7-22 revealed rounded grains and small grain size (their size ranged from 46-61± 2 nm) with number of small humps indicating a very rough surface. This result resembles the well-known granular surface morphology previously observed on undoped CeO₂ thin films, Fig. 7-7. By contrast, CGO10 surface exhibits much bigger and (001)-flat grains (∼200 nm) Fig. 7-23 (a). The valleys are very clear, and the depth is about 10-15 nm. This hillock-like morphology seems comparable with the surface morphology reported in previous chapter for Ar/H₂/H₂O processed sputtering-CeO₂ films.

We have computed the percentage of atomically flat area for these set of samples by applying binarization operator and defining a height threshold around 1.5 nm (3 unit cells of CeO₂), as we described earlier in section 2.1.1. Percentage of atomically flat area for binary images displayed in Fig. 7-24 ranges from ~13 to 18%. For CGO10 films, Fig. 7-23 (b), ~71% of surface area is occupied by flat terraces, only 10% less than sputtering CeO₂ films and it is far more than the other CGO solid solutions here reported. In this case, we speculate that the minimization of (001) surface energy in Ar/H₂ atmosphere could be due to the incorporation of gadolinium. In reality, we suggest that large concentration of oxygen vacancies created by the incorporation of gadolinium reduces the binding energy of surface oxygen ions in agreement with results from atomistic computer simulations [190,191]. However, a more detailed analysis should be required to confirm this assignment.
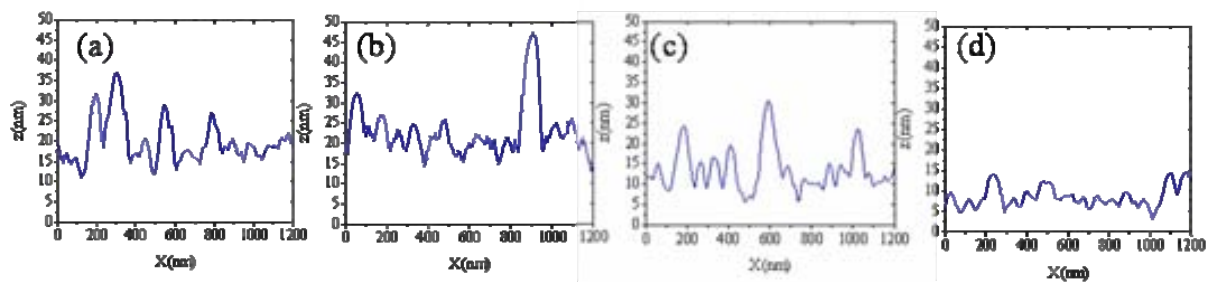
Fig. 7-22 Height profile of AFM topographic images for CGO films with different content of Gadolinium processed under Ar/H$_2$ atmosphere (a) CGO01, (b) CGO1, (c) CGO20 and (d) CGO40.

Fig. 7-23 (a)Profile scan of surface ceria 10% doped gadolinium, grown at 900ºC for 8 h in Ar/H$_2$ performed on Fig.7-12(c). Large (001)-terraces of ~ 200 nm are clearly depicted.

Fig. 7-24 Binary images of the AFM shown in Fig. 7-21 (a) CGO01, (b) CGO1, (c) CGO20 and (d) CGO40.

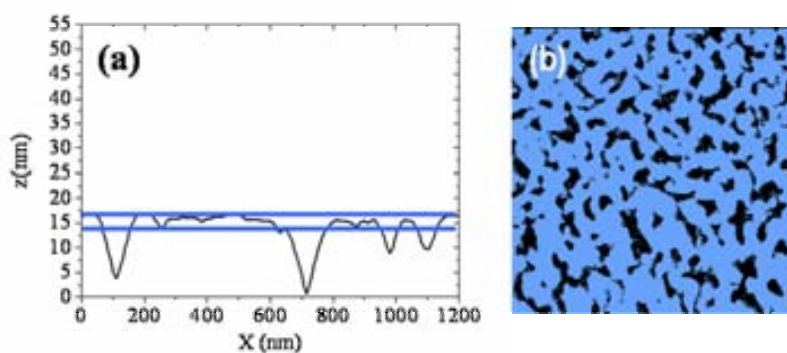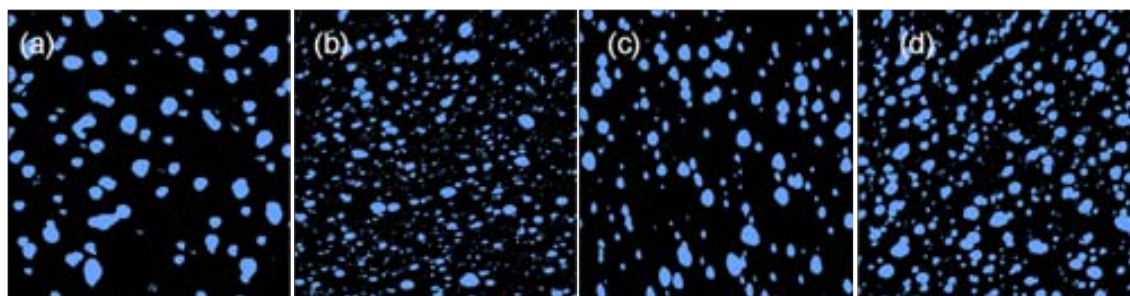Before concluding this section we would like to stress the different grain size and morphology found for Gd-CeO$_2$ solid solution here prepared. Since the driving force for grain growth is the elimination of interfacial energy between grains [207], and grain size distribution for CGO1, CGO01, CGO20, CGO40 is relatively unchanged (recall 46-64 nm versus 200nm in CGO10), it is clear that in these CGO solid solutions impurity effects hinders boundary migration. The nature of these impurity effects could result from sample preparation, i.e. carbon, solute segregation or from solute-vacancy interaction. These results are consistent with XRD analysis presented above in which we detected very low degree of epitaxy.

These proposed impurities have been also detected for other authors in ionic conductivity studies from related systems. For example, Wang and Nowick [236] detected grain boundary resistance at lower dopant concentration due to SiO$_2$ impurities attributed to sample preparation. On the other hand, Chiang and coworkers [237] found changes in bulk conductivity because dopant was extracted to grain boundaries.

By collecting all data from XRD and AFM investigations of MOD-CGO solid solutions, we have found that the percentage of atomically flat area becomes higher when notably increase the epitaxial fraction. It is interesting to remark that this relationship has been already established for undoped CeO$_2$.

At this point it is very important to highlight that based on XRD and AFM investigations we have obtained similar film quality doping CeO$_2$ with 10% of gadolinium in Ar/H$_2$ atmosphere as undoped CeO$_2$ film processed in pure oxygen with the advantage that reducing atmosphere could be transferred to Ni substrates for coated conductors fabrication. Moreover, based on preliminary studies of the group on both MOD-CeO$_2$ [38] and sputtering-CeO$_2$ (chapter 6) in which we found that for high quality TFA-YBCO growth it was extremely important that cap layer displayed high epitaxial fraction and atomically flat terraced surface, we establish that CGO10 solid solution is the most feasible cap layer for subsequent YBCO growth. Consequently, the rest of CGO films which display rounded grains and have low percentage of epitaxial fraction (< 50 %) are ruled them out as a potential cap layers for YBCO growth, i.e. CGO01, CGO1, CGO20 and CGO40. In any case, detailed analysis of TFA-YBCO growth on MOD-CeO$_2$ cap layers will be exposed in chapter 8.

To further investigate the nature of impurities, XPS measurements were carried out because these impurities should modify cerium and oxygen environment and this, in turn, could be detected by shifts in its binding energy (BE). Results are presented in the following section.

7.5.1.1.3 Chemical surface composition

We present here, XPS measurements performed for the CGO films above studied, and which have been compared with undoped ceria.

We acquired data for the O(1s), C(1s) and Ce(3d) core levels with an unmonochromatic Mg K$_\alpha$ source. Gd(3d) emission spectra appears at a binding energy higher than 1200 eV, thus we registered O(1s),C(1s), Ce(3d) and Gd(3d) with Al K$_\alpha$ source (1486.6 eV) because MgK$_\alpha$ is not sufficiently energetic (1253.6 eV). The register with Mg source allows us to compare Ce(3d) feature with previous analysis of undoped Ce(3d) . On the other hand, acquiring data with Al source allows us to examine Gd and quantify the relative atomic percentage. XPS data processing was carried out following description in section 2.1.3. Like in previous measurements, grown samples have been exposed to air before being introduced into the analytical chamber.

C(1s) spectra are shown in Fig. 7-25, O(1s) spectra are shown in Fig. 7-26, Ce(3d) spectra are shown in Fig. 7-27, and finally Gd(3d) spectra are shown in Fig. 7-28.

C(1s) spectra, show the main peak at 285.4 eV originated from the C contamination, Fig. 7-25. Undoped ceria, as we already investigated in section 7.3.2, developed an additional and intense peak at 282.6 eV assigned to Ce-C bond. Gd-doped CeO$_2$ with a concentration of 20% and 40% also present this low binding energy feature, indicating that C has not been effectively removed, Fig. 7-25 (c-d). On the contrary, for CGO10 film C$_{282.6}$ peak is not detected indicating no content of carbide in the surface, Fig. 7-25 (b). Carbide content quantification has been determined by calculating the atomic percentage of C, Ce, O and Gd for the different solid solution composition by using the following sensitivity factors: 0.25, 12.06, 0.66, and 12.93 respectively (see 2.1.3.1). For CGO20 film, the carbide content is 3% and for CGO40 film10 %. We anticipate that TEM analyses have been carried out for CGO10 film to investigate if carbon impurities were in fact fully eliminated throughout the film thickness. Results are presented further on in this section.

Even though carbide content detected for these solid solutions are lower than undoped CeO$_2$ (see 7.3.2), its presence suggests that grain boundary mobility is still blocked and therefore film is not completely epitaxial being consistent with XRD and AFM investigations presented above.
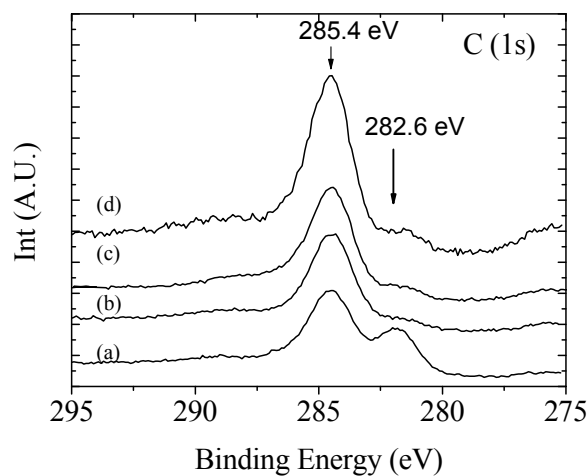
Fig. 7-25 Carbon 1s spectra of CGO grown on YSZ single crystal at 900ºC in Ar/H$_2$ for 8 h. (a) for pure CeO$_2$, spectrum (b) for x=0.1, (c) for x=0.2 and (d) for x=0.4.

Fig. 7-26 shows the corresponding O(1s) spectra. The binding energy of the O(1s) around 529.0 eV is due to lattice oxygen in ceria film. The shoulder peak at about 532.5 eV originates from hydroxyl groups and water adsorbed on the surface due to environment. It is interesting to note that for CGO40, the O(1s) main peak develops a shoulder at higher binding energy, 530.5 eV, Fig. 7-26 (d). This value is close to the O(1s) binding energy of 530.7 eV measured for the Gd$_2$O$_3$ and Ce$_2$O$_3$ compounds [105]. This is because Gd contribution into the CeO$_2$ lattice becomes important, in accordance with modified lattice parameter found above Fig. 7-19(a).
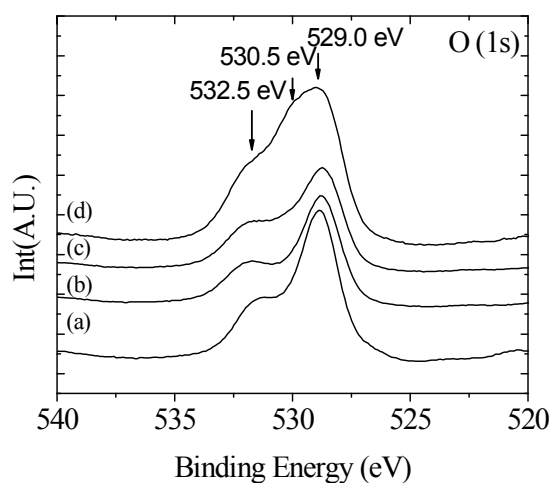

Fig. 7-26 O1s spectra of CGO grown on YSZ single crystal at 900ºC in Ar/H$_2$ for 8 h. (a) for pure CeO$_2$, spectrum (b) for x=0.1, (c) for x=0.2 and (d) for x=0.4.

Gd contribution is also observed in Ce(3d) spectra, in Fig. 7-27. Ceria surface is fully oxidized with no significant changes except for CGO40, Fig. 7-27(d). In this case, cerium environment has been slightly changed. Again, it is due to the Ce^{3+} that appears as a shoulder in Ce(3d) spectra (indicated by vertical arrows in the picture). Ce^{3+} concentration has been computed following the procedure already described in 2.1.3.1 and we obtained a concentration close to ~19%. In this case, based on O1s and C1s spectra results it is suggested that Ce^{3+} could exist either in the form of Ce$_2$O$_3$ or Ce$_2$C$_3$. The mechanism by which the incorporation of significative amount of Ce^{3+} has been occurred is not clear and further investigation is required to clarify its origin.

From Gd (3d) spectra, Fig. 7-28, it is observed an increase in peak area from CGO10 to CGO40. In order to strictly determine if this increase is proportional to the amount introduced in the precursor solution, it has been investigated the dependence of Gd/Ce ratio with theoretical Gd^{3+} concentration. Lineal dependence means true solid solution, otherwise it is a clear indication that segregation occurs. Unfortunately, with three samples it is quite difficult to establish one of these two situations, see Fig. 7-29.

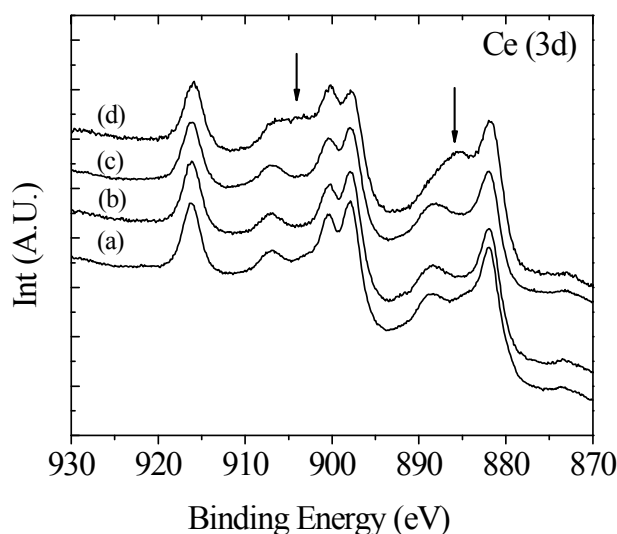Fig. 7-27 Ce 3d spectra of CGO grown on YSZ single crystal at 900ºC in Ar/H$_2$ for 8 h. (a) for pure CeO$_2$, spectrum (b) for x=0.1, (c) for x=0.2 and (d) for x=0.4, vertical arrows indicate the shoulder appeared as a consequence of Ce^{3+} concentration.
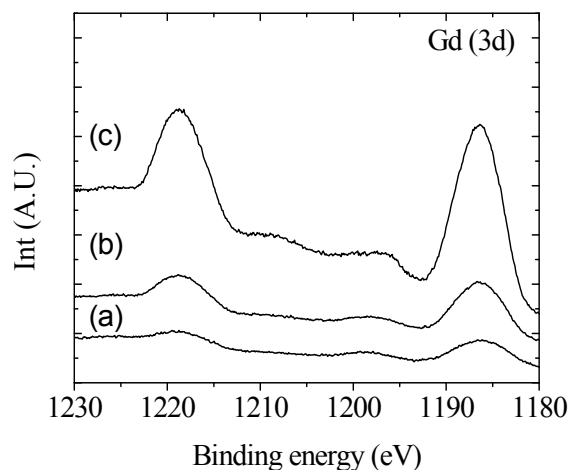
Fig. 7-28 Gd 3d spectra (Al K$_\alpha$) of CGO grown on YSZ single crystal at 900ºC in Ar/H$_2$ for 8 h. (a) for x=0.1, (b) for x=0.2, (c) for x=0.4.
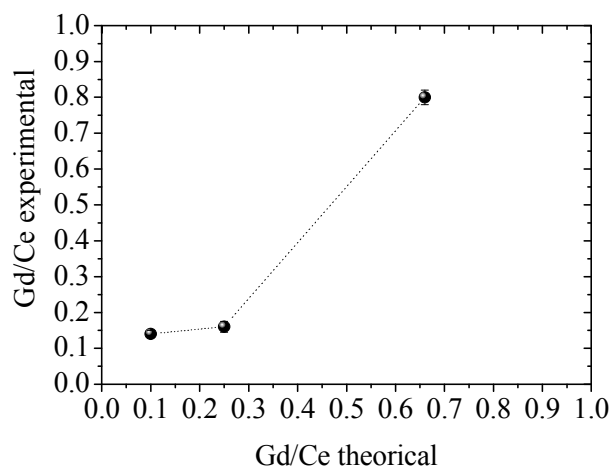
Fig. 7-29 Gd/Ce ratio correlation between experimental and theorical values for Ce$_{1-x}$Gd$_x$O$_{2-x/2}$ solid solutions with x=0.1, x=0.2 and x=0.4.

In conclusion, by XPS measurements we observed that CGO40 spectrum differed from the other analysed samples. Ce and O analysed elements displayed changes in peak shapes resulting of the overall 'charge' by which these elements are surrounded because of Gd. In particular we detected the formation of Ce^{3+} and carbide whereas for CGO10 and CGO20 solid solution, XPS peak shapes for Ce(3d) and O(1s) have not been modified from pure CeO$_2$, only for CGO20 it was detected traces of carbide (~3%).

Thus, it is clear that to enhance grain boundary mobility and simultaneously eliminate C impurities from MOD-doped CeO$_2$ films under reducing atmosphere, a compromise between the carbon content and the gadolinium concentration has to be reached. Gd^{3+} concentration higher than 20% results in dopant-vacancy interaction or even secondary phases segregation that disturb atomic mobility. Thus, these impurities coexist with carbon resulting in final CGO solid solution with low degree of epitaxy. A Gd^{3+} content lower than 10% does not provide enough oxygen vacancies to favour the elimination of carbon simultaneously with grain boundary area and again the final film quality is strongly degraded with an epitaxial fraction lower than 40%. In this study, we found that the threshold between both behaviours occurs at a gadolinium concentration $\sim$ 10% which yields a high epitaxial fraction (~77%) and a atomically flat surface (70%), a promising characteristic for high quality YBCO growth. Thus, we will now focus in the study of surface texture and film microstructure of this CGO10 film.

7.5.1.1.4 Surface texture and microstructure of CGO10 films on YSZ single crystal substrate

To verify surface crystallinity of CGO10 film, RHEED patterns have been recorded (shown in Fig. 7-30). Here the diffraction picture contains slightly elongated spots indicative that the surface film is a transition between 3D to 2D. These results agree with the AFM images in which we detected large and smooth terraces (2D) and valleys between them (3D contribution), Fig. 7-21(c). Note that although we did not detect intense background contribution corresponding to grains randomly oriented, from XRD θ-2θ scan we obtained that this sample is 70% epitaxial. In this case, intense signal for oriented grains disguises 30% of randomly oriented grains. Thus, for our samples, RHEED images complement XRD analysis but do not supply decisive texture information. On the contrary, we have seen that RHEED images are very useful to identify changes in surface morphology.
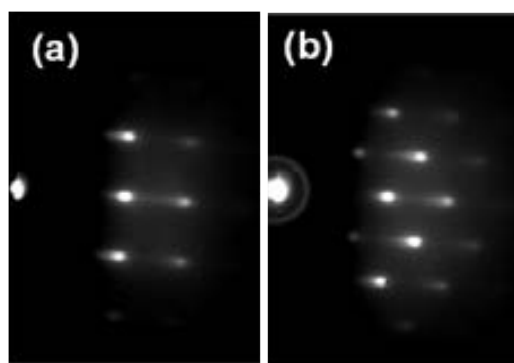

Fig. 7-30 RHEED pattern at 30 keV for a CGO10 cap layer on YSZ single crystal, (a) along the <100> of the substrate direction (b) along <110> of the substrate.

TEM analysis was carried out in order to corroborate the apparent changes film undergoes as detected by XRD, AFM and XPS. Indeed, from the cross sectional images displayed in Fig. 7-31 the terraced surface with grain sizes around 100-200 nm similar to those detected previously by AFM, Fig. 7-21(c), are strongly confirmed. Ledges making an angle of 45º to the film normal are also observed, which according to the <100> viewing direction may correspond either to the {111} or {011} planes. Fig. 7-31(c) is a characteristic <100> SAD pattern that includes YSZ demonstrating the cube on cube epitaxial relationship between the whole film and the substrate.

XTEM images also reflect the stabilization of (001) CeO₂ surface, as previously observed by AFM analysis for MOD-CeO₂ film processed in O₂ [38] and sputtering-CeO₂ processed in Ar/H₂/H₂O (previous chapter).
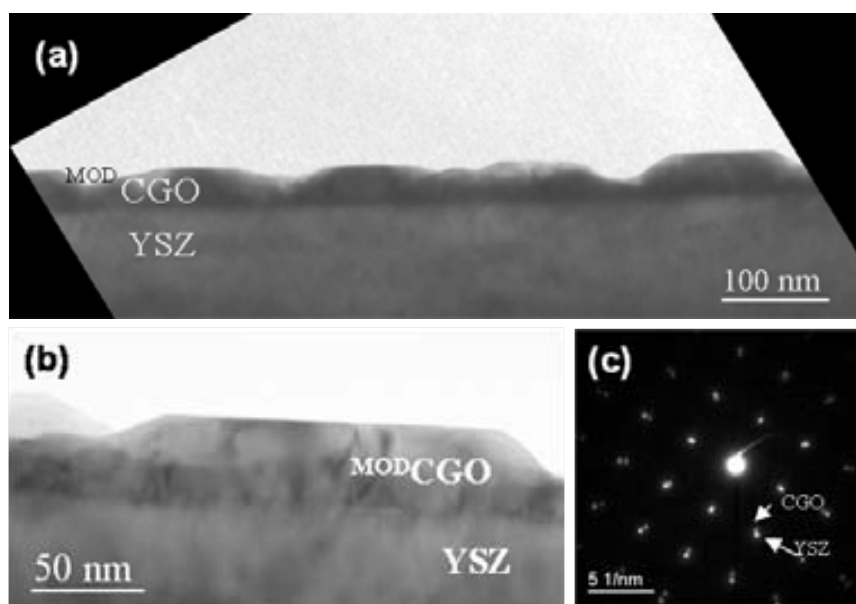
Fig. 7-31 (a) Low magnification XTEM image of a MOD-CGO10 film on YSZ single crystal viewed along the <100> direction. (b) Detail of (a) exhibiting a (001) terraced surface (c) corresponding SAD pattern

Deepen in a high resolution TEM images from this sample, despite in a general view the microstructure is well developed, some grain boundaries with atomic disorder still remain (Fig. 7-32(a)). This high resolution XTEM image shows a detail of two (00l) oriented grains. Moiré fringes indicate the superposition of a third grain misoriented. C distribution for this region was studied by electron energy loss spectroscopy (EELS). Fig. 7-32 (b) compares EELS spectra obtained at a grain boundary and in the bulk. Whereas the bulk is free from C impurities, near the grain boundary low concentration of C still embed grain boundaries. This result contrast with C(1s) spectrum of XPS analysis corresponding of CGO10, Fig. 7-25, in which we did not

detect carbide content. However, this fact can be easily understood considering that C impurities detected by TEM were found far from the surface, whereas XPS is a surface analysis.

From these TEM images it has been exemplified why the epitaxial fraction obtained for CGO10 obtained from XRD analysis was only 70% (it remains 20% of fraction that should be improved). C detected by EELS mapping supports that carbon is still retained in grain boundaries and blocks the epitaxial growth of MOD-doped CeO$_2$ films as we earlier determined in MOD-CeO$_2$ films [38]
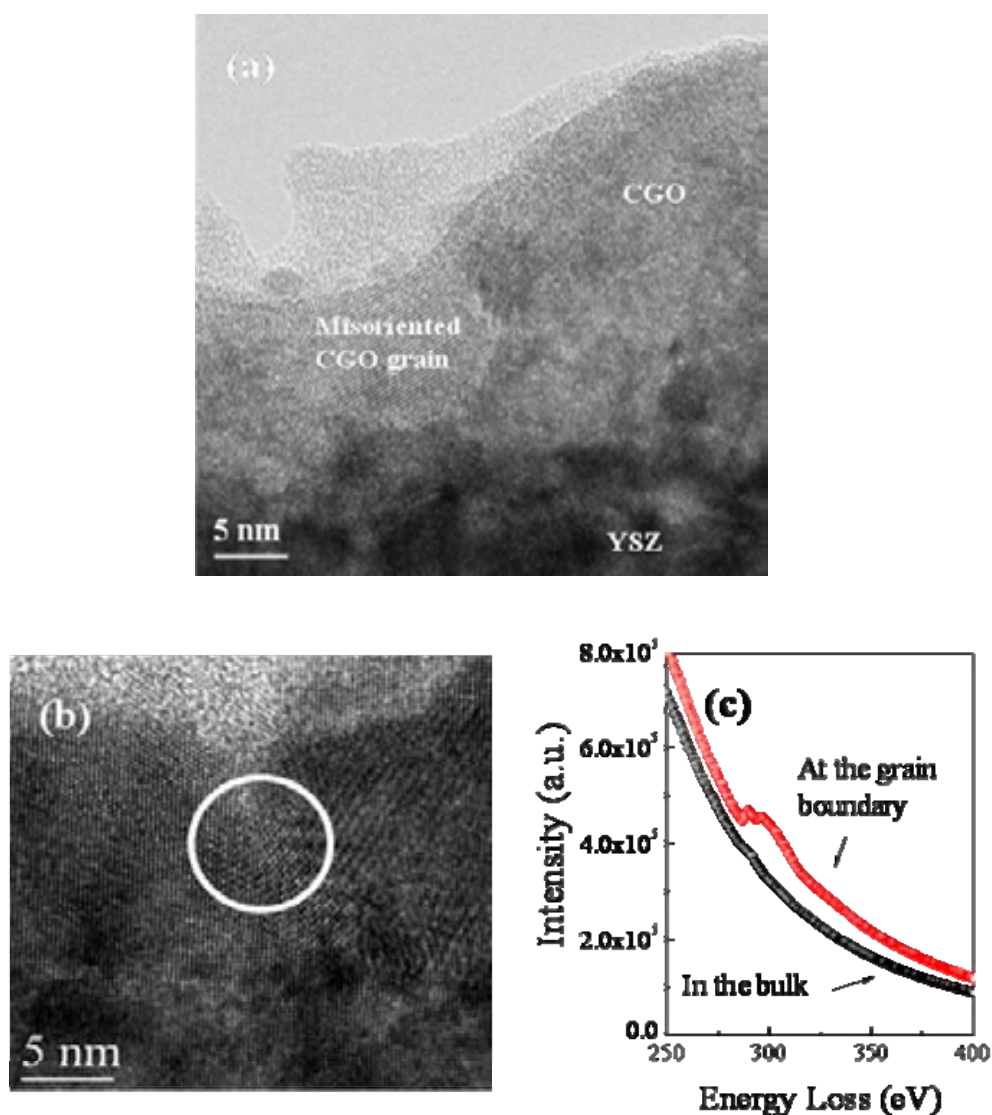

Fig. 7-32 (a) High-resolution XTEM image showing a detail of the grain structure at the topmost region of the film of MOD-10%Gd-CeO$_2$/YSZ film grown at 900ºC for 8 h in Ar/H$_2$ atmosphere. (b) Detail of a grain boundary of two grains of CGO (c) Comparison of EELS spectra obtained from selected area in (b).

7.5.1.1.4.1 Effect of oxidizing atmosphere

Prompted by the remarkable improvement observed in undoped MOD-CeO$_2$ film quality processed in Ar/H$_2$ after oxygen processing due to the elimination of carbon and grain boundaries [38], we also grew CGO10 cap layer with a thickness of 30 nm in oxygen atmosphere, in order to verify if the remaining grain boundaries detected above by TEM could be eliminated and beyond 20% randomly oriented to achieve a highly (100%) epitaxial film.

10%Gd-doped ceria (CGO) on YSZ single crystal was grown using oxygen atmosphere at 900º C for 8 h following the heating profile described in Fig. 3-14(b). We would like to remark that CGO10 film has been synthesized from the same precursor solution as solid solutions described above (section 3.3.3.3).

From the area of (400) CGO peak reflection in XRD θ-2θ scan, we calculated the epitaxial fraction using the same reference sample as previous doped-CeO$_2$ films: Zr-doped CeO$_2$ film grown in pure oxygen atmosphere. From this computation we obtained a value exceptionally high for the epitaxial fraction, 98%, therefore we considered it fully epitaxial. This confirms that when exposed to oxygen atmosphere the epitaxial fraction is being further improved. Actually, we expect that carbon impurities has been completely eliminated, a picture consistent with the previous work [38].

At the same time we have also studied surface morphology by RHEED and AFM techniques. From the AFM analysis, shown in Fig. 7-33, we estimated the percentage of atomically flat surface following the criterion that the height threshold is 1.5 nm. From processing binary image, Fig. 7-33(b), we obtained that 90% of surface area is occupied by flat grains. Additionally, height profile scan, Fig. 7-33 (c), describes (001) terraced surface with a size ranging from 200 to 500 nm. Therefore, from the viewpoint of cap layer applications, oxygen atmosphere has been improved the quality of this buffer in comparison with Ar/H$_2$ atmosphere, however, as we anticipated, this oxidizing atmosphere could not be transferred on coated conductors because it could oxidize them.

The streaky RHEED pattern in Fig. 7-34 is typical from 2D textured surface. We observe that the 3D contribution (rounded spots) detected in CGO10 processed in Ar/H$_2$ has completely disappeared, Fig. 7-30 . This result is in excellent agreement with AFM analysis and both reflects an atomically flat surface. Therefore it is observed that oxygen atmosphere further enhances atomically flat surface.
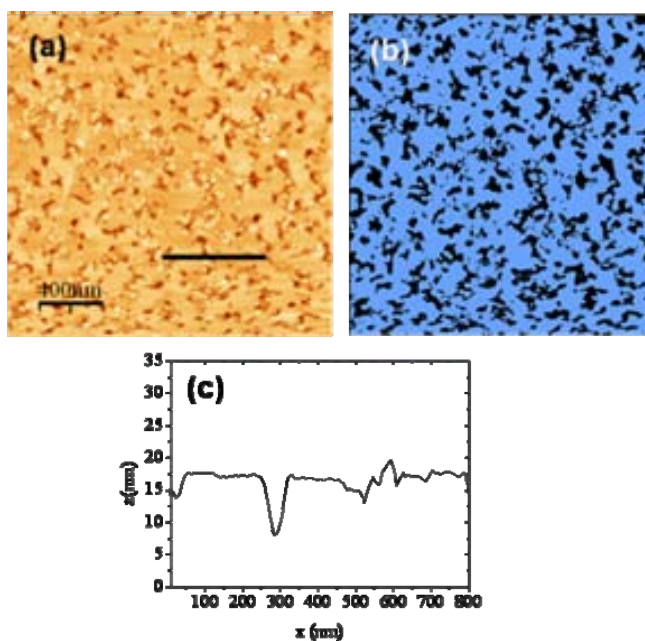
Fig. 7-33 AFM image exhibiting a terraced surface morphology with 90% of atomically flat area of CGO10 fiom grown on YSZ single crystal at 900ºC in O$_2$ for 8 h.
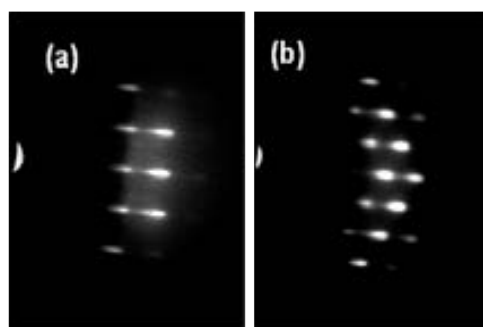
Fig. 7-34 RHEED pattern for a CGO10 cap layer on YSZ single crystal, (a) along the <100> of the substrate and (b) along <110> of the substrate.

In summary, the above results indicate that there exists an evolution to the elimination of grain boundaries (simultaneously with the elimination of C) correlated with an increase of the epitaxial fraction and enhancement of atomically flat surface. Therefore the correlation earlier exposed, first for undoped CeO$_2$ and then for CGO solid solutions, is again accomplished and illustrated schematically in Fig. 7-35. We have demonstrated that many parameters run in parallel to the elimination of grain boundaries: atmosphere, incorporation of dopant agent, concentration of dopant agent and impurities. In fact, by investigating the as mentioned parameters we have successfully demonstrated that the incorporation of 10% of Gd^{3+} in CeO$_2$ film considerably

improve its film quality. Considering that oxygen atmosphere has to be ruled out constrained by the oxidation of the metallic substrate, the most feasible conditions for CGO10 growth are: 900ºC in Ar/H$_2$ atmosphere for 8h. However, in the following section will be investigated the influence of growth temperature and residence time at high temperature.
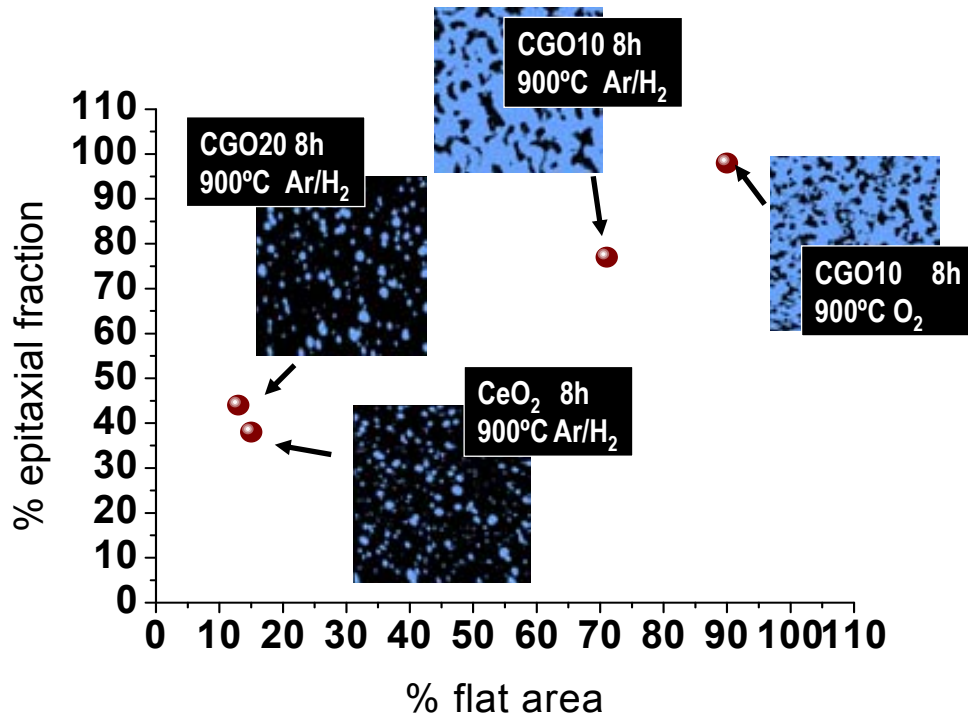
Fig. 7-35 Relationship between percentage of epitaxial fraction and percentage of atomically flat surface from CeO$_2$ and Gd-doped CeO$_2$ grown on YSZ single crystals under the same temperature and time conditions.

Before concluding this section we would like to mention that we have also carried out treatments of CGO10 film at 900ºC for 8 h in Ar/H$_2$/H$_2$O atmosphere, based on the good results obtained in sputtering-CeO$_2$ films presented in section 6.3.2. Unfortunately, film quality is similar to that of pure CeO$_2$ film in reducing atmosphere, i.e., low epitaxial fraction and low percentage of flat area. In Fig. 7-36 it is shown AFM analysis where we observe that surface morphology consists in globular grains ($\sim$21% of atomically flat area and rms $\approx$ 6.5 nm). It is likely that in this case hydroxyl groups do not display any additional role in stabilizing (001)-polar surface. This result is not surprising considering that the nature of the MOD- CeO$_2$ flims strongly differs from sputtering-CeO$_2$ films because of the retention of C from metalorganic precursors.
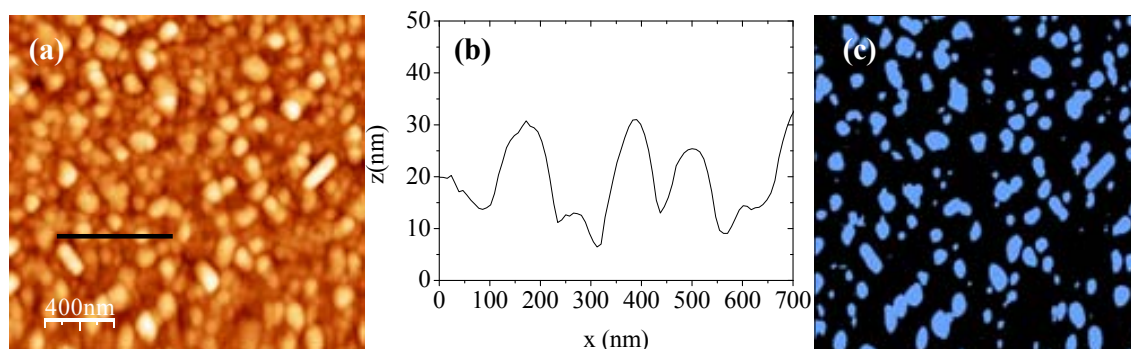
Fig. 7-36 AFM analysis of MOD-CGO10 film grown in Ar/H$_2$/H$_2$O at 900ºC for 8 h on YSZ single crystal substrate. (a) AFM topographic image, rms $\approx$ 6.5 nm (b) profile scan performed on the topographic image (c) binary image (21% of flat grains).

7.5.1.1.4.2 Effect of time and temperature

In an attempt to reduce the required processing temperature (900ºC) and the annealing time (8h) for epitaxial CGO10 films, it has been studied separately the influence of lower growth temperature: 750ºC, and the influence of shorter processing time: 4h. Recall that 30 nm-CGO films have been grown following the heating profile described in Fig. 3-14(b).

XRD θ-2θ scan of samples grown at different times and temperatures on YSZ single crystal with the same thickness, are shown in Fig. 7-37. Only (h00) peaks are observed and no secondary phases are detected. From Fig. 7-37(b) it is deduced different I (h00) CGO Bragg line reflections. Thus, we have estimated the percentage of epitaxial fraction from the area of (400) CGO10 peak reflection and results have been summarized in Table 7-IV

It can be observed that while epitaxial fraction is kept almost constant for samples grown at 900ºC 4h, 900ºC 8h and 1000ºC 8h, CGO10 grown at 750ºC for 8 h shows a noteworthy reduction. From these first structural results it has been deduced that doping ceria with 10% of Gd^{3+} is not enough to obtain highly epitaxial film, growth temperature and time are also critical parameters that govern atomic mobility in CGO films. There is, however, a saturation effect, i.e. very small change is detected by increasing the temperature at 900ºC -1000ºC.
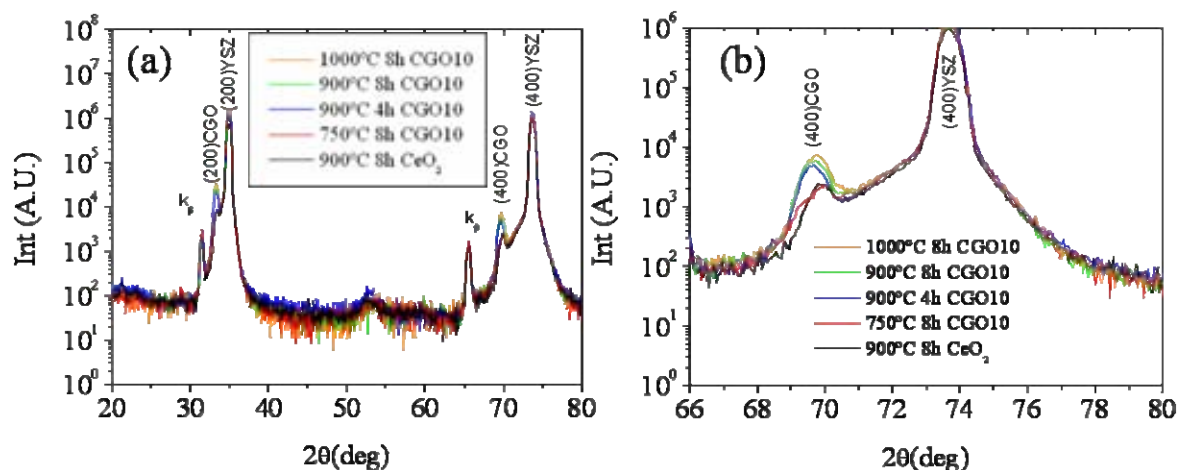
Fig. 7-37 (a) XRD θ/2θ scan of CGO10 films grown on YSZ single crystal substrate under Ar/H$_2$ atmosphere at different time and temperature compared to pure CeO$_2$ film grown on YSZ single crystal substrate at 900ºC for 8 h in Ar/H$_2$ atmosphere.(b) magnification of Fig.7-36 (a) in the range of 2θ values of 66-80º.

Table 7-IV Evolution of the epitaxial fraction of CGO films grown on YSZ at different growth conditions.

Processing conditions of CGO10	% epitaxial fraction (±2)
Ar/H$_2$ 8h 900ºC	77
Ar/H$_2$ 4h 900ºC	73
Ar/H$_2$ 8h 1000ºC	80
Ar/H$_2$ 8h 750ºC	34

Surface morphology analysis for these CGO10 films has been carried out by AFM. In Fig. 7-38 are displayed the AFM topographic images, the corresponding binarized images obtained to quantify the percentage of flatness and, at the bottom a height profile analysis.

CGO processed at 750ºC for 8h surface morphology consists of a granular matrix where grains have similar shape and size but some grains, 12%, homogenously distributed, display larger grain size, see Fig. 7-38(a). By the height profile analysis we detected that larger grains are outgrowth with (001) flat surface. Since no secondary phases were detected from XRD θ-2θ scan analysis, it has been supposed that these hills are a transition morphology from granular to terraced one in which terraces have just started developing.

Sample grown at 900ºC for 4 h, Fig. 7-38(b), surface morphology has similarities to the standard CGO10 film, Fig. 7-21(c). In this case, terraces are smaller (∼100nm) and residual rounded grains with pores observed at 750ºC have not been completely consumed. This could be appreciated from its line scan displayed at the bottom of the AFM image. From the estimation of percentage of flat area, it has been found that ∼ 50% of the surface is atomically flat.

Finally CGO10 film grown at 1000ºC for 8 h displays a fully terraced surface, however, careful inspection of height profile scan reveals that terraces are displayed at different heights (around 5-10 nm), Fig. 7-39(a), and some outgrowths have been settled at the upper terrace Fig. 7-39(b).
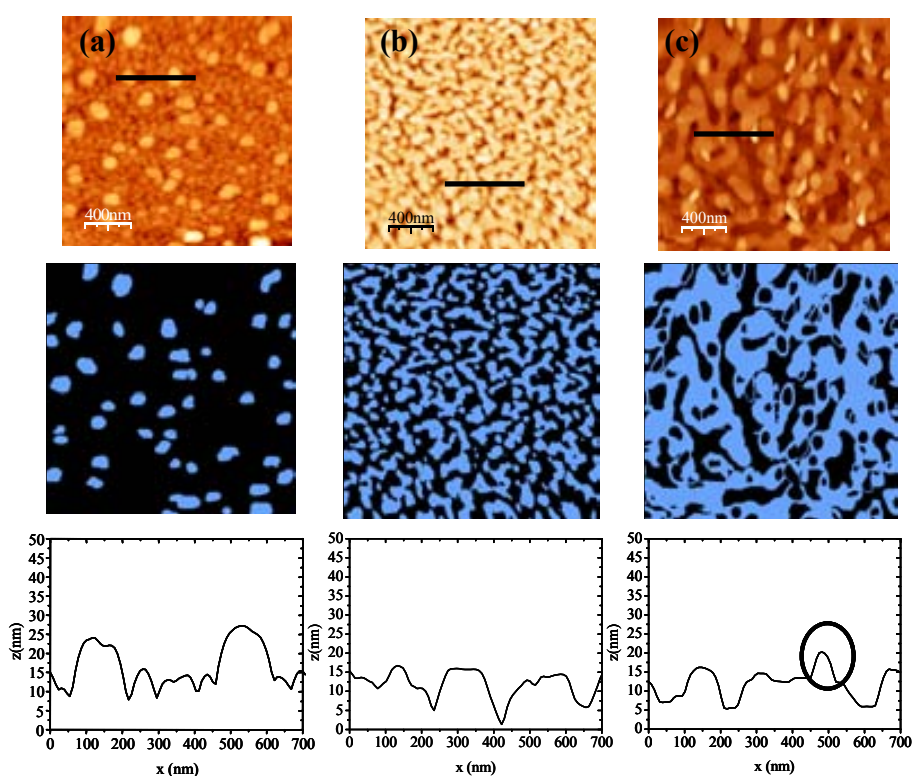

Fig. 7-38 AFM images and its respective scan profile of 10%Gd-doped CeO$_2$ films grown on YSZ single crystal under Ar/H$_2$ atmosphere. At 750ºC 8 h with 12% of atomically flat area (a), at 900ºC 4 h with 50% of atomically flat area (b) and at 1000ºC 8 h, with 59% of atomically flat area (c).
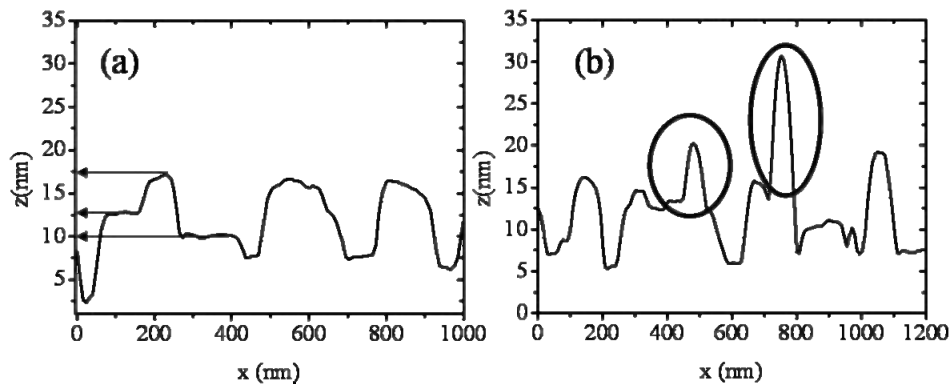
Fig. 7-39 Height profile scans performed on CGO10 solid solution grown at 1000ºC for 8 h in Ar/H$_2$ atmosphere. (a) Exhibits terraces vertically separated by at least 5 nm (b) exhibits outgrowth contributions

It is clear that both contributions will interfere in the computations of atomically flat area for this sample. Therefore, as a first step we should apply a mask in order to subtract the outgrowth contribution (see section 2.1.1). Then, in order to estimate the effective flatness of this film we can only consider the upper floor of terraces, others will be masked. After all these considerations, it results the binarized image displayed below the topographic image, Fig. 7-38(c). This sample has 59% of surface atomically flat.

Collecting all data obtained for these CGO10 films differently processed, we can affirm that improvement in epitaxial fraction is correlated by an enhancement of terraced surface morphology. However, depending on the distribution of these terraces the atomically flat area will not be linearly proportional to the epitaxial fraction, i.e., CGO10 film grown at 1000ºC for 8 h in Ar/H$_2$ although displays similar epitaxial fraction as CGO10 film grown at 900ºC for 8h due to in the former terraces are heterogeneously distributed, effective atomically flat area falls from 71% down to 59%, see Fig. 7-40.

Despite we do not dispose of TEM images for these samples, based on AFM and DRX analysis we suggest that the evolution to high epitaxial and terraced films is strongly related to the elimination of carbon impurities and therefore the grain boundary area. We have observed that besides C contamination, atmosphere and Gd incorporation, growth temperature and growth time also modify the energetic barrier for atomic mobility, however, epitaxial fraction has not been increased beyond 80%, we still have 20% of fraction non epitaxial. We have successfully demonstrated by XRD, AFM, TEM, XPS and RHEED investigations that by tailoring growth conditions and ceria composition (oxygen vacancies) we can modify the activation energy for grain boundary mobility as well as C elimination and obtain high epitaxy and atomically flat CGO10 film.

In terms of YBCO coated conductors applications, the most feasible cap layer is CGO10 film grown at 900ºC for 8 h and Ar/H$_2$ processing atmosphere, since it displays high epitaxial fraction (77%), textured surface and atomically flat area (71%). This proposal will be verified in chapter 8 by depositing YBCO film on top of these CGO10 films.
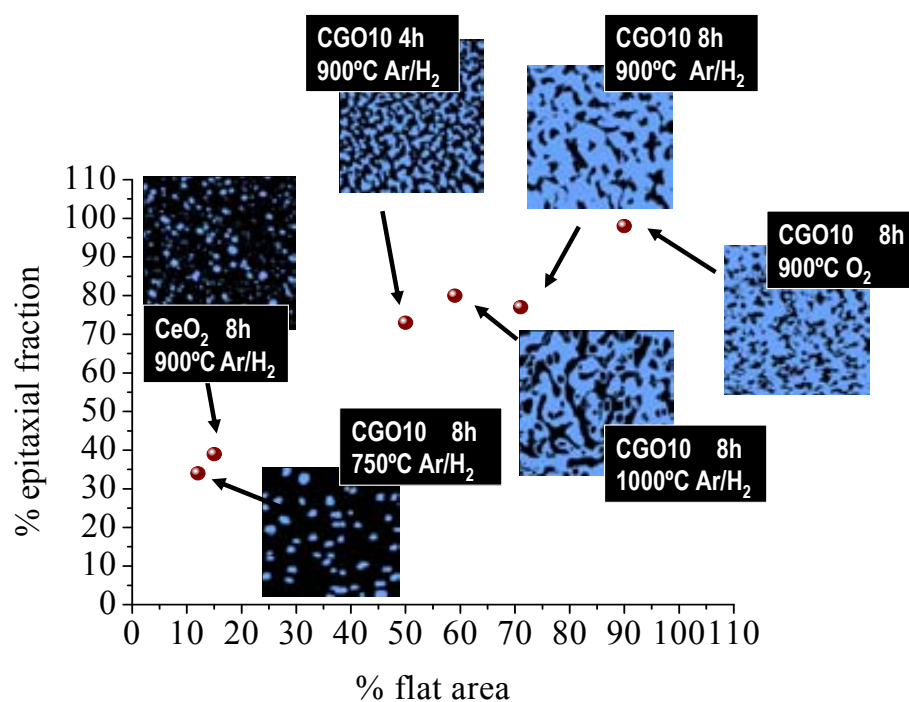
Fig. 7-40 Relationship between percentage of epitaxial fraction and percentage of atomically flat surface from CeO$_2$ and CGO10 films grown on YSZ single crystal at different time, temperature and atmosphere.

7.5.2 Effect of doping ceria with zirconium

In order to complete this study, now we turn to investigate the effect of isovalent dopant into grain boundary mobility: Zr^{4+}. In principle, Zr^{4+} should not modify oxygen vacancies concentration, (see section 7.2), and therefore from this point of view it should be expected a lower grain boundary mobility and a lower CeO$_2$ epitaxial fraction.

7.5.2.1 Structural characterization

Zr-doped CeO$_2$ (CZO) precursor solution was fabricated from propionic acid and isopropanol solvents, following the procedure detailed in section 3.3.3.3. It has been grown on YSZ single crystal substrate under the optimal conditions obtained from CGO films (i.e. 10% Zr^{4+} , 900ºC, in Ar/H$_2$ for 8h). With this composition, CZO10, solid solution presents a cubic fluorite structure [238]. To evaluate epitaxy and crystallinity of this film with a thickness of 30 nm, XRD θ-2θ scan and ω-scan were performed and compared to undoped CeO$_2$ and CGO10 films grown in the same conditions.

Typical XRD θ-2θ scan for CZO10 film only displays the (*h*00) reflections of the CZO and YSZ specimens, and k$_\beta$ reflections associated to YSZ, as can be appreciated in Fig. 7-41.
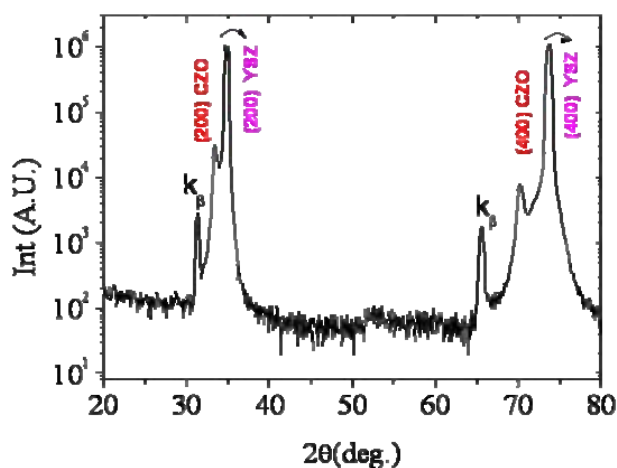
Fig. 7-41 XRD θ-2θ scan for CZO10 grown on YSZ single crystal.

Comparing (400) peak intensity of CZO10, CGO10 and CeO$_2$ films grown under the same conditions, maximum intensity is obtained for CZO10 film, contrary to what we initially expected, Fig. 7-42. Moreover it is noticeable that (400) CZO10 peak reflection has been shifted to higher 2θ values in comparison to pure CeO$_2$, due to ionic radius of Zr^{4+} is smaller than Ce^{4+}, see Table 7-I. Therefore, the Ce-Zr exchange led to a decrease in the lattice constant of the oxide a=5.354Å , in agreement with reported XRD results for bulk powders of these compounds [239]
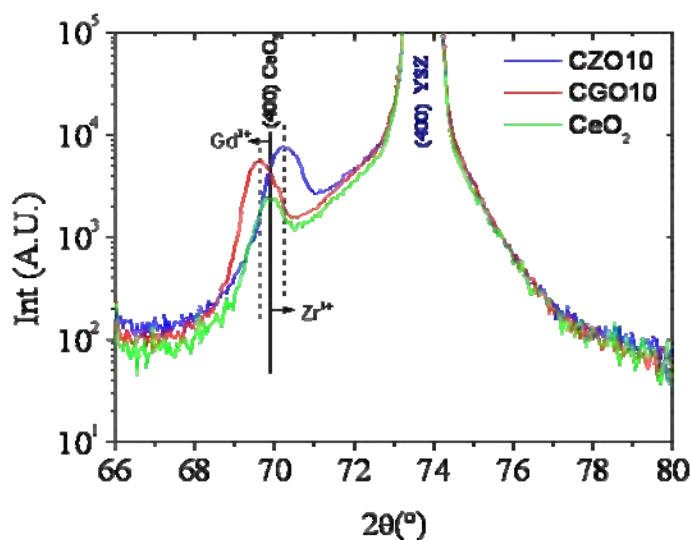
Fig. 7-42 (a) θ/2θ XRD patterns of an undoped CeO$_2$ film, doped with 10% of Gd^{3+} and doped with 10% of Zr^{4+} grown on YSZ single crystal substrate under the same conditions (900ºC in Ar/H$_2$).

We estimated the percentage of epitaxial fraction for this sample from integration A(400) peak reflection using CZO10 film grown in O$_2$ atmosphere as a reference specimen film, described in 7.5.3.4. We obtained a percentage of epitaxial fraction around 50 %. It is interesting to note that despite CZO10 shows an apparent higher intensity from (400) Bragg line reflection, it displays a lower epitaxial fraction than CGO10 film. This can be easily understood by careful inspection of substrate peak position and CZO10 peak position in XRD θ-2θ scan. As they are very close we can not compare directly without proper evaluation of the background. By deconvolution of both peaks, the true area corresponding to CZO10 peak is even lower than CGO10. The apparent high intensity of the (400) Bragg line reflection is therefore attributed to the contribution of the (400) peak of the YSZ substrate. ϕ-scan corresponding to (202) CZO10 film revealed anomalous shape (two contributions), as we already presented in undoped CeO$_2$ film, Fig. 7-5. This result is well consistent with 50% of epitaxial fraction.

7.5.2.2. Surface morphology characterization

In Fig. 7-43 it is shown the analysis of surface morphology performed by AFM of CZO10 film. AFM topographic image shows that surface morphology consists in a mixture of interconnected polyhedral grains with atomically flat terraces defined by (001) planes linked through pores at the ledges of these grains. In this case, 30% of surface is atomically flat and the size of terraces is in the range ∼50-100 nm, therefore, the surface has not developed a well defined terraced topography as the one found by CGO10 grown in the same conditions, Fig.

7-21 (c). But, surface morphology differs from undoped CeO$_2$ film which is also an indication (together with XRD data) that the incorporation of Zr^{4+} has modified the atomic mobility in CeO$_2$ film.
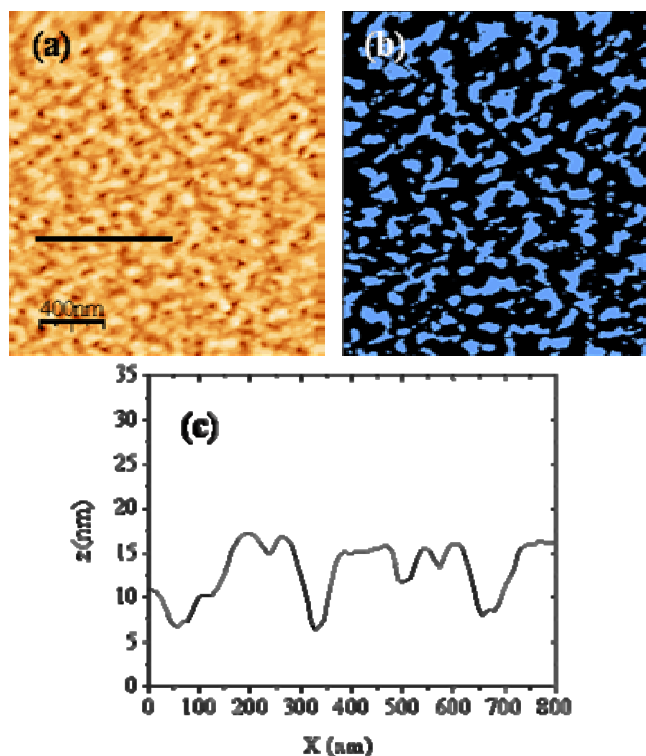
Fig. 7-43 AFM picture of CZO10 grown on YSZ at 900ºC for 8 h in Ar/H$_2$ atmosphere. (b) binary image (c) Profile scan of the topographic image presented in (a)

 RHEED pattern shows spot-like diffraction as a result of textured and rough surface, in short, 3D surface, see Fig. 7-44. This result correlates well with AFM and XRD analysis presented earlier.

   It is very important to notice that even though by XRD analysis we found that films are 50% epitaxial, RHEED pattern does not show a background contribution due to the randomly oriented grains. Therefore we suggest that this contribution might be present but it is masked by sharp spots due to intense textured contribution as we anticipated for CGO10 film. In any case it has to be mentioned that incorporation of 10% of Zr^{4+} under reducing atmosphere, has improved epitaxial fraction and surface morphology from undoped CeO$_2$. Therefore, in contrast to what we initially expected from charge consideration, Zr^{4+} enhanced grain boundary mobility. Thus,

our aim is to find why the incorporation of Zr^{4+} has this beneficial effect on CeO$_2$ microstructure from the view point of cap layer application.
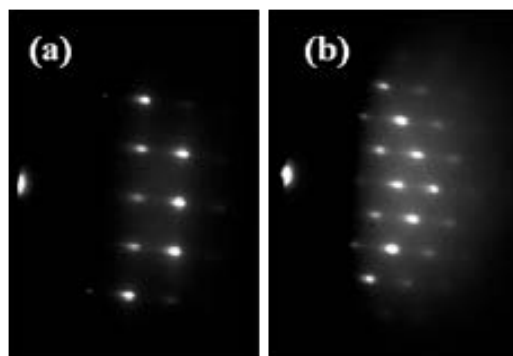
Fig. 7-44 RHEED pattern of CZO10 film on YSZ substrate grown at 900ºC in Ar/H$_2$ for 8h (a) along <100> substrate direction, (b) along <110> substrate direction.

There is a large amount of studies showing that CeO$_2$-ZrO$_2$ system is one of the most appealing mixed-metal oxides due to its important role in the operation of automotive catalysts [240,241]. Balducci and coworkers, by computer simulation studies in CeO$_2$-ZrO$_2$ solid solutions, found that the introduction of 10% of zirconia in ceria lowers the activations energy for oxygen mobility (from ~ 0.6eV for pure CeO$_2$ to 0.1 eV for CZO10) [242]. Although we do not have quantitative data from our samples for direct comparison, our XRD analysis are consistent with an enhanced mobility in ceria by the incorporation of Zr^{4+} based on epitaxial fraction parameter.

The mechanisms for the doping effects of Zr^{+4} remain uncertain and are still a matter of debate but several proposals have appeared. Mamontov and coworkers studied the atomic-level defective structure of nanoscale powders of ceria and ceria-zirconia solid solution using the pulsed neutron diffraction technique and suggested that the smaller ionic radius of zirconium favours the presence of Ce^{3+} ions and associated oxygen vacancies by eliminating the strain associated with their formations [243]. These results are consistent with EXAFS experimental observations from [244] which suggested that structural modifications induced by Zr^{4+} promote the formation of mobile oxygen ions. In this context, it is necessary to look into ceria and CZO10 structure, presented in Fig. 7-45.

Fluorite structure can be described as an array of cations forming the face-centered-cubic lattice with oxygen ions occupying the tetrahedral interstitial sites. The octahedral sites in a perfect fluorite structure are empty (marked by a cross in Fig. 7-45). When Zr^{4+} is incorporated into CeO$_2$, tetrahedral sites are under local atomic compressive stress and it becomes difficult that interstitial oxygen reaches the tetrahedral sites and recombines with vacancies. This could

provide necessary oxygen mobility which is crucial in our samples for grain boundary migration and elimination of C.
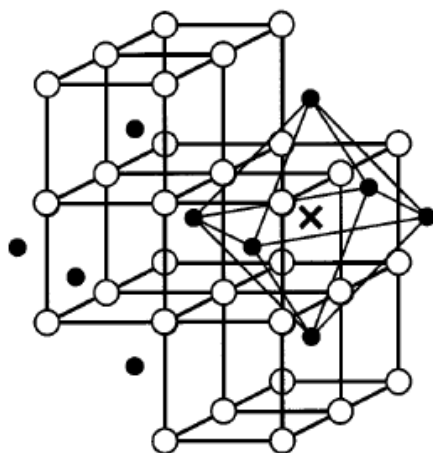
Fig. 7-45 The structure of ceria of cubic ceria-zirconia solid solution. Perfect fluorite structure. Cations (small filled circles) occupy each second interstitial site of the cubes of oxygen ions (open circles). Cation sublattice forms tetrahedral and octahedral sites (one of the octahedral sites is shown). The centers of the tetrahedral sites coincide with the vertexes of the oxygen cubes, while those of the octahedral sites (marked by a cross) coincide with the centers of the oxygen cubes.

7.5.2.3 Chemical surface composition

In attempt to verify if Zr^{4+} favors the presence of Ce^{3+} in our samples, which in turn will allow us to roughly explain changes produced in CZO10 films, XPS analysis was performed.

The surface chemical composition of the CZO films was investigated from Ce(3d), O(1s), C(1s) and Zr(3d) core level x-ray photoelectron spectra. It is important to remark that from the survey spectrum we do not have identified Y indicating that we do not have uncovered substrate areas and therefore the Zr(3d) signal is entirely from the film. These spectra have been acquired by the conditions described in section 2.1.3. Binding energy correction and area calibration had to be made in all cases as in the previous systems here studied. According to earlier XPS results, all spectra will be strongly influenced from environment (CO_2, hydrocarbons, H_2O adsorption).

C(1s) spectra presents a single peak at 285 eV indicating, as expected, the incorporation of typical hydrocarbons impurities, Fig. 7-46(a). Surface carbide contribution is not observed in C(1s) spectrum. This is another indication that Zr^{4+} into CeO_2 favoured the grain boundary mobility.

O(1s) presents a main peak at 528.8 eV corresponding to structural O-Ce energy. Low intensity shoulder at higher binding energy is formed by the as-mentioned oxygen from the environment (H_2O or OH^-), namely $O_{532.1}$ in Fig. 7-46(b).

The shape of the Ce(3d) spectra, indicates the presence of Ce^{3+}, marked by arrows in Fig. 7-46(c). We have quantified the Ce^{3+} content from the total Ce as described in section 2.1.3.4 and from this compute it figures out 10% of Ce^{3+}. Contrasting this result with CGO10 surface chemical composition reported above see Fig. 7-27, we note that in Ce3d spectrum from CGO10 solid solution it is not detected formation of Ce^{3+}. Thus, even the pathway formation of Ce^{3+} in CZO solid solutions is still not understood, this result are consistent with mechanism described by Mamontov and Balducci [242,243].

Finally the presence of Zr in the film was detected from registering the binding energy of the Zr(3d) core level. Peak shape and peak position are very similar to the reported value in previous work on 10%Zr-CeO$_2$ thin film on (100) SrTiO$_3$, Fig. 7-46(d) [245]. It has been estimated the atomic ratio Zr/Ce from the Zr3d and Ce3d peaks areas and by using the corresponding sensitivity factors (section 2.1.3.1.3). We obtained Zr/Ce= 0.12. This calculated ratio is close to that introduced in the precursor solid solution.
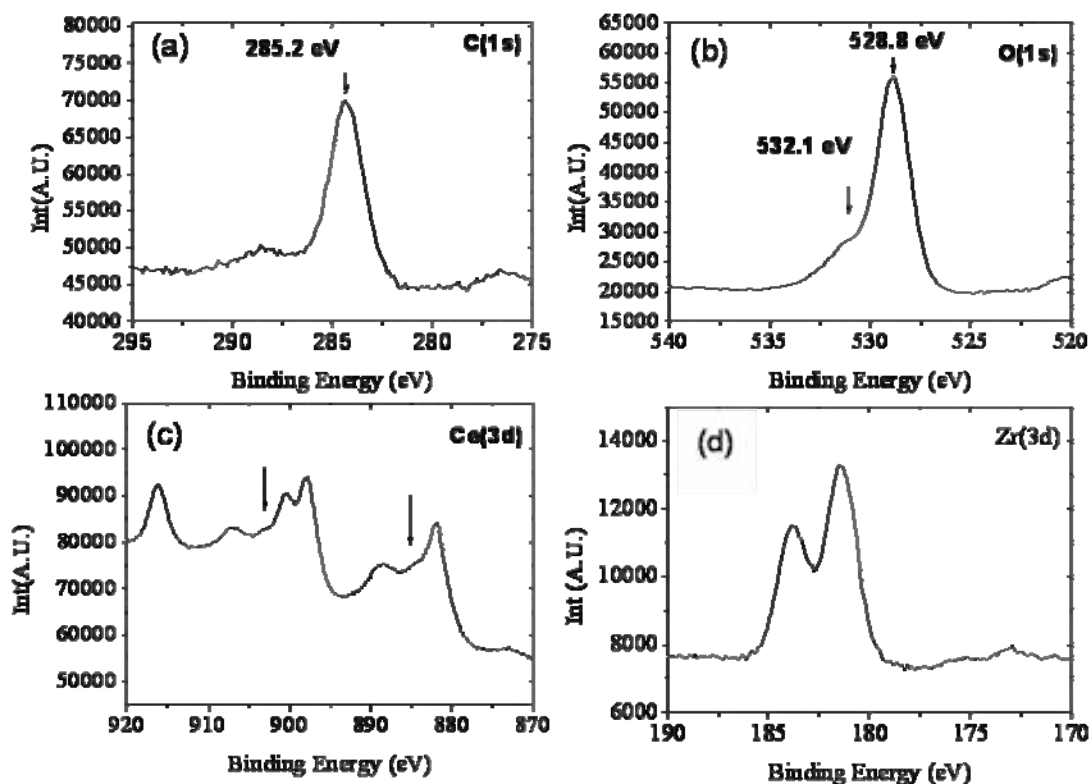
Fig. 7-46 High energy resolution XPS spectra of the C1s (a), O1s (b), Ce3d (c) and Zr 3d (d) for the epitaxial CZO layer on (100) YSZ single crystal.

In conclusion, the incorporation of Zr into CeO$_2$ lattice introduces the formation of 10% of Ce^{3+} on CeO$_2$ surface composition. Therefore, we suggest that the incorporation of Zr^{4+} in our CeO$_2$ films favors grain boundary mobility through Ce^{3+} formation and the associated oxygen vacancies formation. It is interesting to notice that both CGO10 and CZO10 enhance grain

boundary mobility by oxygen vacancies, but the mechanisms by which they form are completely different and the final film present different degree of epitaxy and surface morphology.

7.5.2.4 Effect of oxygen atmosphere

With the purpose of possible improvements in surface morphology and texture quality of CZO10, as we already observed by CeO$_2$ and CGO10 system, CZO10 film has been grown on YSZ single crystal at 900ºC for 8 hours in oxygen atmosphere.

Comparison of XRD θ/2θ patterns of CZO10 solid solutions grown under oxygen and under Ar/H$_2$ atmospheres are shown in Fig. 7-47. They revealed a clear increase of the intensity of the (h00) peaks when CZO10 is grown in oxygen atmosphere. From Fig. 7-48 we appreciate that in-plane texture was improved changing the processing atmosphere resulting a single and sharp contribution with Δϕ(202) =1.1º.

A(400) peak reflection of CZO10 has been calculated by deconvolution of the (400) peak of substrate and (400) peak of film. We obtained maximum area and therefore this sample has been considered 100% epitaxial. This sample, actually, has been utilized as reference specimen for calculations of epitaxial fraction of all other doped-CeO$_2$ here studied as we already anticipated.
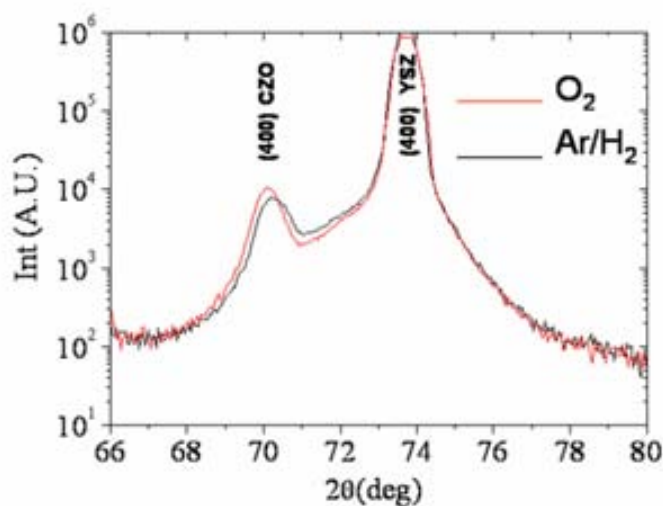
Fig. 7-47 θ/2θ scan in the 2θ range of 66 to 80º. In red it is depicted the CZO/YSZ film grown under oxygen and in black it is depicted the film grown in Ar/H$_2$ atmosphere.
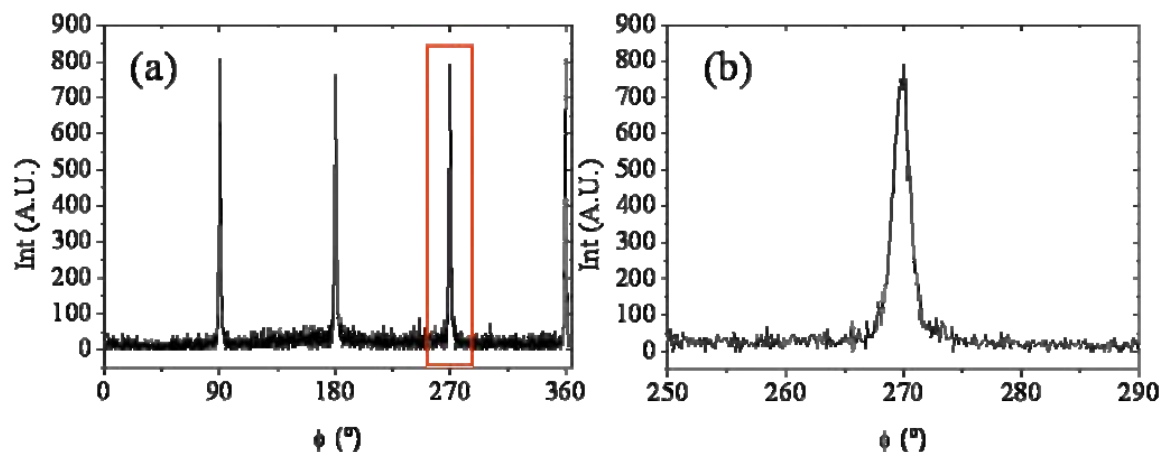
Fig. 7-48 XRD φ-scan of (202) reflection from CZO10 film grown on YSZ single crystal substrate (b) magnification of the peak centered at 270º in (a).

It is likely that by using pure oxygen atmosphere we have successfully eliminate grain boundaries and carbon impurities in MOD-CZO film, thus being well consistent with previous results carried out on MOD-CGO and MOD-CeO$_2$ film under pure oxygen atmosphere.

RHEED pattern shows streak-like diffraction spots indicating a textured surface with very flat islands. There are even indications of 'real' RHEED patterns (see view parallel <100>) resulting from a 2D diffraction case. Therefore, the pattern might be described as 2D surface, Fig. 7-49.
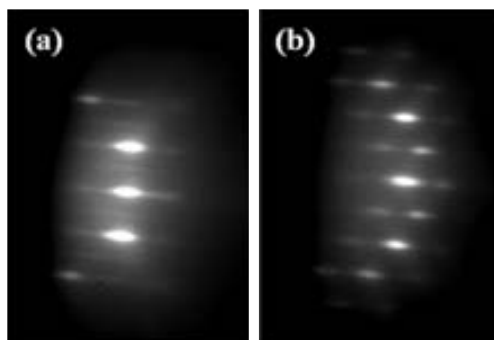
Fig. 7-49 RHEED pattern of 10% Zr-doped Ceria grown on YSZ single crystal (a)along the <100> substrate direction and (b) along <110> substrate direction.

AFM of this sample in Fig. 7-50 show that oxygen atmosphere has further enhanced the (001)- terraced surface morphology and this film became much smoother (rms ∼ 0.8nm). Indeed, it displays 93% of atomically flat surface, in agreement with 2D RHEED pattern. Based on [38] we suggest the film reconstruction as a possible mechanism to eliminate carbon impurities and stabilization of (001)-polar CeO$_2$ surface.
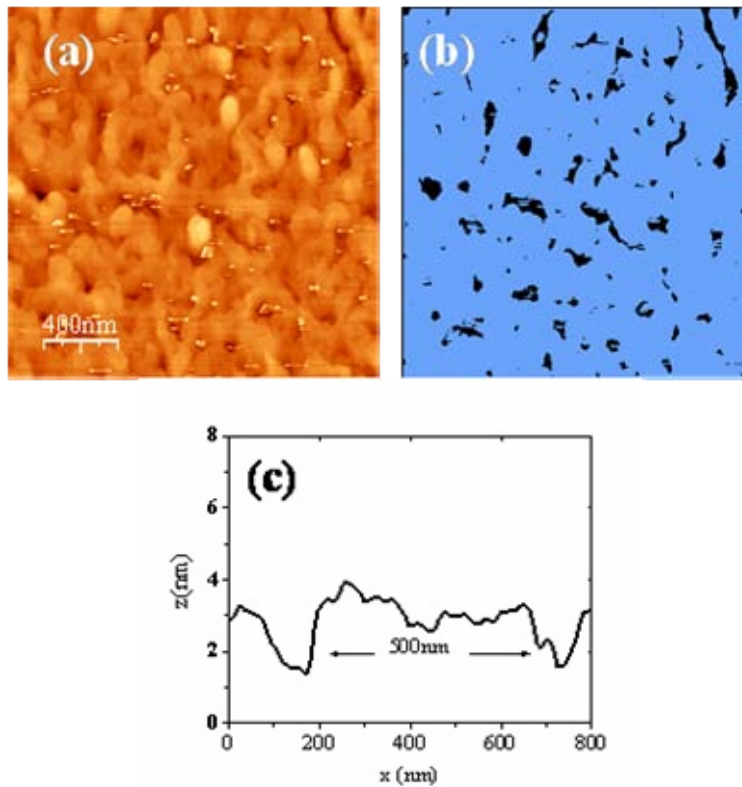
Fig. 7-50   2x2μm AFM scan of CZO/YSZ grown under oxidizing atmosphere at 900ºC for 8 h.

At this point we would verify if percentage of epitaxial fraction and atomically flat area obtained for MOD-CZO films accomplish the predicted dependence found between these two parameters for MOD- ceria samples studied all along this chapter. The results are displayed in Fig. 7-51. We appreciate that CZO films do follow the predicted dependence. Therefore it seems safe to conclude that this correlation can be explained by the mobility of $V_o^{..}$ simultaneously withg C content elimination and it has been corroborated that depends on the type of dopant, association among defect, concentration of dopants and also growth parameters.
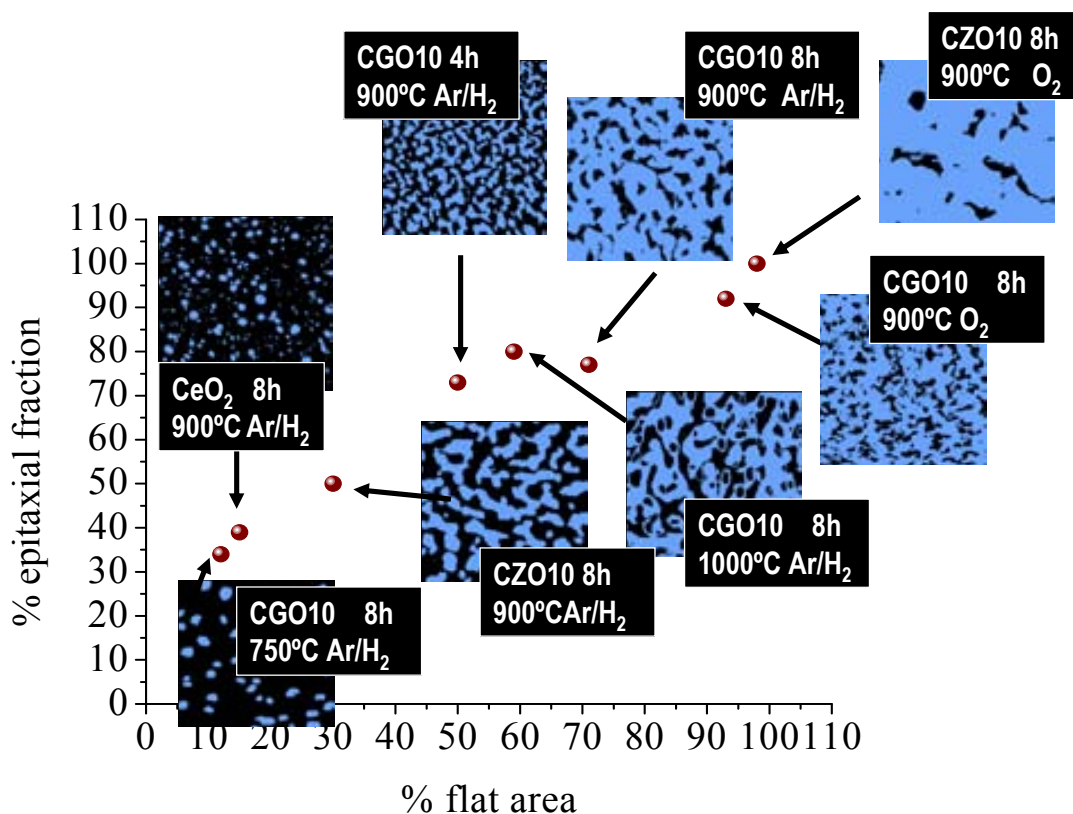
Fig. 7-51 Dependence of percentage of epitaxial fraction on percentage of flat area for modified-CeO$_2$ films deposited on YSZ single substrate.

7.6 Conclusions

In this chapter, we have investigated the growth mechanisms and microstructure of doped-CeO$_2$ films grown by chemical solution deposition as feasible cap layer for TFA-YBCO coated conductors. Based on recently work performed in our group on MOD-CeO$_2$ cap layer in which it was demonstrated that CeO$_2$ film grown under reducing atmosphere is inherently granular as a result of grain growth inhibition induced by grain-boundary contamination with C impurities, we have focused on increasing grain boundary mobility avoiding pure oxygen atmosphere to overcome this blocking mechanism and obtain highly textured and atomically flat (001)-terraced surface MOD-CeO$_2$ films.

Here we have analysed three approaches to increase mobility in CeO$_2$ lattice. Reducing conditions has been preserved to be further transferred on metallic substrate: (1) modification of growth conditions (atmosphere, time and temperature) (2) modification of precursor solution and (3) incorporation of dopant agents into CeO$_2$.

By investigating the influence of growth atmosphere (Ar/H$_2$/H$_2$O or O$_2$+Ar/H$_2$) on 30nm CeO$_2$ film quality, we have found by XRD and RHEED analysis that films are partially or

completely untextured. AFM study reflected that in all cases films conserve granular surface morphology and around 18% of surface is atomically flat. Additionally, we have found by XPS measurements that some C is still trapped in grain boundaries, probably as Ce$_2$C$_3$ or CeC$_4$, inhibiting grain growth.

By varying the precursor solution (acetates have been replaced by propionates), we obtained two significant improvements. On one hand the solution lifetime was increased from several hours to several months. This is due to the chelat effect of new precursors. On the other hand we have observed a significant increase in epitaxial fraction (from ~19% to ~38%). This improvement has been related to the decomposition pathway of organic precursor through formation of isoprene. AFM analysis illustrated that surface morphology has not been modified, rounded grains govern surface morphology.

Finally, we have studied the effect of dopant agents: Gd^{3+} and Zr^{4+} into cerium oxide epitaxy and surface morphology. We have detected that both dopants have increased mobility in CeO$_2$ lattice, but it seems that different mechanism are followed in each case. Whereas for Gd-doped CeO$_2$ it has been suggested that mobility is introduced through oxygen vacancies formation by charge compensation, it is likely that in Zr-doped CeO$_2$ the key parameter is the small ionic radius of Zr^{4+}. It has been proposed that it reduce the strain generated in the lattice due to Ce^{4+} to Ce^{3+} conversion and the corresponding oxygen vacancies. Although epitaxial fraction has been improved to ~77% for Gd-doped CeO$_2$ and to ~50% for Zr-doped CeO$_2$ in Ar/H$_2$ atmosphere, carbon has not been effectively removed. Thus, there is room for further improvement of film quality.

We have found that there are other factors affecting the complex mechanism of elimination C impurities to achieve high quality CeO$_2$ film: concentration of dopant, growth temperature, time and processing atmosphere.

Optimization of dopant concentration has been deeply investigated by Gd^{3+} incorporation. We have observed that the original granular regime detected in pure CeO$_2$ film is successfully suppressed by doping CeO$_2$ with 10% of Gd^{3+} (77% of epitaxial fraction). In addition, by the incorporation of this percentage we have stabilized (001)- flat terraced surface leading to ~70% of atomically flat surface. By contrast, we assume that lower percentage of Gd^{3+} generates few oxygen vacancies and therefore we could not enhance the atomic mobility. Ce$_2$C$_3$ still surround misoriented grains and poor degree of epitaxy and surface morphology with ~ 13% of atomically flat area were observed. Higher percentage of Gd^{3+} (≥20%), incorporated with a primary intention to increase the mobility, resulted as a blocking agent because strong interaction between solute and oxygen vacancies occurs and consequently hinders the atomic mobility in ceria. In addition, at very high concentration of Gd^{3+}, above the solubility limit, it is

likely that this strong interaction might evolutes to phase segregation. We have obtained percentages of epitaxial fraction ranging from ~30 to 44% .

We have also observed that time and growth temperature conditions could also influence the mobility in 10% Gd-doped CeO$_2$ films. It is worth of remark that no influence of adding H$_2$O in the gas flow was detected in this case. It is likely that in this case hydroxyl groups do not play any additional role in stabilizing (001)- terraced surface.

Finally, by the combination of CeO$_2$, CGO and CZO results we have demonstrate that exist a gradual increase in the epitaxial fraction and the percentage of atomically flat area runningin parallel to the elimination of carbon content.

CHAPTER 8

YBa$_2$Cu$_3$O$_7$ deposition on MOD- CeO$_2$ based cap layer buffered YSZ single crystal

8.1 Motivation

High J_c was observed for YBCO film prepared by TFA-MOD route on vacuum CeO$_2$-buffered YSZ single crystal in chapter 7. The next goal that must be achieved now for all chemical CC technology to be competitive is to reproduce high J_c values for TFA-YBCO on MOD-CeO$_2$ buffered YSZ single crystal. To do that, in the previous chapter, we developed MOD- 10%Gd-CeO$_2$ (CGO10) cap layer processed in 95%Ar/5%H$_2$ (Ar/H$_2$) reducing atmosphere that fulfils the requirements as cap layer for YBCO CC fabrication.

However, achieving high J_c values on MOD-CeO$_2$ is not straight forward. In fact, our preliminary studies of TFA-YBCO film with a thickness of 150 nm grown on MOD-CeO$_2$ /YSZ single crystal substrate were negative. These YBCO films carried a J_c of only 10^5 A cm^{-2} at 5K [139]. One of the main drawbacks reported by several authors is the interface reaction between YBCO and CeO$_2$ with the BaCeO$_3$ formation which is evidenced in both vacuum and non vacuum deposition techniques [246,247].

In this work, we conducted a systematic investigation of the effect of the underlying surface and texture of the modified-CeO$_2$ buffer layers on the properties of the subsequently

deposited YBCO film. As a first step we considered YBCO deposition by pulsed laser deposition (PLD) due to vacuum deposition methodologies can certainly reproduce high-performance coated conductors [248,36]. Subsequently, we optimized the growth conditions of TFA- YBCO on MOD- ceria cap layer with specific focus placed on BaCeO$_3$ formation.

8.2 PLD- YBCO on MOD- (doped)- CeO$_2$ /YSZ single crystal

Among all modified MOD-CeO$_2$ buffer layers prepared in the previous chapter, those films which presented higher epitaxial fraction and flat-(001) terraced surface were selected as the most appropriates for high quality YBCO growth in accordance with [38], whereas those that presented granular surface morphology with low epitaxial faction were excluded. To easily verify this proposal, in collaboration with Dr.R.Hühne in IFW-Dresden, optimized PLD-YBCO were deposited on (1) granular MOD-CeO$_2$ and (2) terraced-like MOD-doped CeO$_2$ cap layers. We would like to reiterate that CeO$_2$ and doped-CeO$_2$ films were fabricated from propionates precursor (described in 3.3.3.3). Optimal PLD-YBCO deposition conditions were:

T= 810ºC

Laser energy density=220 kV

Deposition rate=1Å/pulse

Repetition rate = 5Hz

P(O$_2$) Deposition step =0.03 kPa

P(O$_2$) Oxygenation step = 40 kPa

Standard thickness= 300 nm

8.2.1 PLD- YBCO on MOD-CeO$_2$ cap layer

PLD-YBCO film was first deposited on pure MOD-CeO$_2$ cap layer grown under Ar/H$_2$ atmosphere. We would like to bring to mind that this cap layer displayed a surface morphology dictated by rounded grains (13% of atomically flat area) and from the structural analysis two contributions were detected: a textured and a random fraction. They are clearly illustrated in XRD pole figure shown in Fig. 8-1(a).

After depositing PLD-YBCO film, x-ray diffraction was employed to study the phase purity and texture of the superconducting film. J_c was determined by inductive measurements.

From XRD θ-2θ scan, illustrated in Fig. 8-2, we denoted that YBCO films are c-axis oriented on the CeO$_2$ buffered YSZ single crystal substrate. In addition, we also detected an impurity peak at 2θ ≈ 41.8º indexed as BaCeO$_3$ phase [198]. The presence of this phase together with weak CeO$_2$ reflections is an indication that exist interaction between CeO$_2$ and YBCO layers. Note that in this case BaCeO$_3$ is present in a single texture whereas for TFA-YBCO/vacuum-CeO$_2$/YSZ single crystal system it showed two orientations (recall Fig. 6-13).
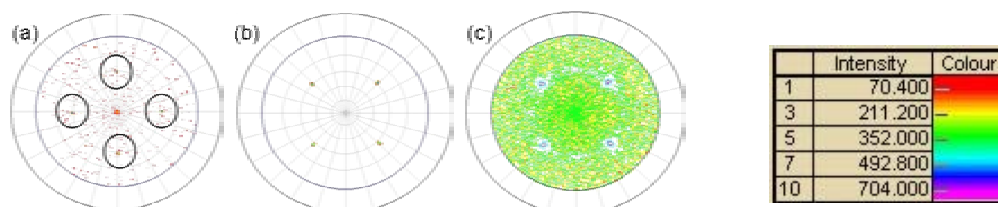

Fig. 8-1 X-ray pole figure measurements (CuK$_\alpha$) taken from the layer sequence of PLD-YBCO/MOD-CeO$_2$(Ar/H$_2$)/YSZ (a) (220)CeO$_2$ reflection and (b) (103)YBCO reflection (c) (103)YBCO reflection in log scale.
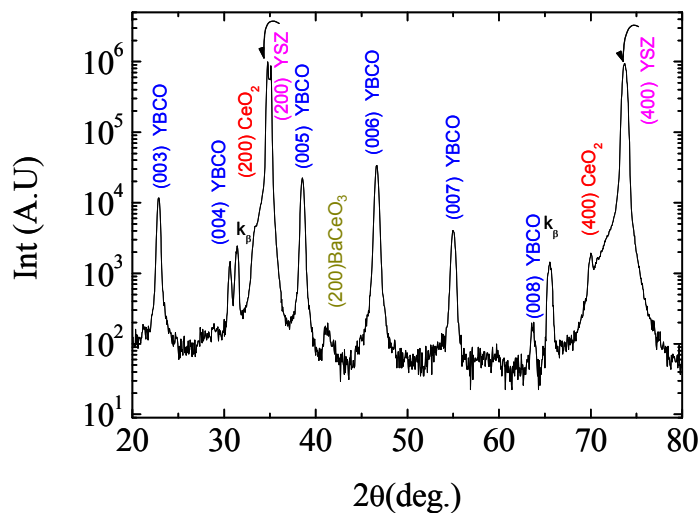
Fig. 8-2 X-ray diffraction pattern of PLD-YBCO/MOD-CeO$_2$/YSZ single crystal substrate.

In chapter 6 it could not be estimated the amount of BaCeO$_3$ formed in YBCO/CeO$_2$ interface because of the poor resolution of the XRD θ-2θ scan. In order to overcome this problem, as we previously announced, from chapter 7 to now, we used another XRD instrument (Philips PW3710 MRD Control Diffractometer) which allows us to quantify BaCeO$_3$ content, C$_{BCO,}$ defining a general formula in Eq. 8-1,

$$C_{BCO} = \frac{\left(I(110)_{BCO} + I(200)_{BCO}\right)}{\left(I(110)_{BCO} + I(200)_{BCO} + Ik_{\beta}\right)} \qquad \text{Eq. 8-1}$$

where I(110), I(200) and I$_{k\beta}$ contributions represent the X-ray θ-2θ scan intensities of the Bragg line reflections here indicated: The first two correspond to the two possible orientations earlier detected for pseudocubic BaCeO$_3$ phase (section 6.4) and the latter corresponds to the k$_\beta$ reflection associated to YSZ substrate. In this particular case, I(110)$_{BCO}$ is assumed to be zero since it has not been detected in XRD θ-2θ scan from Fig. 8-2. After computing the above equation we obtained C$_{BCO}$ ~0.21.

The XRD pole figure was measured on the YBCO film, using the (103) YBCO reflection. From Fig. 8-1(b) it is easily seen that CeO$_2$ layer leads to fibre texture in the YBCO layer. For better appreciation of this low degree of YBCO texture, pole figure from (103) YBCO reflection is shown in Fig. 8-1(c) in logarithmic scale. Pole figures from CeO$_2$ and YBCO film show an epitaxial relationship with a 45º in-plane rotation which can be easily understood considering that with this configuration the lattice mismatch between the cap layer and the superconducting layers is ε= -0.52%.

Critical current density was measured from this sample and $J_c < 10^5$ A/cm^2 at 77K was obtained indicating poor superconducting properties being in well agreement with XRD analysis presented above. Thus, this result reflects that partially epitaxial CeO$_2$ film (38%) with granular surface (13 % of atomically flat area) transfers poor texture to the superconducting film which affects the overall quality of the YBCO film, as we predicted in chapter 7 from the study of MOD-CeO$_2$ cap layers.

8.2.2 PLD-YBCO on MOD-doped CeO$_2$ cap layer

PLD-YBCO film was deposited on 10%Gd-CeO$_2$ film (CGO10) and 10%Zr-CeO$_2$ film (CZO10) grown under two different atmospheres (a) 95%Ar/5%H$_2$ (Ar/H$_2$) and (b) pure O$_2$ atmosphere. As we observed earlier in chapter 7, they are distinguished by the epitaxial fraction of CeO$_2$ and the surface morphology (evaluated from the statistical parameter: rms roughness and percentage of atomically flat area), recall Fig. 7-51.

After deposition PLD-YBCO film, XRD analysis, electrical resistivity and critical current densities were carried out for all samples.

A typical XRD θ-2θ scan of PLD-YBCO film grown on MOD-doped CeO$_2$ cap layer is shown Fig. 8-3(a). Interestingly, XRD θ-2θ scans for PLD-YBCO film on MOD-(Gd,Zr)CeO$_2$/YSZ single crystal substrates do not present significant differences for different dopant or buffer growth atmosphere. Therefore, the scan in Fig. 8-3(a) is representative for all films studied in this section 8.2.2. The intense YBCO (00l) peaks indicate that YBCO film has a strong c-axis texture. Strong (h00) CeO$_2$ Bragg line reflection and only single weak peak of BaCeO$_3$ phase indicates that there is little interaction between doped-CeO$_2$ and YBCO layers. Indeed, we have calculated the concentration of BaCeO$_3$ formed in this sample, C$_{BCO}$, through Eq. 8-1 defined previously. From this computation we obtained C$_{BCO}$ ~0.11, considerably less than PLD-YBCO/MOD-CeO$_2$/YSZ single crystal substrate.Out-of-plane texture of the PLD-YBCO on the MOD-doped CeO$_2$ buffered YSZ single crystal substrate was also measured by the X-ray ω-scan of the (005)YBCO reflection (see Fig. 8-3 (b)). The FWHM values for these films were 0.3º ±0.1. Subsequently, we have also measured YBCO in-plane texture from (103) YBCO reflection. FWHM values for this set of samples are relatively constant at 1.2º, indicating a good transference of the biaxial texture from the CeO$_2$ buffer layer to the YBCO film, as could be observed from the list in Table 8-I. The pole position of the YBCO (103) plane rotated 45 º from CeO$_2$ (220) plane shows again that the epitaxial relation between YBCO and CeO$_2$ is: YBCO (00l) // CeO$_2$ (00l) and YBCO[100] // CeO$_2$ [110], Fig. 8-4.
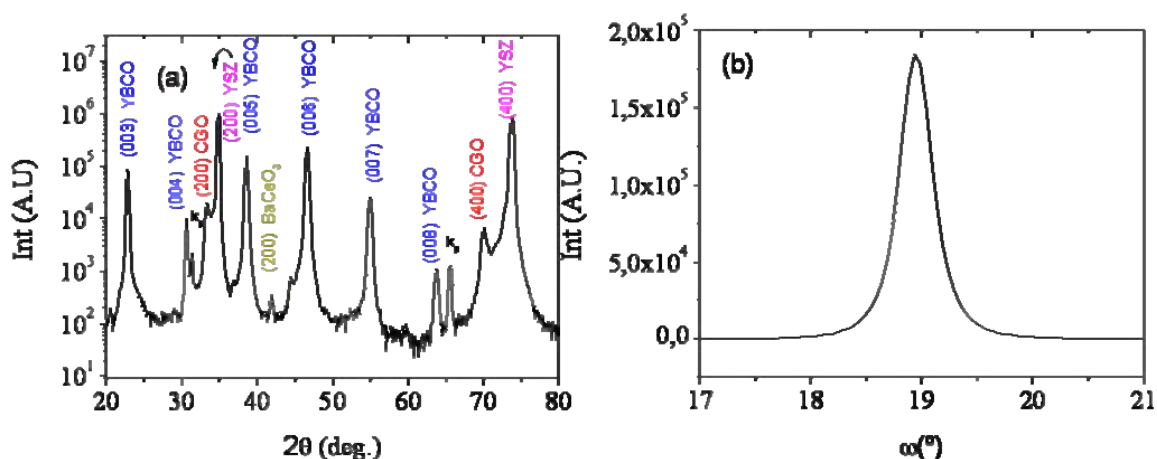
Fig. 8-3 (a) A typical XRD θ-2θ scan for a YBCO film with a thickness of 300 nm deposited by PLD on MOD-CGO10(Ar/H$_2$)/ YSZ system.(b) XRD ω-scan for YBCO(005) of the same film, FWHM=0.32º.

Table 8-I XRD FWHM values for in-plane texture of PLD-YBa$_2$Cu$_3$O$_7$ films on MOD-doped-CeO$_2$ buffered YSZ.

Sample	Buffer layer	Δφ(103)YBCO (deg) ±0.1	Δφ(220)CeO$_2$ (deg) ±0.1
Mu425	CGO Ar/H$_2$	1.2	1.1
Mu412	CGO O$_2$	1.1	1.1
Mu407	CZO Ar/H$_2$	1.2	1.2
Mu408	CZO O$_2$	1.2	1.2
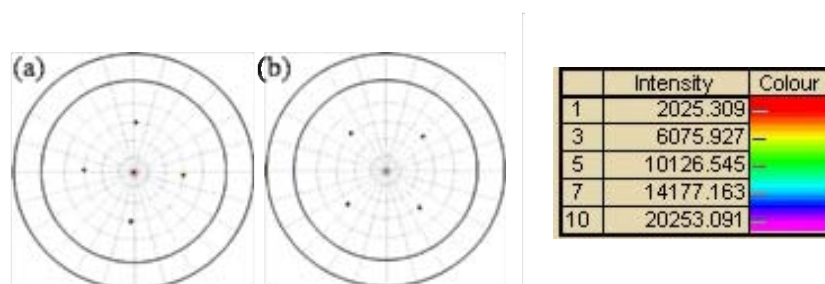
Fig. 8-4 XRD pole figures of (a) (220) MOD-CGO10 buffer layer grown on YSZ single crystal (b) (103) PLD-YBCO grown on MOD-CGO10 buffer layer.

216

Typical surface morphology of the PLD-YBCO layer deposited on doped-ceria cap layers, determined by SEM, shows a homogeneous surface microstructure with a high pore density, see Fig. 8-5. It is important to mention that other groups [96,200] have obtained PLD-YBCO film on CeO$_2$ cap layer significantly denser. In order to denisfy our PLD-YBCO films, it should be required a detailed optimization of deposition parameters.
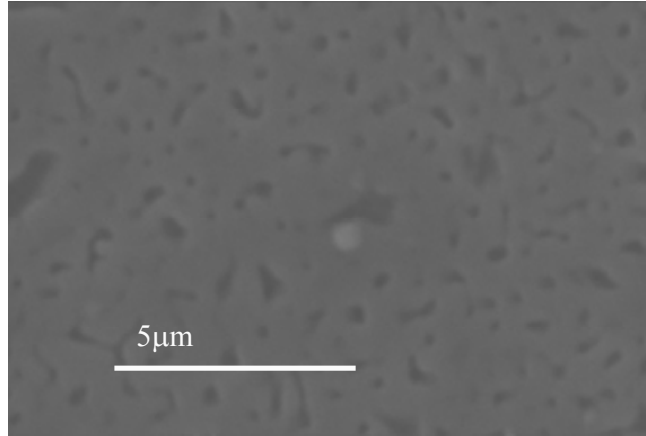
Fig. 8-5 SEM micrograph of 300 nm thickness PLD-YBCO film annealed at 810ºC in 0.03 kPa oxygen on MOD-CGO/YSZ single crystal substrate.

PLD-YBCO layer grown on doped-CeO$_2$ cap layers typically showed a superconducting transition between 88.9 and 89.8 K with a transition width ΔT_c between 1 and 1.6 K, indication of good film quality. These results are consistent with that of XRD texture analysis in which YBCO films displayed good biaxial texture. Critical current density values measured at 77K for the PLD YBCO films are listed in Table 8-II. It is noticeable that no significant changes exist in J_c values achieving an average value of around 3.3 MA cm^{-2}, similar to that obtained on YBCO/LAO single crystal substrates [34].

Table 8-II Characterization of MOD-derived CeO$_2$ cap layers surface quality and the corresponding values of J$_c$ and T$_c$ for the PLD-YBCO film deposited on top.

Sample	Buffer layer	CeO$_2$ surface rms (nm)(scan 2x2 μm) ±0.3	Flat area grains (%) (scan 2x2 μm)	J$_c$ (MA/cm^2) 77K	T$_c$90(K)
Mu425	CGO Ar/H$_2$	4.4	71	3.33	89
Mu412	CGO O$_2$	3.0	90	3.34	89
Mu407	CZO Ar/H$_2$	4.3	30	3.42	90
Mu408	CZO O$_2$	1.2	92	3.79	90

Therefore, exist a clear difference between the quality of PLD-YBCO film grown on undoped (section 8.2.1) and doped CeO$_2$ film indicating that the quality of cap layer do influence the subsequent growth of PLD-YBCO film. In Fig. 8-6 (a) we have represented the dependence of atomically flat area of (doped)-CeO$_2$ film on the critical current density for the superconducting layer. By increasing the percentage of flat area from 18% to 31% J_c values strongly improve from ∼0.1MA cm^{-2} to 3 MA cm^{-2} at 77K. By contrast, from 31% to 92% J_c values remain almost constant. By considering the correlation found in the previous chapter between percentage of atomically flat area and percentage of epitaxial fraction, Fig.7-47, we assume that J_c values also depends in a similar way on the microstructure quality of (doped)-CeO$_2$ cap layer.

However, if we now compare J_c evolution with rms parameter determined in the previous chapter from CeO$_2$ surface we observe that highest rms value does not correspond with lowest critical current density, Fig. 8-6 (b). Therefore, it corroborates that rms is a non meaningful parameter to evaluate CeO$_2$ surface quality for biaxially PLD-YBCO growth, similarly to TFA-YBCO/vacuum-CeO$_2$/YSZ architecture analysed in chapter 6.
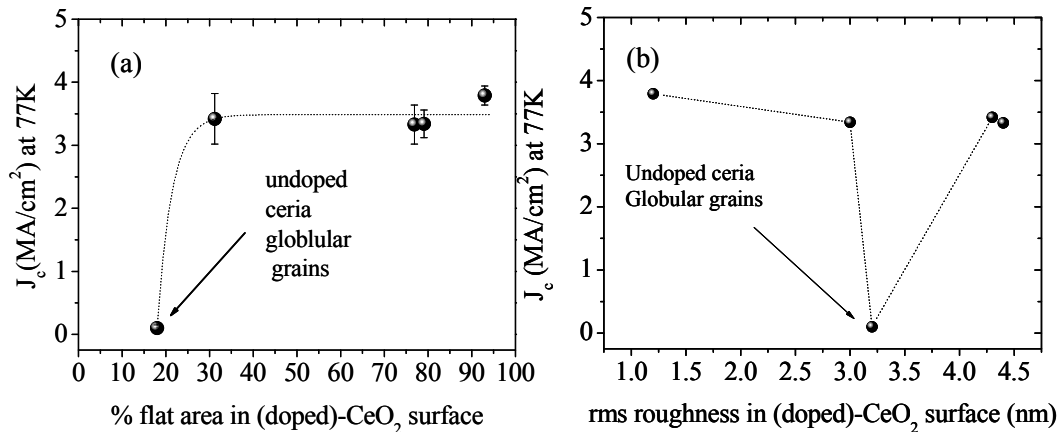
Fig. 8-6 Dependence of J_c at 77K for PLD- YBCO films (a) as a function of atomically flat area of the underlying MOD-modified CeO$_2$ buffer layer (b) as a function of the statistical rms surface parameter.

In addition, we would like to note that (doped)-CeO$_2$ cap layer presenting a percentage of atomically flat area over 30% not only improve YBCO film quality, it also leads to lower interface reaction (recall C$_{CBO}$ ≈0.11 versus C$_{CBO}$ ≈0.21). These results also suggest a correlation between atomically flat area in CeO$_2$ film and interface reaction as we previously detected in TFA-YBCO film grown on vacuum-deposited CeO$_2$ films. However, more experimental work

is needed in order to draw a conclusion on the role of BaCeO$_3$ phase on YBCO/CeO$_2$/YSZ system.

8.3 TFA- YBCO on MOD-CGO10 /YSZ single crystal

In order to transfer the knowledge acquired from PLD-YBCO film grown on MOD-doped-CeO$_2$ film to TFA-YBCO film growth, we first started with CGO10 cap layer grown under reducing atmosphere since this processing atmosphere could be further transferred on metallic substrate (Ni). As a first step we have considered the set of CGO10 samples grown under different growth conditions ((1) 780ºC for 8 h, (2) 900ºC for 4 h, (3) 1000ºC for 8 h and finally (4) 900ºC for 8 h) which led different surface morphology (recall section 7.5.1.1.3.2). Therefore, we expect that they influence in a different way the TFA-YBCO growth.
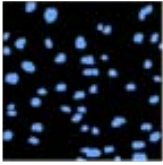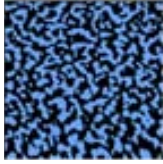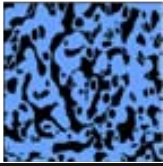
TFA-YBCO films were prepared from anhydrous precursor solution (1.5M) using conditions detailed in the experimental procedure in section 3.1.1.2. Pyrolysis conditions had to be modified for this system otherwise cracked and buckled films were obtained. In this particular case, it was followed the schematic profile described in Fig 3-3(b) but oxygen gas flow rate was increased to 0.075 l min^{-1}.

Initially, processing conditions used for YBCO conversion are based on the optimal results obtained for TFA- YBCO grown on vacuum-CeO$_2$ (780 ºC, 180 min, P(H$_2$O)= 0.6kPa, P(O$_2$) = 0.02 kPa and gas flow rate =2.03 x10^{-2} m s^{-1}), Fig. 6-12.

In Table 8-III are summarized the most significant results of these films, the relationship between surface morphology of CGO10 cap layer (rms and percentage of atomically flat area) and critical current density of subsequent TFA-YBCO film. We present J_c values at 5K since at 77K it is reduced by two or three orders of magnitude for most of them, indicating poor YBCO film quality.

These results evidence a dramatic dependence of TFA-YBCO film quality on doped-CeO$_2$ cap layer quality, emphasizing once more that the key parameter to evaluate the quality of CeO$_2$ surface morphology is the percentage of atomically flat area, indeed, highest J_c value, 1.5 MA cm^{-2} at 5K, was obtained on CGO10 cap layer with ~71% of atomically flat area. Therefore, in the following section we have presented a complete characterization of this TFA-YBCO film. However, it is noteworthy that the critical current density for this film is still one order of magnitude below of the current carried for PLD-YBCO on the same CGO10 cap layer.

Table 8-III Processing parameters for CGO10 films, surface morphology properties of CGO10 and critical current density of TFA-YBCO deposited on top

CGO processing conditions	Binary image of CGO10	rms roughness (nm) ±0.3 (2x2µm scan)	% atomically flat grains (±2)	J$_c$(5K)A cm^{-2}
750°C 8h Ar/H$_2$		7.2	12%	<10^5
900°C 4h Ar/H$_2$		3.1	46%	<10^5
1000°C 8h Ar/H$_2$		4.2	59%	0.3x10^6
900°C 8h Ar/H$_2$		4.4	71%	1.5x10^6

8.3.1 TFA-YBCO film on MOD-CGO10 (900°C, 8 h in Ar/H$_2$)/YSZ

From X-ray θ-2θ scan, Fig. 8-7 (a), it was noticeable YBCO film with c-axis texture and no detection of intermediate phases such as BaF$_2$ which indicates that precursors are fully converted to YBCO. However, (200) CGO10 peak reflection has been almost disappeared and high intensity peaks of BaCeO$_3$ (110) and (200) were detected. This suggests that reaction between YBCO and CGO10 buffer layer during the high-temperature anneal has occurred. By computing the BaCeO$_3$ formation from X-ray diffraction θ-2θ Bragg line intensities, Eq. 8-1, we have obtained C$_{BCO}$ ≈0.50. This value is quite high in comparison with PLD-YBCO on MOD-derived CeO$_2$ films presented earlier (C$_{CBO}$ =0.11 and C$_{CBO}$=0.21). Thus, it points that all-chemical multilayers tend to react in more extension than vacuum deposited films.
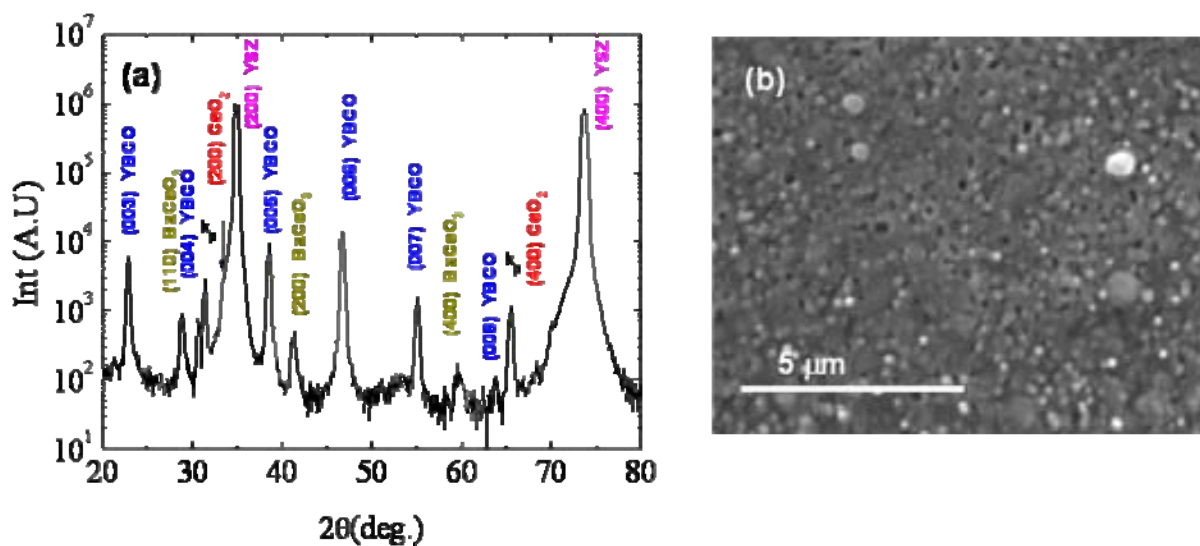
Fig. 8-7 (a) Typical XRD θ-2θ scan of TFA-YBCO film grown on MOD-CGO10 (Ar/H$_2$)/YSZ single crystal substrate and (b) SEM micrograph of the as described sample.

From the presence of BaCeO$_3$ we would expect the detection of secondary phases in YBCO film such as Y$_2$O$_3$ or Y$_2$Cu$_2$O$_5$ to compensate Ba deficiency. Unfortunately the most intense reflections for these phases are overlapped with 2θ reflections of YSZ or CeO$_2$. It is interesting to note that XRD 2θ values for BaCeO$_3$ reflections are slightly shifted from 'pure' BaCeO$_3$ phase due to the presence of gadolinium. This is not surprising since early studies performed in doped-CeO$_2$ films, we already detected that the incorporation of aliovalent cation into ceria lattice slightly modify the cell parameter, Fig.7-16.

X-ray ω-scan and φ-scan was performed for the YBCO (005) and (103) reflection respectively, Δω ≈ 2.4º and Δφ ≈2.1º, indicating low degree of texture.

SEM image, Fig. 8-7 (b), showed a uniform surface with granular structure decorated with small porous feature. This surface morphology contrasts with the one observed form PLD-YBCO films, probably due to the different YBCO growth mode[100,71]. Under this conditions, as earlier mentioned, J_c value for TFA-YBCO film on MOD-CGO10/YSZ single crystal substrate was 1.5 MA/cm^2 at 5K but at 77K J_c value fall down to 10^5 A cm^{-2}, indicating a strong degradation of the film.

Due to TFA-YBCO film properties are not as high as the ones observed in YBCO vacuum deposited systems (see section 8.1.2), efforts are carried out to optimize YBCO growth parameters. As already mentioned at the beginning of this work, a lot of parameters influence the YBCO growth from trifluoroacetate precursors and most of them have to be varied

simultaneously. With these previous results in mind we proceeded on improving TFA- YBCO film quality on MOD-CGO10 buffered YSZ single crystal.

8.3.2 Optimization of TFA-YBCO film on CGO10(Ar/H$_2$)/YSZ single crystal substrate

8.3.2.1 Study of the residence (wet) time at high temperature

As a first approach, we investigated the influence of holding time under wet atmosphere at the YBCO crystallization temperature on BaCeO$_3$ formation and YBCO film quality. Dry dwell time was kept constant in 30 minutes. At the same time we increased YBCO growth rate through P(H$_2$O), based on R$\propto$P(H$_2$O)$^{1/2}$ dependence [85]. Both parameters have been investigated with the purpose to reduce the residence time between CeO$_2$ and YBCO precursors but preserving a fully converted YBCO film. Thus, we increased P(H$_2$O) from 0.6 kPa to 2.2kPa and wet dwell time was investigated in the range of 45 to 150 min.

Samples were annealed at 780°C in P(O$_2$)=0.02 kPa, P(H$_2$O) =2.2kPa and gas flow rate of 2.03 x10^{-2} ms^{-1}. The film thickness of YBCO on CGO10 buffered YSZ was measured by profilometry and was in the range 150 nm ± 30.

8.3.2.1.1 Structural and morphological characterization of TFA-YBCO films

To examine the phase development, XRD θ-2θ scans of YBCO films were carried out, Fig. 8-8. Note that all spectra have been shifted vertically to easily appreciate variations in intensity and secondary phases. All the YBCO (00l) diffractions peaks are present indicating that YBCO is c-axis oriented. Peaks from YSZ substrate, CeO$_2$ buffer layer, and BaCeO$_3$ (BCO) were also observed. We would like to emphasize since (111) BaF$_2$ Bragg line reflection did not appear in any XRD 2θ scan, 2θ = 28.8 and 41.2°, are assigned to BaCeO$_3$ phase. Secondary reflection at 2θ = 44.67, 50.96, 52.86 and 58.06° are indexed as Y$_2$Cu$_2$O$_5$, BaCuO$_{2+x}$ and CuO respectively. They can be formed as a result of two pathway reactions: On one hand secondary phases resulting from YBCO conversion [71] and on the other hand as subproducts of interface reaction [198].
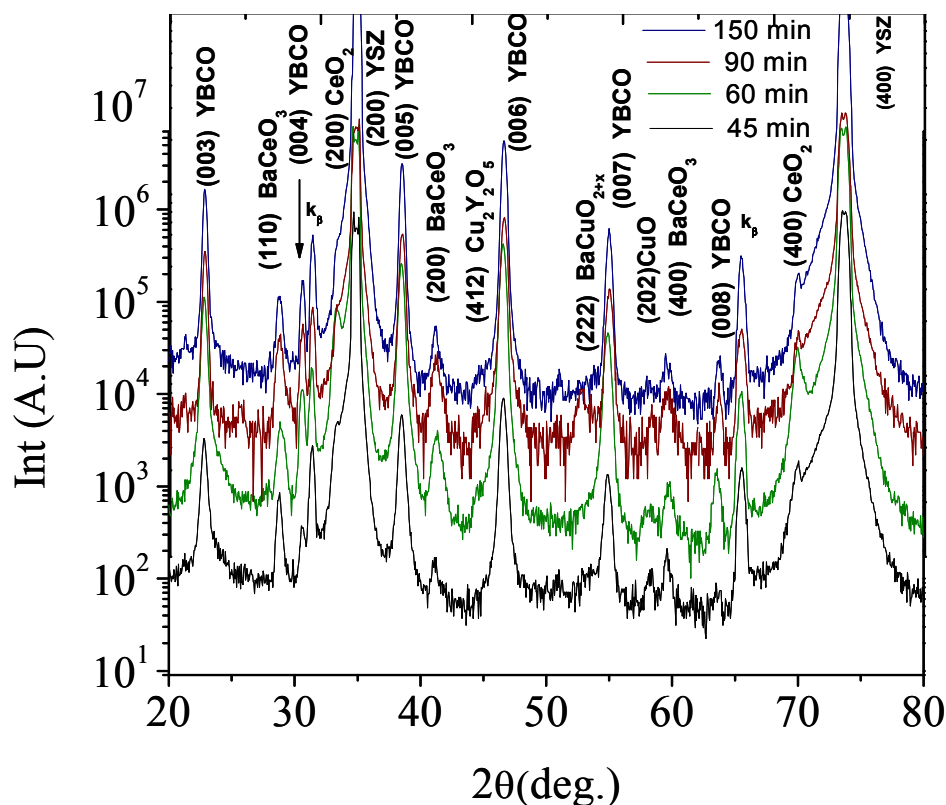
Fig. 8-8 X-ray θ-2θ reflections of YBCO film on CGO-buffered YSZ substrate. Samples were converted at 780°C in 0.02kPa oxygen for different wet dwell time.

To estimate in a simplified way the evolution of YBCO epitaxy on the wet dwell time, it has been normalized I(005) YBCO peak reflection with I(k_β), similarly to the equation defined for BaCeO$_3$ quantification (Eq. 8-1). Concomitantly, we have studied BaCeO$_3$ content evolution on the wet dwell time and results are shown in Fig. 8-9. In both phases it is reflected a similar behaviour, at t(wet)=60 minutes, Bragg line intensity saturates. This indicates that YBCO conversion on MOD-CGO10 finishes after 60 minutes exposure in wet atmosphere. On the other hand, BaCeO$_3$ formation stops after 60 minutes. Therefore from this dependence it is likely that YBCO conversion is correlated to BaCeO$_3$ formation. This correlation is not surprising considering that for the formation of both it is required that H$_2$O decompose BaF$_2$ phase. Additionally, in the same figure it has been anticipated values of t=0 obtained from a quench study presented forth. It is interesting to evaluate these results because the existence of a fraction of 0.45 of YBCO (00*l*) oriented at t=0 indicates that YBCO c-axis oriented grains started to grow during the heating rate. By contrast, low fraction of BaCeO$_3$ phase (lower than 0.2) suggested that interface reaction takes place mostly in dwell step at 780°C rather than during the heating rate.
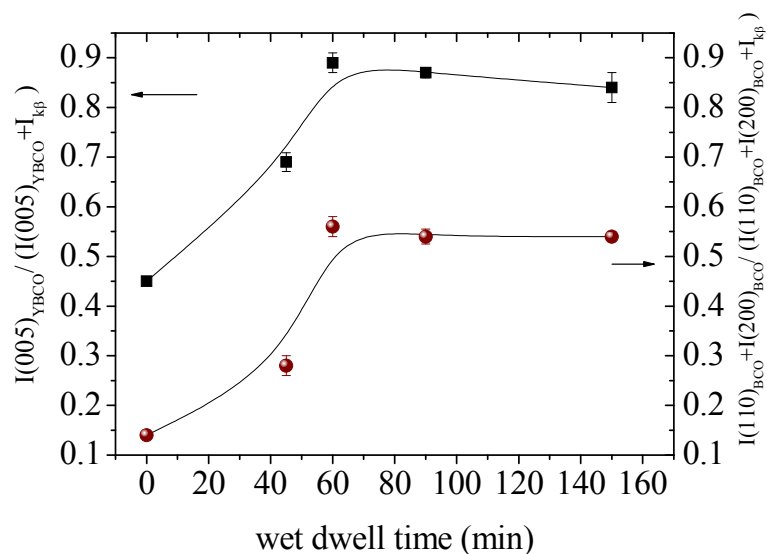
Fig. 8-9 Evolution of YBCO epitaxy and BaCeO$_3$ formation on the wet dwell growth time.

Nevertheless, by further texture analysis from ω-scan of (005) YBCO reflection, we detected a slight film degradation at prolonged heat treatment, as could be seen in FWHM values listed in Table 8-IV. Since C(BCO) is maintained nearly constant at t (wet)≥ 60 min we could not assign YBCO texture degradation to BaCeO$_3$ formation, indeed, based on the work reported by Xu [128] we suggest that it is due to long exposure to wet atmosphere at high temperature.

Therefore, based on this structural data, at T=780ºC, highest degree of crystallinity and epitaxy is obtained by processing YBCO during 60 min wet+30 min dry despite large interface reaction.

Table 8-IV Processing parameters and dependence on wet dwell time of (TFA) YBCO films deposited on (MOD)CGO10 cap layer

Sample	T(growth) (°C)	P(H$_2$O) (kPa)	P(O$_2$) (kPa)	Wet dwell (min)	Dry dwell (min)	YBCO(005) FWHM (deg) ±0.1	I(005)$_{YBCO}$/ [I(005)$_{YBCO}$+I$_k$]	C$_{CBO}$	J$_c$(A/cm^2) 5K	T$_c$(K)
YCYt45	780	2.2	0.02	45	30	1.6	0.74	0.28	1.05x10^6	90
YCYt60	780	2.2	0.02	60	30	0.9	0.92	0.56	8.32x10^6	90
YCYt90	780	2.2	0.02	90	30	1.4	0.82	0.54	1.44x10^6	87
YCYt150	780	2.2	0.02	150	30	1.8	0.86	0.54	2.55x10^6	88

From the surface morphology studied by SEM we do not observed any significant microstructural evolution of the YBCO film with the wet dwell time. In Fig. 8-10 it is shown a typical SEM top-view micrograph of TFA-YBCO film on MOD-CGO10 /YSZ substrate. We observe a continuous and dense film. Small grains with spheroidal morphology decorate the surface of the film, no a-axis grains were observed. By previous μ-Raman measurements performed in our group we presume that these grains are BaCuO$_2$ [121].
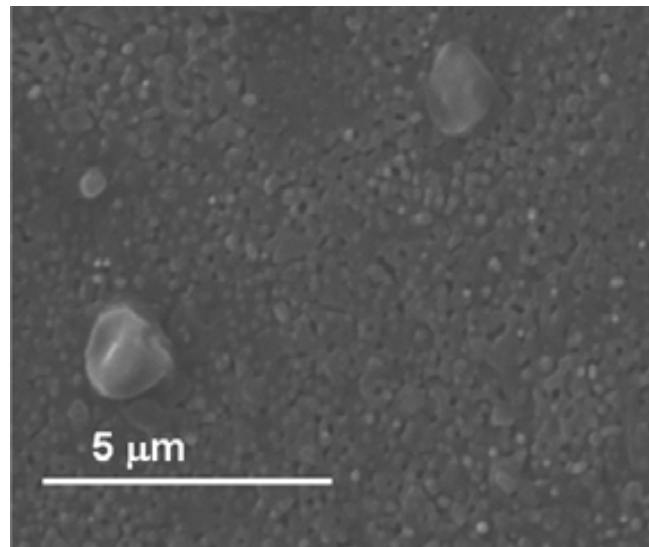
Fig. 8-10 SEM micrograph of TFA-YBCO film on MOD-CGO10 deposited on YSZ single crystal grown at 780ºC for 150 min (wet dwell).

8.3.2.1.2 Superconducting properties

From critical current density measurements at 5K it can be clearly seen that superconducting property follows the same trend as the degree of crystallinity of YBCO: In the initial period (45min) J_c increased with annealing dwell time and crystallinity. At a time of 60 min wet dwell, J_c and film crystallinity reached about the maximum. When we continued to prolong the high-temperature annealing time I(005)YBCO and I(BaCeO$_3$) remain almost constant but J_c decreased slightly correlating with YBCO texture analysis. Thus, film degradation is not due to BaCeO$_3$ formation at prolonged growth time being consistent with XRD analysis. Film degradation occurs due to contact with wet atmosphere at high temperature. Similar dependence was also found for TFA-YBCO/LAO model system [249,99].

In conclusion, 60 min anneal in humid atmosphere resulted in the best developed texture, crystallinity and highest J_c value despite BaCeO$_3$ formation

8.3.2.2 Study of the influence of P(H$_2$O)

Optimistic by the important improve in J_c value when P(H$_2$O) was slightly increased to 2.2 kPa for 90 minutes growth (60 wet and 30 dry dwell), we inspected the water partial pressure influence. Temperature was fixed at 780ºC for a total residence time of 90 minutes, P(O$_2$) = 0.02 kPa, gas flow rate = 2.03 x10^{-2} m s^{-1} and P(H$_2$O)–values have been varied from 0.6 to 3.3 kPa. In addition, it was investigated the influence of water partial pressure during the heating ramp. To do that, we carried out an experiment in which the flow of humid gas was injected into the furnace once the furnace temperature reached 780ºC. Results have been compared to sample grown at 2.2 kPa previously characterized.

8.3.2.2.1 Structural and morphological characterization

X-ray diffraction patterns, out-of-plane texture analysis and J_c have evidenced some evolution of the microstructure of the films with P(H$_2$O). Fig. 8-11 shows a comparison of XRD θ-2θ scan of final YBCO films obtained at different water partial pressure.

As a general trend, all the YBCO films display the (00l) diffraction peaks indicating that they are c-axis oriented. (110) and (200) reflections of BaCeO$_3$ simultaneously with slight decrease of (h00) CGO10 peak reflections, point out the existence of interface reaction. In certain growth conditions other secondary phases have been observed like Ba$_{1-x}$Y$_x$F$_{2+x}$ (BYF), BaCuO$_2$, BaF$_2$, CuO and Y$_2$Cu$_2$O$_5$. The reasons why they exist are considered below after analyzing the evolution of the degree of YBCO crystallinity and BCO formation.

In Fig. 8-12 we studied the degree of YBCO epitaxy and texture dependence on P(H$_2$O) from samples grown in the same processing conditions (i.e. humid gas injected at the beginning of the heating rate, ∼100ºC). In this figure we observed that at lower P(H$_2$O), i.e. 0.6kPa, degradation of the film quality is evidenced by very low I(005)YBCO peak reflections and high FWHM value from ω-scan. On the other hand, for YBCO film grown at higher P(H$_2$O) no important variations have been detected in a change in the relative heights of the YBCO reflections and FWHM (005) comparing with P(H$_2$O)=2.2kPa.
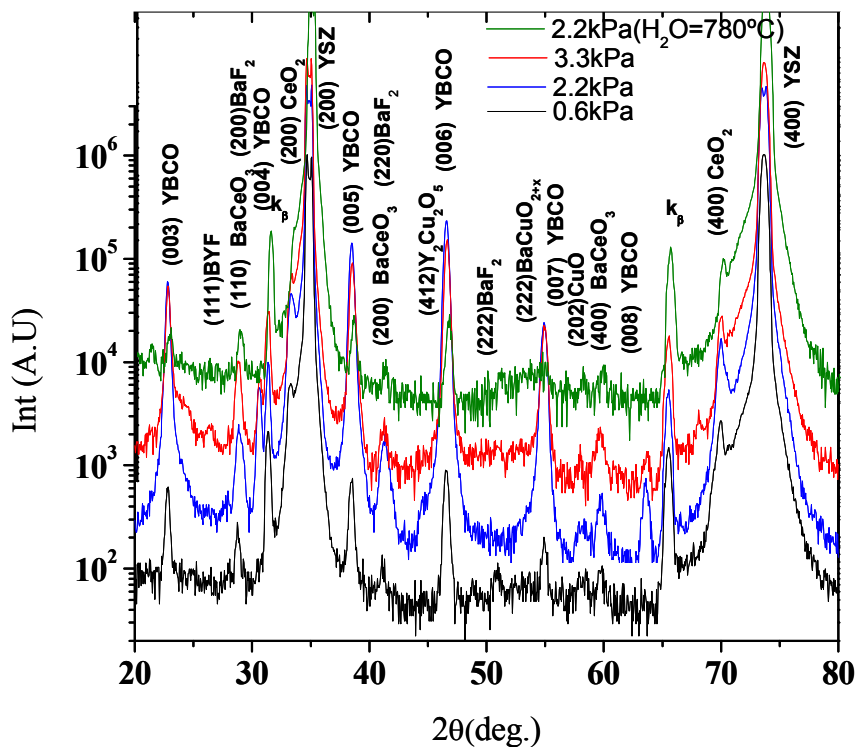
Fig. 8-11 TFA-YBCO on MOD-CGO grown at 780ºC for 90 min (60 min wet +30 min dry) at different water partial pressure.
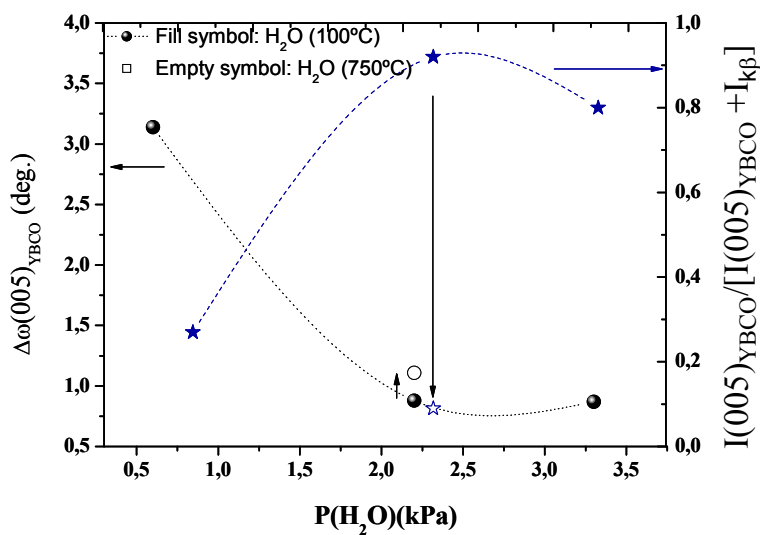

Fig. 8-12 Dependence of the normalized ratio of YBCO(005) peak intensity to I (k$_\beta$) and the $\Delta\omega$(005) YBCO on P(H$_2$O)-value.

For these films we have also studied the tendency of BaCeO$_3$ on P(H$_2$O)-values and results are listed in Table 8-V. Given that (111) BaF$_2$ reflection has been detected in θ-2θ scan for P(H$_2$O) =0.6 and 3.3 kPa values, the computation of BaCeO$_3$ content for these samples could be masked. Recall that the most intense reflections of BaCeO$_3$ matches with those from BaF$_2$ phase.

In order to minimize BaF$_2$ contribution on BaCeO$_3$ quantification, we have subtracted I(200) BaF$_2$ from I(110) BaCeO$_3$ (overlapped at 2θ ~ 28º) following the methodology proposed recently by Wesolowksi [201]. It consists of calculating I(111)BaF$_2$/I(200)BaF$_2$ ratio from a quench sample in which nor YBCO neither BaCeO$_3$ phases are present. Then, since BaF$_2$ intensity ratio is constant, when (111) BaF$_2$ peak reflection appears in XRD θ-2θ scan and I(200)BaF$_2$ peak reflection matches with (110) BaCeO$_3$ peak reflection, it can be figure out the intensity for (200) BaF$_2$ Bragg line reflection from the previously calculated ratio (I(111)BaF$_2$/I(200)BaF$_2$). Finally, I(200)BaF$_2$ is subtracted from total intensity of Bragg line reflection at 2θ ~ 28º and results I(110)BaCeO$_3$ contribution.

Similarly to the wet dwell time study discussed before, we can observe that BaCeO$_3$ follows YBCO tendency. Taking into account that for sample grown at P(H$_2$O)=0.6kPa we identified intense reflections of BaF$_2$ from XRD θ-2θ scan, we suggest that YBCO texture degradation could be related to an uncompleted YBCO formation due to insufficient supply of H$_2$O at the growing interface [137,99]. This proposal is also consistent with low content of BaCeO$_3$ since interface reaction could not take place if BaF$_2$ does not decompose providing Ba^{2+} cations [201]. At high P(H$_2$O)-values it was also found a microstructural degradation in YBCO film, which could not be attributed to BaCeO$_3$ since C$_{BCO}$ value has not increased from P(H$_2$O)=2.2kPa. Based on preliminary studies [99] we suggest that it could be related to the high HF concentration accumulated at the growing interface. It might happen that gas flow becomes insufficient to fully evacuate the high concentration of HF gas generated at high P(H$_2$O), and therefore it is supposed that some gas stagnancy occurs [85]. However, this correlation has to be verified in J_c studies.

We now turn to study the sample which has been grown under dry heating rate. From X-ray diffraction θ-2θ scan, Fig. 8-11 (green trace), we observe an important decrease in (00l) YBCO and in BaCeO$_3$ reflection peaks. Once more (00l) YBCO formation was correlated to BaCeO$_3$ formation, Eq. 8-1. Moreover, from Fig. 8-12 (empty symbols) we have also detected YBCO texture degradation. It suggests that the incorporation of H$_2$O at 780ºC delayed the YBCO conversion and also interface reaction. Therefore, 60 min in wet atmosphere leads to uncompleted YBCO formation.

Table 8-V Processing parameters and dependence on water partial pressure of (TFA) YBCO films deposited on (MOD)CGO10 cap layer

Sample	T(growth) (°C)	P(H$_2$O) (kPa)	P(O$_2$) (kPa)	Wet dwell (min)	Dry dwell (min)	YBCO(005) FWHM (deg)±0.1	I(005)$_{YBCO}$/ [I(005)$_{YBCO}$+I$_{k\beta}$]	C$_{CBO}$	J$_c$(A/cm^2) 5K	T$_c$(K)
YCYP06	780	0.6	0.02	60	30	>3.1	0.27	0.09	<0.1x10^5	-
YCYt60	780	2.2	0.02	60	30	0.9	0.92	0.56	8.32x10^6	90
YCYP33	780	3.3	0.02	60	30	0.9	0.80	0.35	5,59x10^5	85
YCYP22H*	780	2.2	0.02	60	30	1.1	0.09	0.12	<0.1x10^5	-

* Water has been introduced into the furnace at 780°C, i.e, dry heating ramp.

From the SEM micrographs, shown in Fig. 8-13, we can find that increasing water partial pressure from 0.2kPa to 2.2 kPa (Fig. 8-13(a-b)), the granular structure evolutes to smoother and denser one with some precipitates on top corresponding to BaCuO$_2$ phase. No differences have been detected in surface morphology between the sample grown at P(H$_2$O) =2.2kPa and P(H$_2$O)=3.3 kPa. Note that no a-axis oriented grains appeared in YBCO films. YBCO film grown in dry heating ramp (Fig. 8-13(d)) displays similar surface morphology as sample grown at P(H$_2$O)= 0.6kPa, following similar behaviour as XRD results.
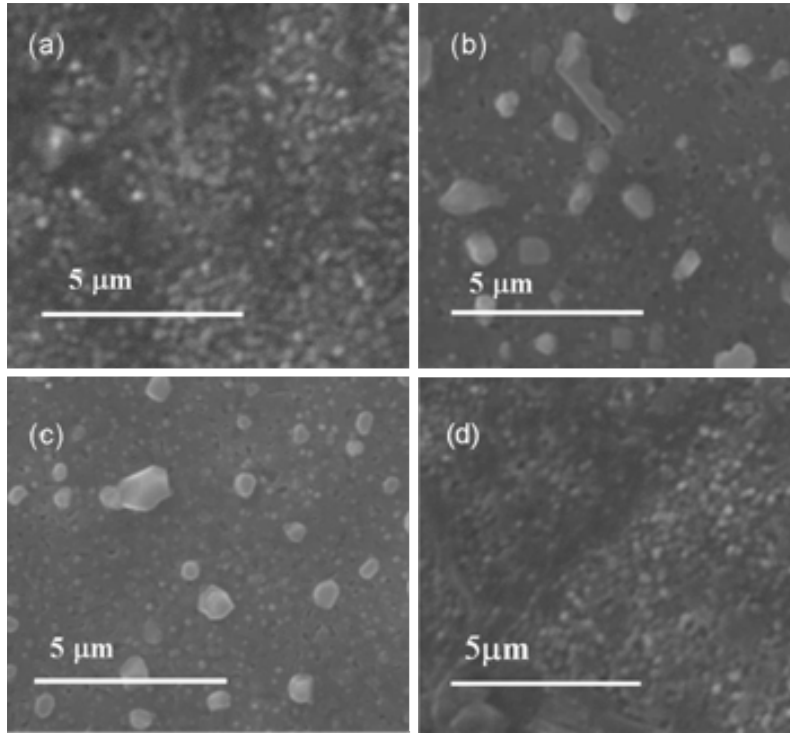
Fig. 8-13 SEM micrographs of 0.15 μm TFA-YBCO film annealed at 780°C at different P(H$_2$O)-values (a)0.2 kPa (b) 2.2 kPa (c) 3.3 kPa (d) 2.2kPa (H$_2$O=780°C)

8.3.2.2.2 Superconducting properties

Superconducting measurements were also performed for these set of samples and it was found maximum J_c value for sample grown 90 min (60+30) at P(H$_2$O)=2.2kPa in excellent agreement with structural and microstructural data presented above. It is interesting to remark that the highest J_c value (5K) has been obtained for the sample that displays higher I(005) YBCO from XRD θ-2θ scan and simultaneously higher C$_{BCO}$. On the other hand, samples grown at P(H$_2$O)=0.6kPa, 3.3kPa and 2.2kPa (H$_2$O 780°C) showed lower J_c values as well as lower degree of YBCO texture and lower C$_{BCO}$. Thus, it allows us to correlate degraded film

quality with uncompleted conversion or ineffective evacuation of high concentration of residual products (HF).
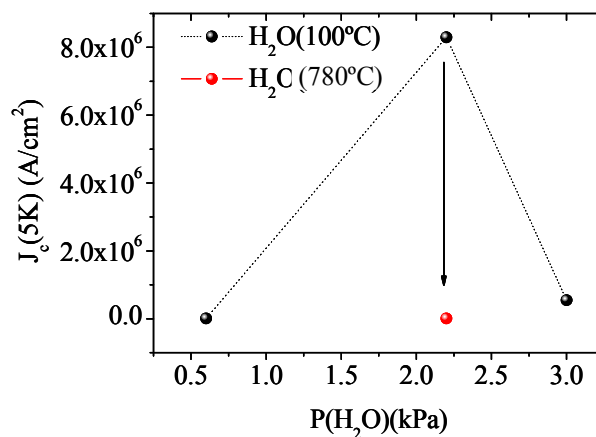
Fig. 8-14 Water partial pressure dependence on J_c (5K) for TFA-YBCO films grown on MOD-CGO10/YSZ substrates.

In conclusion, we observed that P(H$_2$O) parameter play a non-negligle role on TFA-YBCO grown on MOD-CGO10 films according to previous studies performed on LAO single crystal [99]. From the range of investigated conditions at 780ºC, we could not detached BaCeO$_3$ formation from YBCO growth. However, it is very important to remark that TFA-YBCO film grown on MOD-CGO10 cap layer can be biaxiallly textured despite BaCeO$_3$ formation. This is a clear indication that BaCeO$_3$ should take place after YBCO nucleation on CeO$_2$ surface and therefore, efforts have to be made on YBCO nucleation step. Thus, based on this hypothesis we have focused on studying the YBCO film quality as well as interfacial reaction at different growth temperatures.

8.3.2.3 Quench study

Finally, in this study we tried to establish when TFA-YBCO initially forms on MOD-CGO10 cap layer in order to find a 'sweet spot' where YBCO nucleates c-axis oriented and interface reaction has not extensively occurred.

We have prepared TFA-YBCO quenched films by cooling rapidly during crystallization at 780ºC and at 770ºC. Experimental conditions are described in detail in Fig. 8-15.

To investigate phase evolution, a series of XRD θ-2θ scan of quenched films were performed and compared to a film completely grown (780ºC 90 min), as can be seen in Fig. 8-15. Film quenched from 770ºC exhibit only broad features identified as BaF$_2$ [71]. In sample quenched from 780ºC, detection of (00l) YBCO reflection confirms the initial formation of the YBCO phase. Increase of intensity of diffraction peaks 2θ ≈ 28.8 and 41.2º initially assigned to BaF$_2$ phase, together with slight decrease of I(200)CGO peak reflection are consistent with formation of BaCeO$_3$. Thus, 2θ ≈ 28.8 and 41.2º can be indexed as BaF$_2$ and BaCeO$_3$. As we anticipated in section 8.3.2.2.1, intensity of both contributions can be elucidated. By comparing XRD patterns of film quenched from 780ºC and film quenched after holding 90 min at 780ºC, we observed that after holding 90 min at 780ºC all intermediate phases have been consumed, I(YBCO) Bragg line reflections have strongly increased and it is odd that I(BaCeO$_3$) is almost constant.
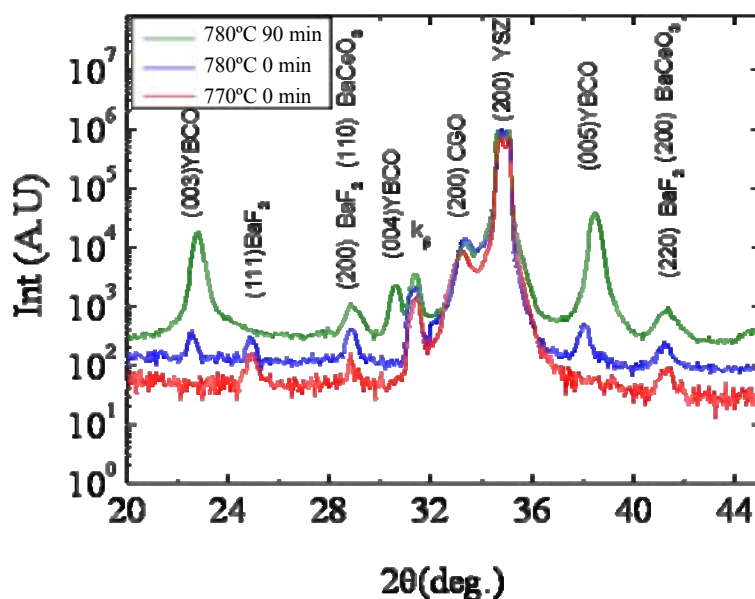
Fig. 8-15 X-ray diffraction patterns of TFA-YBCO film on MOD-CGO10/YSZ quenched from 770ºC, from 780ºC and quenched after holding 90 min at 780ºC.

Interestingly, TEM investigations performed on sample quenched from 780ºC revealed a highly oriented and dense YBCO film in which BaCeO$_3$ formation extends almost all the 30 nm Gd-CeO$_2$ thickness, see Fig. 8-16. According to XRD analysis, two different orientations for BaCeO$_3$ are also detected. The remaining areas were occupied by the epitaxially aligned (200)Gd-CeO$_2$ as exhibited in Fig. 8-16(b). These are the earlier observation of the propensity for the alignment of the (00l) YBCO despite being under layered by BaCeO$_3$, and at the same time, this evidences that YBCO should nucleate onto Gd-CeO$_2$ layer and afterwards starts

interface reaction considering its lattice mismatch parameter (Table 1-I). HRTEM suggests that YBCO growth initially starts from interface of the precursor film and CeO$_2$. The atomically flat terraced areas are usually viewed as the place where the nucleation energy is less than on a rougher surface and thus may provide ideal position for YBCO nuclei. We propose that interface reaction should begin in hillocks/grain boundaries (space between terraces) where Ba-rich precursor could diffuse to CeO$_2$ and form BaCeO$_3$ phase.

Due to YBCO follows an island growth mode, it is suggested that once YBCO nuclei have been formed on atomically flat surface, by coarsening the film covers CeO$_2$ surface and therefore, the subsequent BaCeO$_3$ formations does not much influence on the quality of YBCO epitaxy. Moreover, this hypothesis would support the strong influence of percentage of atomically flat surface on YBCO growth.
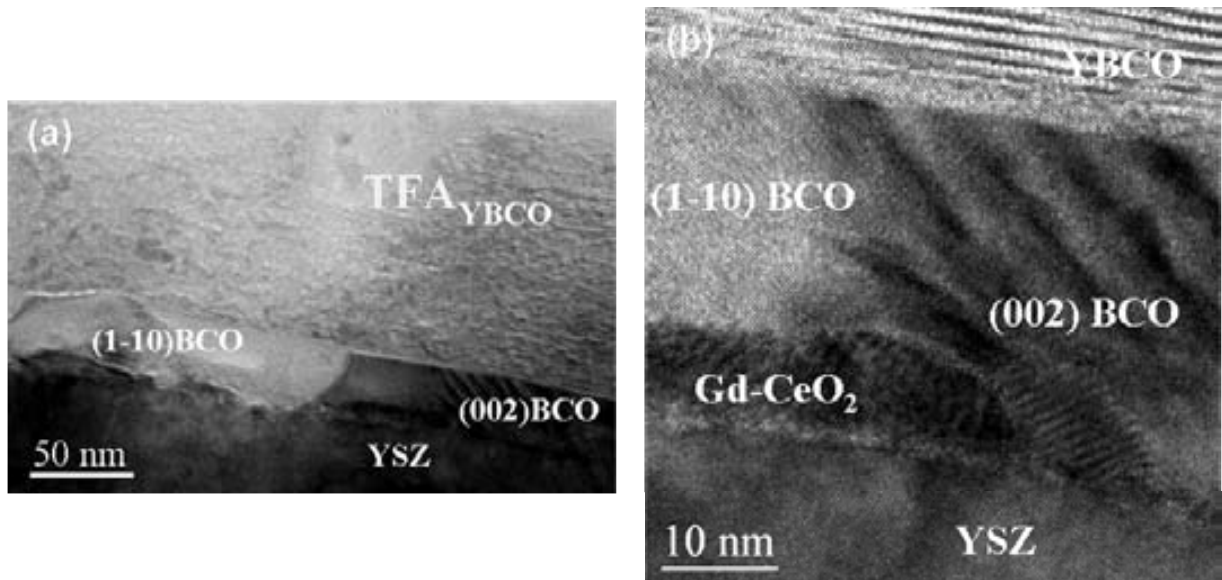
Fig. 8-16 Cross-sectional TEM images viewed along (110) axis of TFA-YBCO quenched film prepared by cooling rapidly after holding at 735ºC for 10 minutes.

Finally, this massive transformation to BaCeO$_3$ at 780ºC explains the fact that in the study of influence of residence time at 780ºC, BaCeO$_3$ content did not increase much further after 60 minutes (wet dwell) at high temperature. From these XRD and TEM investigations we have proposed to replace 780ºC to 770ºC as growth temperature to sluggish interface reaction and therefore improve YBCO epitaxial growth.

8.4 Optimal TFA-YBCO growth process on MOD-CGO10/YSZ single crystal substrate

In accordance with the optimized values found above we settled the following growth parameters: P(O$_2$) = 0.02kPa, P(H$_2$O) = 2.2kPa, gas flow rate = 2.03 x10^{-2} m/s, t= 80 min wet+30 min dry and in Fig. 8-17 it is shown a schematic diagram of the followed heating profile.
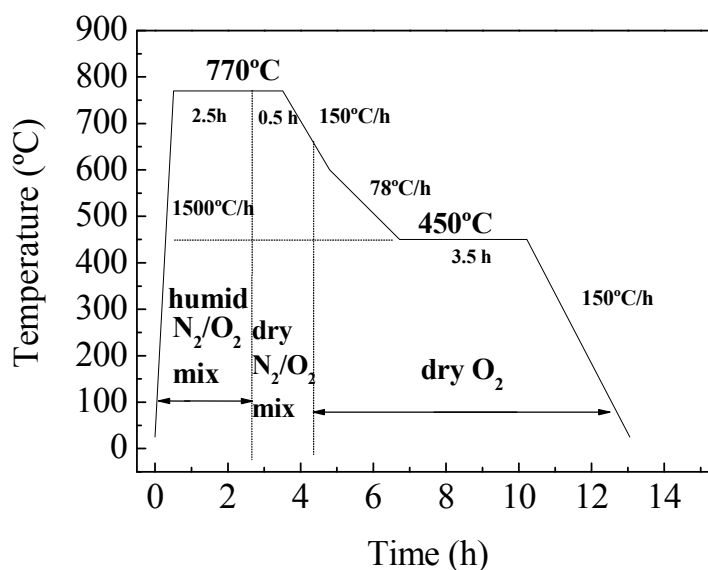
Fig. 8-17 Heating profile for the high-temperature anneal of TFA-YBCO on MOD-CGO10/YSZ substrate.

8.4.1 Structural characterization

XRD θ-2θ scan for this sample, Fig. 8-18, yields stronger (00l) YBCO peak reflections indicating good YBCO films. There is evidence of the formation of BaCeO$_3$ at the end of the process besides CuO and Y$_2$Cu$_2$O$_5$ phases. In this case we have been obtained C$_{BCO}$ =0.54, it does not strongly differ from the previous TFA-YBCO/CGO10/YSZ samples.

However, the high crystalline perfection of the YBCO is demonstrated by the rocking curve value, Δω=0.5º, measured on the (005) reflection, similar value to the CGO cap layer (0.3º). Moreover, this film also shows a good in-plane texture by φ-scan of (103) YBCO= 1.4º, Fig. 8-19. It is a clear improvement in degree of epitaxy from previous TFA-YBCO films. In reality, we achieved similar degree of texture as PLD-YBCO films presented at the beginning of this chapter.
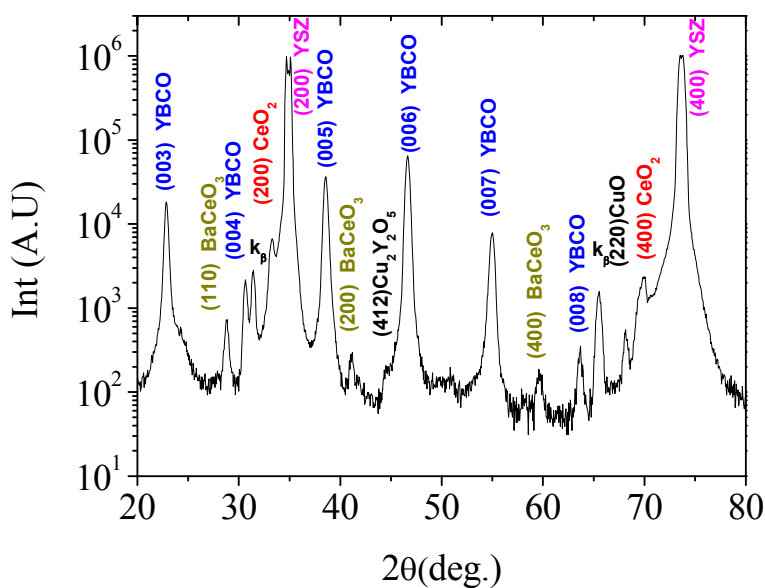
Fig. 8-18 TFA YBCO grown on MOD-CGO/YSZ substrate at 770ºC
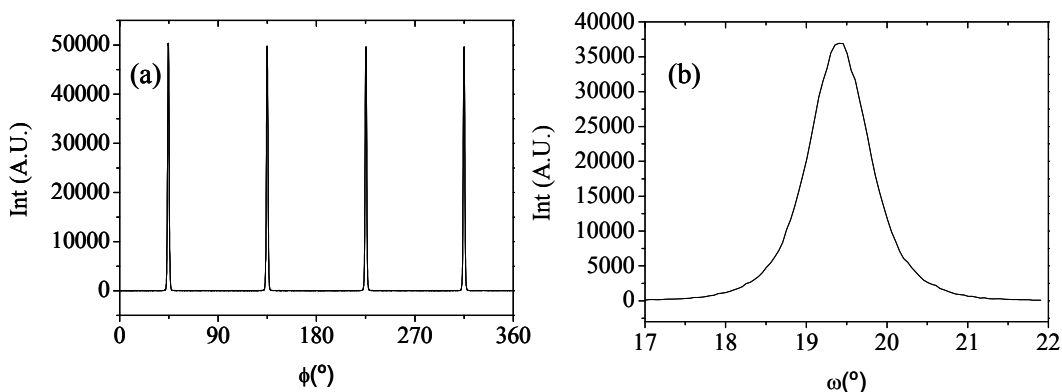
Fig. 8-19 XRD texture analysis of TFA-YBCO film (a) Δφ(103)YBCO =1.3º, (b) Δω(005)YBCO=0.7º

By means of transmission electron microscopy (TEM), it was further investigated YBCO interface quality. Fig. 8-20 shows cross-sectional TEM images of the YBCO film grown on 10%Gd-doped ceria. Well textured YBCO film has been formed coinciding with the results observed in XRD data. BaCeO$_3$ covers nearly the entire YSZ surface (∼30 nm thick) in well agreement with the massive transformation of Gd-CeO$_2$ to Gd:BaCeO$_3$ anticipated in the previous quench studied and in the above XRD θ-2θ scan, Fig. 8-15. In all the areas observed there is no traces of CGO phase, contrasting with XRD θ-2θ scan. However, the interface between the YBCO and Gd-CeO$_2$ is flat and sharp. Taking into account the large mismatch between YBCO and BaCeO$_3$ (Table 1-I), these TEM images are again an evidence that confirm BaCeO$_3$ reacts after YBCO nucleation. HRTEM suggests that YBCO growth initially starts from interface of the precursor film and CeO$_2$. Similar results are recently reported by Matsuda et al.[199] who carried out transmission electron microscopic studies on crystallization of TFA-YBCO film on PLD-CeO$_2$ cap layer.
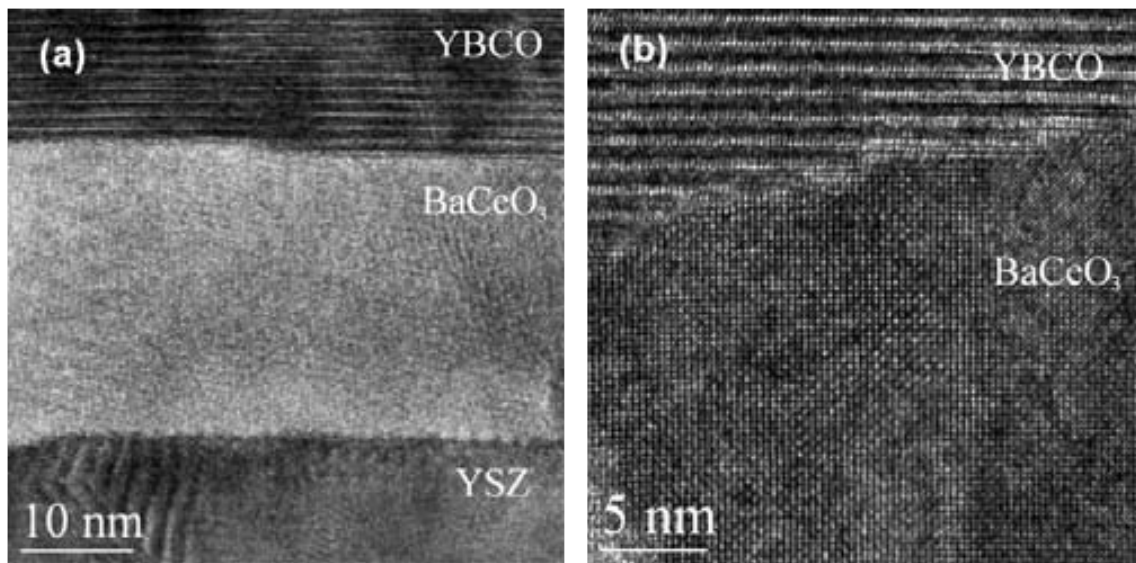
Fig. 8-20 Cross-sectional TEM images of TFA-YBCO film grown at 770ºC by high temperature heating profile on MOD-CGO buffered YSZ.

Notice that these cross sectional TEM images strongly differ from the one observed for TFA-YBCO/sputt-CeO$_2$ (Ar/H$_2$/H$_2$O)/YSZ sequence in Fig. 6-16(b). There, it was hardly observed BaCeO$_3$ phase even if YBCO heating profile was not optimized. This further confirms that interface reaction occurs in less extension between vacuum deposited layers in the TFA-YBCO-CeO$_2$ system. We do not have a clear explanation by such differences between sputt-CeO$_2$ and MOD-CGO10 films but we suggest that high interface reaction in chemical layers is

probably due to an enhaced porosity of the films and hence of the contact surface area among the cap layer and the YBCO film [38,176]. Indeed, considering AFM height profile analysis of both sputtering- CeO$_2$ and MOD-CGO10 films (see Fig.6-3(c) and Fig. 7-23(a)), they can be distinguished by the deepness of voids and hillocks being higher in MOD-CGO10 films.

8.4.2 Superconducting and electrical properties

We found that TFA-YBCO film grown on MOD-CGO10 cap layer through heating profile described in Fig. 8-17 showed the most remarkable effect of improvement in the J_c value at 77K in comparison with YBCO grown on MOD-CeO$_2$ cap layer, as can be seen in Fig. 8-21 In fact, for TFA-YBCO/MOD-CGO10/YSZ single crystal substrate we have calculated J_c ratio of J_c(5K)/J_c (77K)=12.4. This is typical value of high quality and stoichiometric YBCO film. We would like to mention that this ratio has not been computed in the previous samples since all displayed J_c (77K)<10^4 A cm^{-2} which indicates beforehand that the film quality is degraded. Critical current density of TFA-YBCO/MOD-CGO10/YSZ lead highest J_c value of 2.3 MA/cm^2 at 77K and the transition temperature is found to be T$_c$~90K.
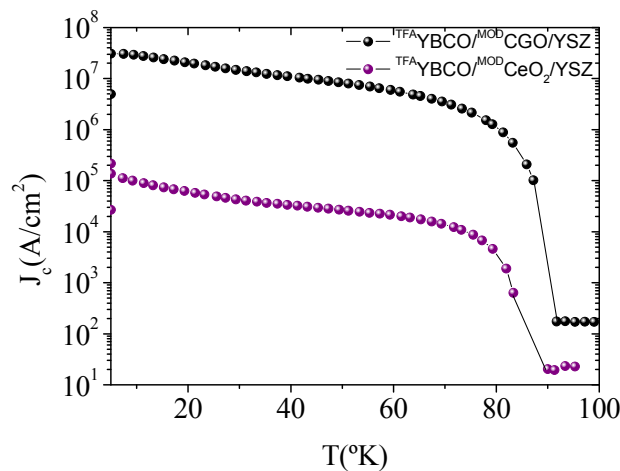
Fig. 8-21 Critical current as a function of temperature of TFA-YBCO thin films grown on MOD-CGO10/YSZ (in black) and MOD-CeO$_2$ /YSZ single crystals (in purple).

From Fig. 8-22 we observed that these films presented a critical temperature of 90 K and that both residual and normal state resistivity values are similar to that obtained for YBCO/LAO model system [34,83] being well consistent with high critical current density showed above.

Therefore, this allows us to conclude that MOD-CGO10 cap layer grown at 900ºC for 8 h in Ar/H$_2$ atmosphere, despite carbon impurities were not fully removed and consequently epitaxial fraction was 77%, it is a very good cap layer to obtain biaxially textured TFA-YBCO film with J_c value of 2.3 MA cm^{-2} at 77K. Thus, this is a feasible cap layer for all-chemical YBCO coated conductors in particular for Ni-RABiT substrates.
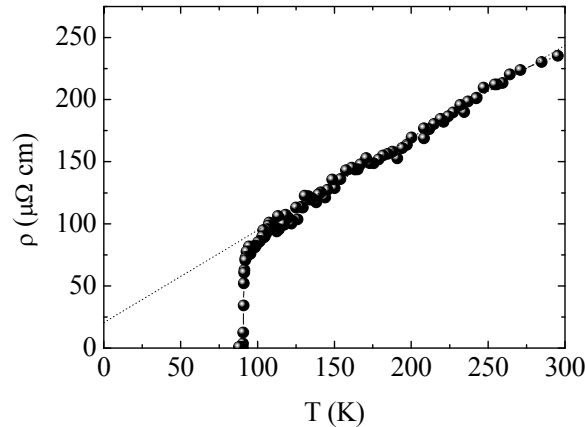
Fig. 8-22 Temperature dependence of resistivity of TFA-YBCO thin film deposited on MOD-CGO10/YSZ single crystal.

Finally, we have studied the dependence of J_c at 77K of TFA-YBCO film on the percentage of atomically flat area of differently processed MOD-modified CeO$_2$ cap layer on YSZ single crystal, similarly to the study carried out on PLD-YBCO films (see section 8.1.2). It is shown in Fig. 8-23. We observe a gradual increase in the J_c value from 0 to ≥70% contrasting with a sharp transition in PLD-YBCO films, see Fig. 8-6. In this case, 30% of atomically flat area is not enough to obtain fully biaxial YBCO film and it is reflected by J_c (77K) ∼ 1.8 MA cm^{-2}. Further investigation is required to determine if beyond 80% of atomically flat area, J_c value saturates. Anyway, this demonstrates that TFA-YBCO film is more sensitive to the percentage of atomically flat area of CeO$_2$ cap layer than PLD films. These effects are not surprising considering that growth mode of PLD (bi-dimentional growth) and CSD films (island coalescence) are completely different as well as deposition route as we anticipated in section 1.2.3.2.2). Therefore, parameters like contact surface area, residence time at high temperature as well as pathway reaction make CSD film more sensitive to quality of the underlying film. However, we have demonstrated that by modifying TFA-YBCO growth parameters we can

favour the accommodation of c-axis nuclei on CeO$_2$ surface and achieve high quality film similar to vacuum deposited films.
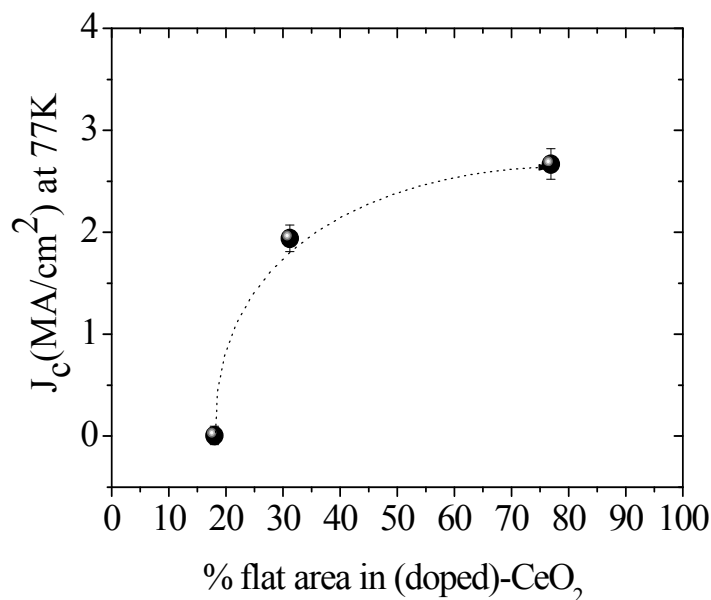
Fig. 8-23 Dependence of Jc at 77K for MOD-YBCO films as a function of atomically flat area of the underlying MOD-modified CeO$_2$ buffer layer

8.5 Conclusions

In this chapter we have described an important advance in processing TFA-YBCO films on MOD- doped ceria buffered YSZ single crystal with J_c value of 2.3 MA/cm^2 at 77K.

We have analyzed the influence of MOD-CeO$_2$ cap layer quality on both PLD and TFA YBCO epitaxy and superconducting properties. In particular we have presented evidences that percentage of atomically flat area and high texture of CeO$_2$ cap layer determine YBCO film quality, rather than BaCeO$_3$ formation.

We have observed that CeO$_2$ films with low percentage of atomically flat area (~18%) and fibre texture induce partially epitaxial PLD-YBCO films and BaCeO$_3$ formation (C$_{BCO}$ ≈0.21). As a result, J_c values fall down to 10^5 A cm^{-2} at 77K. By contrast, doped CeO$_2$ with 10%

of Gd^{3+} or Zr^{4+}, which improved epitaxial fraction and increase the percentage of flat area above 30% leads to biaxially textured PLD-YBCO film with J_c values of 3MA cm^{-2} at 77K . In this case, interface reaction has been minimized (C$_{BCO}$ ~0.11).

We have investigated the influence of 10% Gd^{3+}doped-CeO$_2$ cap layer quality (grown at different time and temperature) on TFA-YBCO growth. It is particularly remarkable that TFA-YBCO film is more sensitive to the underlying surface layer than PLD-YBCO film. Around 70% of atomically flat area in CGO10 was required to obtain J_c values around 1.5 MA cm^{-2} at 5K which is quite far from the values obtained for PLD-YBCO film grown on the same cap layer. Additionally, we observed that BaCeO$_3$ phase has been formed in more extension in these all-chemical deposited systems (C$_{BCO}$ ≈0.54). This has been mainly attributed to the different growth mode of YBCO. However, TFA-YBCO film quality grown on the optimal CGO10 cap layer (grown at 900ºC for 8h in Ar/H$_2$) has been strongly improved by modifying growth parameters (time, temperature and P(H$_2$O)).

We have carried out a systematic study of the influence of residence time (wet) at high temperature on YBCO film quality. We have investigated the range of 45-150 min in wet atmosphere and optimal results have been obtained for t (wet)= 60 min. Shorter time (45 min) the quality of the YBCO film is degraded due to intermediate phases have not been fully converted. By contrast, at long processing time (t=150 min), the main consequence of film degradation is the long exposure to wet atmosphere at high temperature.

Then, we have carried out a systematic study of the influence of P(H$_2$O) on TFA-YBCO film quality at 780ºC and total residence time of 90 min (60 min wet and 30 min dry). Once more we have observed high interface reactivity. Low J_c observed for P(H$_2$O)=0.6 and 3.3 kPa has been associated to poor YBCO texture induced by uncompleted reaction and HF gas stagnancy respectively. Concomitantly, it has been analysed the influence of H$_2$O during the heating rate incorporating H$_2$O in the gas flow at 780ºC (we usually switch on wet atmosphere at 100ºC). For this case, we have also detected an incomplete conversion. Optimal film quality has been detected for P(H$_2$O)=2.2 kPa.

By TEM analysis of quenched sample from 780ºC we have observed that c-axis YBCO grains have been nucleated and grown and 30nm-thick CGO10 cap layer has nearly converted to Gd:BaCeO$_3$. High alignment of YBCO grains has suggested that c-axis YBCO firstly nucleates on CeO$_2$ films which provide lower lattice mismatch than BaCeO$_3$ and then, interface reaction occurs. From this study we have lowered growth temperature from 780ºC to 770ºC and we have successfully improved the epitaxial growth of TFA-YBCO film. We have found TFA-YBCO film carrying J_c (77K) ~2.3 MA cm^{-2} and excellent texture even CGO10 cap layer has fully

converted to Gd:BaCeO$_3$. Therefore, it has been verified that despite CGO10 film grown at 900ºC for 8 h in Ar/H$_2$ atmosphere still retained some carbon and therefore it was not fully epitaxial, it can be a potential cap layer for all-chemical YBCO coated conductor.

We have confirmed that when YBCO growth is carried out on different substrate than LAO [99], growth temperature, P(H$_2$O) and time of growth have to be shifted due to modified relative interfacial energies and chemical compatibility.

By contrasting YBCO film grown on MOD-CGO10 and sputt-CeO$_2$ we have found that in the latter interface reaction occurs in less extension. We have suggested that this is due to MOD-CGO10 films displays higher surface imperfections (hillocks, porosity, voids). However, by optimizing TFA-YBCO growth parameters we have overcame those surface problems obtaining higher critical current density than no-optimized TFA-YBCO film on sputt-CeO$_2$ cap layer.

CHAPTER 9

GENERAL CONCLUSIONS

We have successfully demonstrated that chemical solution deposition (CSD) is a very competitive technique for obtaining epitaxial buffer and superconducting layers of high quality and with high critical currents for coated conductor fabrication.

Several conductor architectures based on YBCO are possible. However, the optimum oxide buffer combination depends on the metallic substrate. Two types of metallic substrates have been considered in this Thesis: polycrystalline stainless steel and Ni-RABiT. For these substrates, $SrTiO_3$ and CeO_2 are the cap layers which have attracted more attention and consequently, we have investigated the growth conditions of these buffers based on CSD to obtain high quality interfaces in multilayered systems. We have also investigated the stability and growth of TFA-YBCO film over the underlying cap layers

We have first investigated the stability of YBCO film deposited by the trifluoracetate (TFA) route on single crystals substrates: $SrTiO_3$ (STO) and $LaAlO_3$ (LAO) or buffered single crystal substrates: $BaZrO_3/LaAlO_3$ (BZO/LAO) as model systems of multilayered architectures. In this study we have given for the first time evidence that a homogeneous structure of heteroepitaxial TFA-YBCO films is unstable. We have demonstrated that under certain conditions of film thickness, growth or post-processing annealing strongly dewetted films can be generated. TEM investigations have confirmed that the YBCO migration process from the interface is complete in the dewetted areas. These areas display well defined geometrical features with parallepipedic-like shapes in order to stabilize low energy surfaces. Moreover we have established that the film instability is a mechanism to relief the stress induced at the interface by the lattice misfit between the YBCO film and the single crystal substrates LAO, STO and BZO buffer layers.

Finally, we have been able to describe this phenomenon on the basis of free-energy analysis which is of general validity for YBCO films.

Then, we have focused our work on investigating the influence of the quality of the interface of cap layers on the superconducting properties of TFA-YBCO films. We have considered two different cap layers which are promising candidates for the production of all-chemical coated conductors because they properly match the criteria of protection of the metallic substrates from oxidation, they display low lattice mismatch with YBCO and they can develop high-quality interfaces: STO, with perovskite structure, and CeO_2, with fluorite structure.

We have investigated mechanisms to control the interfacial quality of perovskite STO cap layer grown by CSD on single crystal substrates (STO and LAO) and on MOD-BZO buffered LAO single crystal as model systems for conductors. We have focused on reducing atmospheres which can be used in architectures for Ni-RABiT.

We have obtained epitaxial films, with homogeneous surface morphology consisting in rounded nanometric grains even when high lattice mismatches must be overcome, as in the case of STO/BZO/LAO. Because of this surface morphology consisting on connected globular grains, the surface quality can be determined either by rms roughness or from the percentage of atomically flat area. We have found a certain range of variability in surface roughness in the case of STO/BZO/LAO architecture which can actually be controlled through modifying buffer layer growth temperatures. We have observed that surface roughness has direct implications in the growth and properties of TFA-YBCO films. We have proved that an increased roughness leads to an enhancement of the nucleation of a/b axis oriented grains, and, as a consequence, the residual porosity of TFA-YBCO films is increased with the subsequent deterioration of the superconducting properties.

Control of the interfacial quality of CeO_2 cap layer has also been investigated in detail. We have studied first the influence of annealing treatments on highly epitaxial vacuum deposited CeO_2 cap layer on the final quality of TFA-YBCO films and this knowledge has been used to achieve highly epitaxial and atomically flat CeO_2 cap layers grown by chemical solution deposition.

We have observed that (001)-terraced surfaces in CeO_2 greatly improve the superconducting properties of the TFA-YBCO overlayers grown on them. This feature, not detected in perovskite cap layers, stressed the difference between a statistical parameter such as rms roughness and the percentage of atomically flat area to quantify the surface quality. In this case, the use of rms roughness is a non meaningful parameter and the critical factor to evaluate the quality of ceria surface morphology is the percentage of atomically flat area.

Oxygen atmosphere stabilizes (001)-flat terraced surfaces through some kind of film reconstruction in both vacuum and chemical solution deposited CeO_2 cap layers. However, this

atmosphere cannot be used on Ni substrates because it oxidizes them. Alternatively, as a first approach, we have investigated the influence of other processing atmospheres on highly epitaxial sputtering-CeO_2 films. Whereas Ar/H_2 atmosphere degrades the surface morphology resulting in an inhomogeneous topography, $Ar/H_2/H_2O$ atmosphere has successfully stabilized (001)-flat terraces. It is likely that in this wet atmosphere hydroxyl groups play a special role in stabilizing the (001)-polar CeO_2 surface.

Epitaxy development and stabilization of (001)-flat surfaces in MOD-CeO_2 films have not been straightforward in reducing (95%Ar/5%H_2) atmosphere. This atmosphere, actually, hinders the elimination of carbon content from metalorganic precursors and it blocks the fully epitaxial growth (∼18% of epitaxial fraction). To reduce carbon content in film we have investigated different alternatives: (1) the use of partial oxidizing atmospheres (2) the nature of precursor solution (3) the incorporation of dopant agents.

Ar/H_2 atmosphere with different contents of oxygen ($Ar/H_2/H_2O$, O_2+Ar/H_2) have not provided enough mobility and chemical exchange to remove all carbon (Ce-C) trapped in grain boundaries. On the other hand, by modifying chemical precursors we have slightly improved the epitaxial fraction from ∼18% to ∼38%) but without stabilizing the (001)-surface. This improvement has been related to a modification of the decomposition pathway of organic precursor through formation of isoprene.

Then, we have explored an alternative route: the incorporation of dopant agents (Gd^{3+}, Zr^{4+}). Interestingly, both cations introduce and enhance atomic mobility by creation of oxygen vacancies, however, the mechanism of oxygen vacancy formation strongly differs in both cases. Whereas for Gd^{3+} it appears to be related with charge compensation effect, while by Zr^{4+} the small ionic radius emerge as the key parameter to stabilize interstitial defects.

We have demonstrated, after detailed optimization of Gd-doped CeO_2 films, that many parameters influence the atomic mobility in CeO_2 films: carbide impurities, dopant concentration and growth conditions (atmosphere, time and temperature). Indeed, we detected a gradual increase in the epitaxial fraction and the percentage of atomically flat area running in parallel to the elimination of carbon content.

The films with optimum performances obtained in Ar/H_2 atmosphere have been 10%Gd-doped CeO_2 (CGO10) grown at 900ºC for 8h. Under these reducing conditions we obtained ∼77% of epitaxial fraction and ∼71% of (001)-atomically flat area. No influence of adding H_2O in the gas flow was detected in this case. It is likely that in this case oxygen vacancies already stabilize the (00l) polar surface and the hydroxyl groups do not play any additional role. Improving the epitaxy (> 80% of epitaxial fraction) simultaneously with stabilizing (001)-flat terraced surface could only be achieved under pure oxygen atmosphere.

Highly biaxially TFA-YBCO films have been successfully grown on high quality (001)-terraced CeO_2 films. We have obtained self-field J_c values at 77K of 1.5MA cm^{-2} in sputtering-CeO_2/YSZ single crystal substrates and 0.3MA cm^{-2} in sputtering-CeO_2/YSZ/CeO_2/Ni-RABiT substrates. We have been able also to develop high quality TFA-YBCO films on MOD-(001)-10%-Gd-CeO_2 cap layer, after a detailed optimization of growth parameters, displaying very promising superconducting performances, J_c of 2.3MA cm^{-2} at 77K. Interestingly, TFA-YBCO films are more sensitive to the quality of the underlying cap layers and we have shown that a higher percentage of atomically flat area (~70 versus ~30%) is needed to obtained similar film properties as YBCO films deposited by pulsed laser deposition (PLD), J_c of 3MA cm^{-2} at 77K. In both systems we have detected interface reaction between YBCO film and CeO_2 cap layers, leading to $BaCeO_3$ formation.

Chemical reactivity has been found higher in all-chemical multilayers, this is probably due to an enhanced porosity of the films and hence of the contact surface among the cap layer and the YBCO film. However, we have demonstrated that interfacial reaction does not preclude the attainment of high J_c values because it generally occurs after the nucleation of the epitaxial YBCO film at the interface with the cap layer. Our work shows then that a high percentage of atomically flat area in CeO_2 cap layers is the key parameter to favor c-axis YBCO grain nucleation and therefore reaching biaxially textured YBCO film and high critical currents.

FUTURE WORK

Our work has rised, on the other hand, several issues that still remain unanswered, and therefore it suggests new research areas that should be investigated in the future. It would be very appealing to reach a deeper understanding of the process involved in the carbon content elimination in CeO_2 films, keeping a reducing atmosphere. The interplay between the nature of precursor solutions and defect structure of the fluorite CeO_2 seems to be the key issue here. More specifically it would be interesting to study an alternative way to increase the atomic mobility in ceria films in order to beyond 80% in epitaxial fraction and ~77% in atomic flatness and hence, achieve a final film quality similar to that obtained under pure oxygen atmosphere. To reach this objective it is needed to understand the mechanism by which the incorporation of Gd^{3+}, or even other dopant agents, enhances the C elimination.

Another issue that remains to be investigated is the relationship between the TFA-YBCO growth conditions and the surface quality of CeO_2 cap layers. We can wonder if the sensitiveness of TFA-YBCO layers to the cap layer quality could be decreased to values similar to those found by PLD growth.

Finally, the other field in which an extensive work still remains to be done is in MOD-STO cap layers. This regard the issue that we consider more appealing to improve the STO cap layer surface quality (develop terraced surfaces for instance) and hence to further optimize the YBCO texture quality and critical currents when growth is performed on this perovskite cap layer.

We would like to conclude this work by indicating that the knowledge generated in the preparation of the different CSD multilayers can be now transferred to metallic substrates, particularly to the RABIT substrates fabricated by Nexans Superconductors, and so it is expected that in a very near future long length 'all chemical' coated conductors will be achieved with high performances.

BIBLIOGRAPHY

1. J.R.Waldram,*"Superconductivity of Metals and Cuprates"* , Edited by Institut of Physics Publishing (1996)

2. J.R.Gavaler, M.A.Janocko, and C.S.Jones,*"Superconductivity in Nb-Ge films above 22K"* Appl. Phys. Lett. **23**, 480 (1973)

3. J.Bardeen, L.N.Cooper, and J.R.Schrieffer,*"Theory of Superconductivity"* Physical Review **108**, 1175 (1957)

4. J.G.Bednorz and K.A.Müller,*"Possible High-Tc Superconductivity in the Ba-La-Cu-O System"* Zeitschrift fur Physik B-Condensed Matter **64**, 189 (1986)

5. M.K.Wu, J.R.Ashburn, C.J.Torng, P.H.Hor, R.L.Meng, L.Gao, Z.J.Huang, Y.Q.Wang, and C.W.Chu,*"Superconductivity at 93 K in a New Mixed-Phase Y-Ba-Cu-O Compound System at Ambient Pressure"* Physical Review Letters **58**, 908-912 (1987)

6. D.C.Larbalestier,*"Power Applications of Superconductivity in Japan and Germany (World Technology and Engineering Center)"* , Loyola College, MD, September (1997)

7. A.Schilling, M.Cantoni, J.D.Guo, and H.R.Ott,*"Superconductivity above 130K in the Hg-Ba-Ca-Cu-O system"* Nature **363**, 56 (1993)

8. F.Beech, S.Miraglia, A.Santoro, and R.S.Roth,*"Neutron Study of the Crystal-Structure and Vacancy Distribution in the Superconductor $Ba_2YCu_3O_{9-\delta}$"* Physical Review B **35**, 8778 (1987)

9. V.Breit, P.Schweiss, R.Hauff, H.Wühl, H.Claus, H.Rietschel, A.Erb, and G.Müller-Vogt,*"Evidence for chain superconductivity in near-stoichiometry $YBa_2Cu_3O_x$ single crystals"* Physical Review B **52**, 15727 (1995)

10. G.Blatter, M.V.Feigelman, V.B.Geshkenbein, V.B.Larkin, and A.I.Vinkour,*"Vortices in high-temperature superconductors"* Rev. Mod. Phys. **66**, 1125 (1994)

11. D.C.Larbalestier, A.Gurevich, D.M.Feldmann, and A.Polyanskii,*"High-T_c superconducting materials for electric power applications"* Nature **414**, 368 (2001)

12. M.Paranthaman and T.Izumi,*"High-Performance YBCO-Coated Superconductor Wires"* Materials Research Bulletin **8**, 533 (2004)

13. K.Heine, J.Tenbrink, and M.Thoner,*"High-Field Critical Current Densities in $Bi_2Sr_2Ca_1Cu_2O_{8+x}$/Ag Wires"* Appl. Phys. Lett. **55**, 2441 (1989)

14. A.Goyal, M.Paranthaman, and U.Schoop,*"The RABITS Approach:Using Rolling-Assisted Biaxially Textured Substrates for High-Performance YBCO Superconductors"* Materials Research Bulletin **8**, 552 (2004)

15. Y.Iijima, K.Kakimoto, Y.Yamada, T.Izumi, T.Saitoh, and Y.Shiohara,*"Research and Development of Biaxially Textured IBAD-GZO Templates for Coated Conductors"* Materials Research Bulletin **8**, 564 (2004)

16. D.Dimos, P.Chaudhari, J.Mannhart, and F.K.Legoues,*"Orientation Dependence of Grain-Boundary Critical Currents in $YBa_2Cu_3O_{7-\delta}$ Bicrystals"* Physical Review Letters **61**, 219 (1988)

17. Y.Iijima and K.Matsumoto,*"High-temperature-superconductor coated conductors: technical progress in Japan"* Superconductor Science & Technology **13**, 68 (2000)

18. M.Ohring,*"Materials Science of Thin Films, Deposition and structure"* 2nd Edition, Academic Press, New York , 412-430 (2005)

19. J.W.Matthews,*"Coherent Interfaces and Misfit Dislocations"* Ed. by J. W. Matthes, Academic Press , 559 (1975)

20. *"Inorganic Crystal Structure Database, ICSD-for-WWW"* Fachinformationszentrum Karlsruhe (FIZ) and National Institute of Standards and Technology (NIST) (2005)

21. A.Goyal, D.P.Norton, J.D.Budai, M.Paranthaman, E.D.Specht, D.M.Kroeger, D.K.Christen, Q.He, B.Saffian, F.A.List, D.F.Lee, P.M.Martin, C.E.Klabunde, E.Hartfield, and V.K.Sikka,*"High critical current density superconducting tapes by epitaxial deposition of $YBa_2Cu_3O_x$ thick films on biaxially textured metals"* Appl. Phys. Lett. **69**, 1795 (1996)

22. Y.Iijima, N.Tanabe, O.Kohno, and Y.Ikeno,*"Inplane Aligned $YBa_2Cu_3O_{7-X}$ Thin-Films Deposited on Polycrystalline Metallic Substrates"* Appl. Phys. Lett. **60**, 769 (1992)

23. X.D.Wu, S.R.Foltyn, P.N.Arendt, W.R.Blumenthal, I.H.Campbell, J.D.Cotton, J.Y.Coulter, W.L.Hults, M.P.Maley, H.F.Safar, and J.L.Smith,*"Properties of $YBa_2Cu_3O_{7-\delta}$ Thick-Films on Flexible Buffered Metallic Substrates"* Appl. Phys. Lett. **67**, 2397 (1995)

24. K.Matsumoto, K.Kim, K.Yamagiwa, Y.Koike, I.Hirabayashi, T.Watanabe, N.Uno, and M.Ikeda,*"High critical current density $YBa_2Cu_3O_{7-d}$ films on surface-oxidized metallic substrates"* Physica C **335**, 39 (2000)

25. M.Bauer, R.Semerad, and H.Kinder,*"YBCO films on metal substrates with biaxially aligned MgO buffer layers"* IEEE Transaction on Applied Superconductivity **9**, 1502 (1999)

26. K.Matsumoto, S.B.Kim, I.Hirabayashi, T.Watanabe, N.Uno, and M.Ikeda,*"High critical current density $YBa_2Cu_3O_{7-\delta}$ tapes prepared by the surface-oxidation epitaxy method"* Physica C **330**, 150 (2000)

27. A.Usoskin, J.Dzick, A.Issaev, J.Knoke, F.Garcia-Moreno, K.Sturm, and H.C.Freyhardt,*"Critical currents in long-length YBCO-coated conductors"* Superconductor Science & Technology **14**, 676 (2001)

28. M.Varela, D.Arias, Z.Sefrioui, C.Leon, C.Ballesteros, and J.Santamaria,*"Epitaxial mismatch strain in $YBa_2Cu_3O_{7-\delta}/PrBa_2Cu_3O_7$ superlattices"* Physical Review B **62**, 12509 (2000)

29. R.Feenstra, A.Gapud, F.A.List, E.D.Specht, C.W.Chu, T.G.Holesinger, and D.M.Feldmann,*"Critical currents I_c (77K) >350A/cm-width achieved in ex situ YBCO coated conductors using a faster conversion process"* IEEE Transaction on Applied Superconductivity **15**, 2803 (2005)

30. H.Yamane, T.Hirai, K.Watanabe, N.Kobayashi, Y.Muto, M.Hasei, and H.Kurosawa,*"Preparation of a high Jc Y-Ba-Cu-O film at 700 ℃ by thermal chemical vapor-deposition"* J. Appl. Phys. **69**, 7948 (1991)

31. Y.Yamada,*"Liquid-phase epitaxy processing of $RBa_2Cu_3O_{7-\delta}$"* Superconductor Science & Technology **13**, 82 (2000)

32. A.Gupta, R.Jagannathan, E.I.Cooper, E.A.Giess, J.I.Landman, and B.W.Hussey,*"Superconducting Oxide-Films with High Transition-Temperature Prepared from Metal Trifluoroacetate Precursors"* Appl. Phys. Lett. **52**, 2077 (1988)

33. P.C.McIntyre, M.J.Cima, M.F.Ng, R.C.Chiu, and W.E.Rhine,*"Texture Development in $Ba_2YCu_3O_{7-X}$ Films from Trifluoroacetate Precursors"* J. Mater. Res. **5**, 2771 (1990)

34. X.Obradors, T.Puig, A.Pomar, F.Sandiumenge, N.Mestres, M.Coll, A.Cavallaro, N.Roma, J.Gazquez, J.C.Gonzalez, O.Castano, J.Gutierrez, A.Palau, K.Zalamova, S.Morlens, A.Hassini, M.Gibert, S.Ricart, J.M.Moreto, S.Piñol, D.Isfort, and J.Bock,*"Progress Towards all-chemical superconducting YBCO coated-conductors"* Superconductor Science & Technology **19**, s1 (2006)

35. M.P.Paranthaman, T.Aytug, H.Y.Zhai, L.Heatherly, A.Goyal, and D.K.Christen,*"Growth of YBCO films on MgO-based rolling-assisted biaxially textured substrates templates"* Superconductor Science & Technology **18**, 223 (2005)

36. A.Usoskin and H.C.Freyhardt,*"YBCO-coated conductors manufactured by high-rate pulsed laser deposition"* Mrs Bulletin **29**, 583 (2004)

37. P.N.Arendt and S.R.Foltyn,*"Biaxially Textured IBAD-MgO templates for YBCO-Coated Conductors"* Materials Research Bulletin **8**, 543 (2004)

38. A.Cavallaro, F.Sandiumenge, J.Gazquez, T.Puig, X.Obradors, J.Arbiol, and H.C.Freyhardt,*"Growth mechanism, microstructre and surface modification of nanostructured CeO_2 films by chemical solution deposition"* Advanced Functional Materials **16**, 1363 (2006)

39. T.G.Holesinger, S.R.Foltyn, P.N.Arendt, Q.X.Jia, P.C.Dowden, R.F.DePaula, and J.R.Groves,*"A comparison of buffer layer architectures on continuously processed YBCO coated conductors based on the IBAD YSZ process"* IEEE Transaction on Applied Superconductivity **11**, 3359 (2001)

40. T.Muroga, H.Iwai, Y.Yamada, T.Izumi, Y.Shiohara, Y.Iijima, T.Saito, T.Kato, Y.Sugawara, and T.Hirayama,*"Pulsed laser deposition method-CeO$_2$ buffer layer for YBCO coated conductor"* Physica C **392-396**, 796 (2003)

41. D.P.Norton, A.Goyal, J.D.Budai, D.K.Christen, D.M.Kroeger, E.D.Specht, Q.He, B.Saffian, M.Paranthaman, C.E.Klabunde, D.F.Lee, B.C.Sales, and F.A.List,*"Epitaxial YBa$_2$Cu$_3$O$_7$ on biaxially textured nickel (001): An approach to superconducting tapes with high critical current density"* Science **274**, 755 (1996)

42. M.Paranthaman, S.Sathyamurhy, M.S.Bhuiyan, A.Goyal, T.Kodenkandath, X.Li, W.Zhang, C.Thieme, U.Schoop, D.T.Verebelyi, and M.W.Rupich,*"Improved YBCO Coated Conductors Using Alternate Buffer Architectures "* IEEE Trans. on Appl. Supercond. **15**, 2632 (2005)

43. S.Sathyamurhy, M.Paranthaman, L.Heatherly, P.M.Martin, E.D.Specht, A.Goyal, T.Kodenkandath, X.Li, and M.W.Rupich,*"Solution-processed lanthanum zirconium oxide as a barrier layer for high I$_c$-coated conductors"* J. Mater. Res. **21**, 910 (2006)

44. E.Stewart, M.S.Bhuiyan, S.Sathyamurhy, and M.Paranthaman,*"Studies of solution deposited cerium oxide thin films on textured Ni-alloy substrates for YBCO superconductor"* Materials Research Bulletin **41**, 1063 (2006)

45. J.M.Phillips, M.P.Siegal, R.B.van Dover, T.H.Tiefel, J.H.Marshall, A.J.Strauss, R.E.Fahey, S.Sengupta, A.Cassanho, and H.P.Jenssen,*"Comparison of YBCO thin films grown on various perovskite substrates by coevaporation"* J. Mater. Res. **7**, 2650 (1992)

46. K.Matsumoto, A.Takechi, T.Ono, I.Hirabayashi, and K.Osamura,*"Effect of perovskite oxide cap layer on superconducting properties of YBa$_2$Cu$_3$O$_x$ films grown on mechanically polished SOE substrates"* Physica C **392-396**, 830 (2003)

47. R.Hühne, B.Holzapfel, A.Kursumovic, J.E.Evetts, A.Cavallaro, F.Sandiumenge, A.Pomar, T.Puig, and X.Obradors,*"Preparation of MZrO$_3$ (M=Ba,Sr) Buffer layers on surface oxidized Ni/NiO templates by PLD and MOD"* IEEE Trans. on Appl. Supercond. **15**, 3024 (2005)

48. A.Pomar, A.Cavallaro, M.Coll, J.Gazquez, F.Sandiumenge, T.Puig, X.Obradors, and H.C.Freyhardt,*"All Chemical YBaCuO Coated Conductors on IBAD/YSZ Substrates"* Superconductor Science & Technology **19**, L1 (2006)

49. A.Pomar, M.Coll, A.Cavallaro, J.Gazquez, J.C.Gonzalez, N.Mestres, F.Sandiumenge, T.Puig, and X.Obradors,*"All-chemical high-Jc YBa$_2$Cu$_3$O$_7$ multilayers with SrTiO$_3$ as cap layer"* J. Mater. Res. **21**, 1106 (2006)

50. M.P.Siegal, P.G.Clem, J.T.Dawley, J.Richardson, D.L.Overmyer, and T.G.Holesinger,*"Optimizing SrTiO$_3$ films on textured Ni substrates using chemical solution deposition"* J. Mater. Res. **20**, 910 (2005)

51. C.Brinker and G.W.Scherer,*"Sol-Gel Science: The Physics and Chemistry of Sol-Gel Processing"* , New York (1990)

52. J.D.Mackenzie and E.Bescher,*"Some factors governing the coating of organic polymers by sol-gel derived hybrid materials"* J. Sol-Gel Sci. Technol. **27**, 7 (2003)

53. R.W.Schwartz, T.Schneller, and R.Waser,*"Chemical solution deposition of electronic oxide films"* Comptes Rendus Chimie **7**, 433 (2004)

54. D.E.Bornside, C.W.Macosko, and L.E.Scriven,*"On the Modeling of Spin Coating"* Journal of Imaging Technology **13**, 122 (1987)

55. M.Huffmann,*"Liquid source misted chemical deposition (LSMCD) - a critical review"* Integrated Ferroelectrics **10**, 39 (1995)

56. R.T.Morrison and R.N.Boyd,*"Organic Chemistry"* , 3rd Edition, Allyn and Bacon, Inc., Boston (1974)

57. J.M.Phillips,*"Substrate selection for high-temperature superconducting thin films"* J. Appl. Phys. **79**, 1829 (1996)

58. P.K.Coffman and S.K.Dey,*"Structure evolution in the $PbO-ZrO_2-TiO_2$ sol-gel system: PartI-Characterization of prehydrolyzed precursors"* Journal of Sol-Gel Science and Tecnology **1**, 251 (1994)

59. R.W.Schwartz, R.A.Assink, and T.J.Headley,*"Solution Chemistry Effects in PZT Thin Film Processing: Spectroscopic and Microstructural Characterization, in Ferroelectric Thin Films II"* Materials Research Society Symposium Proceeding **243**, 245 (1992)

60. M.Liu and D.Wang,*"Preparation of $La_{-z}Sr_zCo_{1-y}Fe_yO_{3-x}$ thin films, membrnes and coatings on dense and porous substrates"* J. Mater. Res. **10**, 3210 (1995)

61. M.S.G.Baythoun and F.R.Sale,*"Production of Strontium-Substituted Lanthanum Manganite Perovskite Powder by the Amorphous Citrate Process"* Journal of Materials Science **17**, 2757 (1982)

62. M.F.Ng and M.J.Cima,*"Heteroepitaxial growth of lanthanum aluminate films derived from mixed metal nitrates"* J. Mater. Res. **12**, 1306 (1997)

63. F.Parmagiani, G.Chiarello, N.Ripamonti, H.Goretzki, and U.Roli,*"Observation of carboxylic groups in the lattice of sintered $Ba_2YCu_3O_{7-\delta}$ high-Tc superconductors"* Physical Review B **36**, 7148

64. Y.Xu, A.Goyal, K.J.Leonard, E.D.Specht, D.Shi, and M.Paranthaman,*"Processing Dependence of Texture, and Critical Properties of YBCO films on RABITS substrates by a Non-Fluorine MOD method"* Journal of American Ceramic Society **89**, 914 (2006)

65. G.W.Scherer,*"Sintering of Sol-Gel films"* Journal of Sol-Gel Science and Tecnology **8**, 353 (1997)

66. R.W.Schwartz, P.G.Clem, J.A.Voigt, E.R.Byhoff, M.Van Stry, T.J.Headley, and N.A.Missert,*"Control of Microstructure and Orientation in Solution-Deposited BaTiO₃ and SrTiO₃ Thin Films"* Journal of American Ceramic Society **82**, 2359 (2006)

67. J.W.Christian,*"The Theory of Transformations in Metals and Alloys. Part I"* Pergamon, New York , 420 (1975)

68. R.Roy,*"Gel Route to Homogeneous Glass Preparation"* Journal of American Ceramics Society **52**, 344 (1969)

69. K.T.Miller and F.F.Lange,*"Processing Science of Advanced Ceramics"* Materials Research Society,Pittsburg,PA , 191,Edited by I.A.Aksay,G.I.McVay and D.R.Ulrik (1989)

70. F.Sandiumenge, A.Cavallaro, J.Gazquez, T.Puig, X.Obradors, J.Arbiol, and H.C.Freyhardt,*"Mechanisms of nanostructural and morphological evolution of CeO₂ functional films by chemical solution deposition"* Nanotechnology **16**, 1809 (2005)

71. J.Gazquez, F.Sandiumenge, M.Coll, A.Pomar, N.Mestres, T.Puig, X.Obradors, Y.Kihn, M.J.Casanove, and C.Ballesters,*"Precursor evolution and nucleation mechanism of YBa₂Cu₃Oₓ films by TFA metal-organic decomposition"* Chemistry of Materials accepted (2006)

72. S.Y.Chen and I.W.Chen,*"Temperature-Time Texture Transition of Pb(Zr1-Xtix)O-3 Thin-Films .1. Role of Pb-Rich Intermediate Phases"* Journal of American Ceramics Society **77**, 2332 (1994)

73. S.Y.Chen and I.W.Chen,*"Temperature-Time Texture Transition of Pb(Zr1-Xtix)O-3 Thin-Films .2. Heat-Treatment and Compositional Effects"* Journal of American Ceramics Society , 2337 (1994)

74. J.A.Smith, M.J.Cima, and N.Sonnenberg,*"High critical current density thick MOD-derived YBCO films"* IEEE Trans. on Appl. Supercond. **9**, 1531 (1999)

75. P.M.Mankiewich, J.H.Scofield, W.J.Skocpol, R.E.Howard, A.H.Dayem, and E.Good,*"Reproducible Technique for Fabrication of Thin-Films of High Transition-Temperature Superconductors"* Appl. Phys. Lett. **51**, 1753 (1987)

76. T.Araki and I.Hirabayashi,*"Review of a chemical approach to YBa₂Cu₃O₇-ₓ-coated, superconductors - metalorganic deposition using trifluoroacetates"* Superconductor Science & Technology **16**, R71 (2003)

77. P.C.McIntyre, M.J.Cima, and M.F.Ng,*"Metalorganic Deposition of High-Jc Ba₂YCu₃O₇-ₓ Thin-Films from Trifluoroacetate Precursors Onto (100) SrTiO₃"* J. Appl. Phys. **68**, 4183 (1990)

78. J.Shibata, T.Honjo, H.Fuji, R.Teranishi, T.Izumi, Y.Shiohara, T.Yamamoto, and Y.Ikuhara,*"Transmission electron microscopic studies on the growth mechanism of YBa₂Cu₃O₇-y and Nd₁₊ₓBa₂-ₓCu₃O₇-y films formed by metalorganic deposition method using trifluoroacetates"* Physica C **378-381**, 1039 (2002)

79. W.Wong-Ng, L.P.Cook, J.Suh, I.Levin, M.Vaudin, R.Feenstra, and J.P.Cline,*"Phase Relationships and Phase Formation in the Ba-Y-Cu-F-O-H System"* Materials Research Society Symposium **689**, 337,Boston MA (2001)

80. M.Yoshizumi, I.Seleznev, and M.J.Cima,*"Reactions of oxyfluoride precursors for the preparation of barium yttrium cuprate films"* Physica C **403**, 191 (2004)

81. B.P.Sobolev and N.L.Tkachenko,*"Phase diagrams of BaF_2-(Y,Ln)F_3 systems"* Journal of the Less-Common Metals **85**, 155 (1982)

82. S.Morlens, N.Roma, S.Ricart, A.Pomar, T.Puig, and X.Obradors,*"Thickness enhancement of YBCO superconducting films by use of organic polymeric additives"* , In preparation (2006)

83. N.Romà, S.Morlens, S.Ricart, K.Zalamova, J.M.Moreto, A.Pomar, T.Puig, and X.Obradors,*"Acid anhydrides: a simple route to highly pure organometallic solutions for superconducting films"* Superconductor Science & Technology **19**, 521 (2006)

84. K.Zalamova, N.Romà, A.Pomar, S.Morlens, T.Puig, J.Gázquez, A.E.Carrillo, F.Sandiumenge, S.Ricart, N.Mestres, and X.Obradors,*"Smooth stress relief of trifluoroacetate metal-organic solutions for $YBa_2Cu_3O_7$ film growth"* Chemistry Materials accepted (2006)

85. T.Honjo, Y.Nakamura, R.Teranishi, H.Fuji, J.Shibata, T.Izumi, and Y.Shiohara,*"Growth mechanism of YBCO films in metal organic deposition method using trifluoroacetates"* IEEE Trans. on Appl. Supercond. **13**, 2516 (2003)

86. T.B.Lindemel, J.F.Hunley, J.E.Gates, A.L.Sutton, J.J.Brynestad, C.R.Hubbard, and P.K.Gallagher,*"Experimental and thermodynamic study of nonstoichiometry in $YBa_2 Cu_3O_7$"* Journal of American Ceramic Society **72**, 1775 (1989)

87. V.F.Solovyov, H.J.Wiesmann, and M.Suenaga,*"Growth rate limiting mechanisms of $YBa_2Cu_3O_7$ films manufactured by ex situ processing"* Physica C **353**, 14 (2001)

88. M.Suenaga,*"BaF_2 process for $YBa_2Cu_3O_7$ conductors:promises and challenges"* Physica C **378-381**, 1045 (2002)

89. R.Teranishi, S.Nomoto, J.S.Matsuda, K.Nakaoka, H.Fuji, Y.Aoki, Y.Kito, T.Izumi, Y.Shiohara, A.Sato, T.Watanabe, and Y.Yamada,*"High production rate of crystallization processing in TFA-MOD method for YBCO coated conductors"* , CCA 2004, International Workshop on Coated Conductors for Applications, Japan, Oido, Nov. 2003 (2004)

90. R.Feenstra, T.B.Lindemer, J.D.Budai, and M.D.Galloway,*"Effect of Oxygen-Pressure on the Synthesis of $YBa_2Cu_3O_{7-X}$ Thin-Films by Postdeposition Annealing"* J. Appl. Phys. **69**, 6569 (1991)

91. M.Coll,*"Influència de la interfície en el creixement de capes primes superconductores de $YBa_2Cu_3O_7$"* Treball de recerca, UAB (2005)

92. R.Bormann and J.Nötling,*"Stability limits of the perovskite structure in the Y-Ba-Cu-O system"* Appl. Phys. Lett. **54**, 2148 (1989)

93. E.D.Specht, C.J.Sparks, A.G.Dhere, J.Brynestad, O.B.Cavin, and D.M.Kroeger,*"Effect of oxygen pressure on the orthorhombic-tetragonal transition in the high-temperature superconductor $YBa_2Cu_3O_x$"* Physical Review B **37**, 7426 (1988)

94. V.F.Solovyov, H.J.Wiesmann, M.Suenaga, and R.Feenstra,*"Thick $YBa_2Cu_3O_7$ films by post annealing of the precursor by high rate e-beam deposition on $SrTiO_3$ substrates"* Physica C **309**, 269 (1998)

95. W.Wong-Ng, I.Levin, R.Feenstra, L.P.Cook, and M.Vaudin,*"Phase evolution of $Ba_2YCu_3O_{6+x}$ films during the BaF_2 process"* Superconductor Science & Technology **17**, S548 (2004)

96. L.Fernandez,*"Grain boundary networks in RABiTS based $YBa_2Cu_3O_{7-\delta}$ coated conductors"* PhD. Thesis , IFW, Dresden. Germany (2003)

97. A.Morimoto and T.Shimizu,*"Handbook of Thin Films process technology"* Brisol: Institute of Physics Publishing. Ed. D. A. Glocker and S. I. Shah , A1.5 (1995)

98. R.Hühne, D.Selbmann, J.Eickemeyer, J.Hänisch, and B.Holzapfel,*"Preparation of buffer lalyer architectures for $YBa_2Cu_3O_{7-x}$ coated conductors based on surface oxidized Ni tapes"* Superconductor Science & Technology **19**, 169 (2006)

99. T.Puig, J.C.Gonzalez, A.Pomar, N.Mestres, O.Castano, M.Coll, J.Gazquez, F.Sandiumenge, S.Piñol, and X.Obradors,*"Influence of growth conditions on the microstructure and critical currents of TFA-MOD $YBa_2Cu_3O_7$ films"* Superconductor Science & Technology **18**, 1141 (2005)

100. B.Dam and B.Stauble-Pumpin,*"Growth mode issues in epitaxy of complex oxide thin films"* Journal of Materials Science-Materials in Electronics **9**, 217 (1998)

101. *"Scanning Probe Microscopy and Spectroscopy, Theory, Techniques and Applications"* Ed. by Dawn Bonnel, Wiley-VCH, New York , 2nd Edition (2001)

102. R.Wiesendanger,*"Scanning Probe Microscopy and Spectroscopy, Methods and Applications"* University Press, Cambridge (1994)

103. D.J.O'Connor, B.A.Sexton, and R.St.C.Smart,*"Surface Analysis Methods in Materials Science"* Springer, Berlin , 175 (2003)

104. J.Chastien,*"Handbook of X-Ray Photoelectron Spectroscopy"* PErkin-Elmer Corp. (1992)

105. D.C.Wagner, A.V.Naumkin, A.Kraut-Vass, J.W.Allisoin, C.J.Powell, and J.R.Rumble,*"NIST X-ray Photoelectron Spectroscopy Database"* http://srdata. nist. gov/xps/ (2003)

106. J.P.Holgado, R.Alvarez, and G.Munuera,*"Study of CeO_2 XPS spectra by factor analysis: reduction of CeO_2"* Applied Surface Science **161**, 301 (2000)

107. J.Z.Shyu, K.Otto, W.L.H.Watkins, G.W.Graham, R.K.Belitz, and H.S.Gandhi,*"Characterization of Pd/Gamma-Alumina Catalysts Containing Ceria"* Journal of Catalysis **114**, 23 (1988)

108. E.Paparazzo and G.M.Ingo,*"On the X-ray induced chemical reduction of CeO_2 as seen with X-ray photoemission spectroscopy"* Journal of Electron Spectroscopy and Related Phenomena **95**, 301 (1998)

109. A.Pfau and K.D.Schierbaum,*"The electronic structure of stroichiometric and reduced CeO_2 surface and XPS, UPS and HREELS study"* Surface Science **321**, 71 (1994)

110. P.Burroughs, A.Hammett, A.F.Orchard, and J.Thornton,*"Satellite Structure in the X-Ray Photoelectron Spectra of some Binary and Mixed Oxides of Lanthanum and Cerium"* Journal of the Chemical Society, Dalton Transactions , 1686 (1976)

111. A.R.Gonzalez-Elipe, A.Fernandez, A.Caballero, J.P.Holgado, and G.Munuera,Journal of Vacuum Science and Technology **11**, 58 (1993)

112. J.Elfallah, L.Hilaire, M.Roméo, and F.Lenormand,*"Effect of surface treatments, phton and electron impacts on the ceria 3d core level"* Journal Electron Spectroscopy and Related Pheomena **73**, 89 (1995)

113. P.J.Goodhew and F.J.Humphreys,*"Electron Microscopy and Analysis"* Taylor & Francis, Second Edition. London (1988)

114. J.I.Goldstein, D.E.Newbury, P.Echlin, D.C.Joy, C.Fiori, and E.Lifshin,*"Scanning Electron Microscopy and X-ray Microanalysis"* Plenum, New York (1981)

115. J.L.Pouchou and F.Pichoir,*"Surface-Film X-Ray-Microanalysis"* Scanning **12**, 212 (1990)

116. G.Herranz,*"Growth mechanisms and functionalities of epitaxial metallic ferromagnetic oxide thin films"* Ph. D. Thesis. U. A. Barcelona-ICMAB,Spain (2004)

117. J.Gazquez,*"TEM investigation of growth mechanisms and microstructure of model YBCO coated conductor architectures deposited by metalorganic decomposition"* , Ph.D. Thesis, UAB, Barcelona, Spain (2006)

118. D.B.Williams and C.B.Carter,*"Transmission electron microscopy. A textbook for Materials Science"* Plenum Press, New York (1996)

119. C.P.Bean,*"Magnetization of Hard Superconductors"* Physical Review Letters **8**, 250 (1962)

120. L.J.van der Pauw,*"A method of measuring the resistivity and Hall coefficient on lamellae of arbitrary shape"* Philips Technical Review **20**, 220 (1958)

121. J.C.Gonzalez,*"Coated conductors and chemical solution growth of YBCO films: a micro -raman study"* Ph. D. Thesis. U. A. Barcelona-ICMAB,Spain (2005)

122. M.E.Brown,*"Introduction to Thermal Analysis: Techniques and Applications"* London, New York. Chapman and Hall (1988)

123. M.W.Rupich, D.T.Verebelyi, W.Zhang, T.Kodenkandath, and X.Li,*"Metalorganic deposition of YBCO films for second-generation high-temperature superconductor wires"* Mrs Bulletin **8**, 572 (2004)

124. P.Y.Chu and R.C.Buchanan,*"Reactive Liquid-Phase Sintering of solution-Derved YBCO superconducting thin-films.Ambient and precursor effects on BaO-CuO Liquid-Phase formation"* J. Mater. Res. **8**, 2134 (1993)

125. M.E.Gross, M.Hong, S.H.Liou, P.K.Gallagher, and J.Kwo,*"Versatile New Metalorganic Process for Preparing Superconducting Thin-Films"* Appl. Phys. Lett. **52**, 160 (1988)

126. A.H.Hamdi, J.V.Mantese, A.L.Micheli, R.C.O.Laugal, D.F.Dungan, Z.H.Zhang, and K.R.Padmanabhan,*"Formation of Thin-Films High-Tc superconductors by Metalorganic Deposition"* Appl. Phys. Lett. **51**, 2152 (1987)

127. C.E.Rice, R.B.Vandover, and G.J.Fisanick,*"Preparation of superconducting thin-films of $Ba_2YCu_3O_7$ by a Novel Spin-on Pyrolysis Technique"* Appl. Phys. Lett. **51**, 1842 (1987)

128. Y.Xu, A.Goyal, J.Lian, N.A.Rutter, I.Shi, S.Sathyamurthy, M.Paranthaman, L.Wang, P.M.Martin, and D.M.Kroeger,*"Preparation of YBCO films on CeO_2-buffered (001) YSZ substrates by a non-fluorine MOD method 804"* Journal of the American Ceramic Society **87**, 1669 (2004)

129. T.Araki,*"Purified Coating Solution and Growth Scheme of the YBCO superconductors in Metal organic Deposition Using Trifluoroacetates"* Bulletin of the Chemical Society of Japan **77**, 1051 (2004)

130. N.Roma, S.Morlens, S.Ricart, K.Zalamova, J.M.Moreto, A.Pomar, T.Puig, and X.Obradors,*"Acid anhydrides: a simple route to highly pure organometallic solutions for superconducting films"* Superconductor Science & Technology **19**, 521 (2006)

131. P.C.McIntyre, R.C.Chiu, M.J.Cima, and W.E.Rhine,Materials Research Society Symposium Proceeding **169**, 743 (1990)

132. P.C.McIntyre, M.J.Cima, J.A.Smith, R.B.Hallock, M.P.Siegal, and J.M.Phillips,*"Effect of Growth-Conditions on the Properties and Morphology of Chemically Derived Epitaxial Thin-Films of Ba2Ycu3O7-X on (001) Laalo3"* Journal of Applied Physics **71**, 1868 (1992)

133. M.Mukaida and S.Miyazawa,*"Preferential Axis Control of $Yba_2Cu_3O_x$ Thin-Film by Quasi-Lattice-Match Engineering"* J. Appl. Phys. **74**, 1209 (1993)

134. O.Castaño,*"Sintesis y caracterización de láminas delgadas superconductoras de altas corrientes críticas de YBCO obtendias por M.O.D."* Ph. D. Thesis. U. A. Barcelona-ICMAB,Spain (2004)

135. S.J.Pennycook, M.F.Chisholm, D.E.Jesson, R.Feenstra, S.Zhu, X.Y.Zheng, and D.J.Lowndes,*"Growth and relaxation mechanisms of YBCO films"* Physica C **202**, 1 (1992)

136. Y.-F.Hsieh, M.P.Siegal, Hull R., and J.M.Phillips,*"Microstructure of epitaxial YBCO thinfilms gron on LAO (001)"* Appl. Phys. Lett. **57**, 2268 (1990)

137. J.S.Matsuda,*"Effects of heat-treatment conditions on microstructure of multi-coating Y123 films deposited by advanced TFA-MOD method"* Physica C **412-414**, 890 (2004)

138. R.Teranishi, H.Fuji, T.Honjo, Y.Nakamura, T.Izumi, Y.Shiohara, J.Shibata, T.A.Yamamoto, T.Ikuhara, and M.Yoshimura,Physica C **378-381**, 1033 (2002)

139. A.Cavallaro,*"Optimisation of CSD buffer layers for YBa₂Cu₃O₇ coated conductor development"* Ph. D. Thesis. U. A. Barcelona-ICMAB,Spain (2005)

140. P.A.Langjahr, T.Wagner, M.Ruhle, and F.F.Lange,*"Thermally induced structural changes in epitaxial SrZrO₃ films on SrTiO₃"* J. Mater. Res. **14**, 2945 (1999)

141. A.Seifert, A.Vojta, J.S.Speck, and F.F.Lange,*"Microstructural instability in single-crystal thin films"* J. Mater. Res. **11**, 1470 (1996)

142. C.Teichert,*"Self-organization of nanostructures in semiconductor heteroepitaxy"* Physics Reports **365**, 335 (2002)

143. B.Voigtländer,*"Fundamental processes in Si/Si and Ge/Si epitaxy studied by scanning tunneling microscopy during growth"* Surface Science Reports **43**, 127 (2001)

144. U.Lüeders, F.Sánchez, and J.Fontcuberta,*"Self-organized structures in CoCr₂O₄ (001) thin films: Tunable growth from pyramidal clusters to a {111} fully faceted surface"* Physical Review B **70**, 045403 (2004)

145. J.C.Nie, H.Yamasaki, and Y.Mawatari,*"Self-assembled growth of CeO₂ nanostructures on sapphire"* Physical Review B **70**, 195421 (2004)

146. M.Coll, J.Gazquez, A.Pomar, T.Puig, F.Sandiumenge, and X.Obradors,*"Stress-induced spontaneous dewetting of heteroepitaxial YBa₂Cu₃O₇ thin films"* Physical Review B **73**, 075420 (2006)

147. V.A.Shchukin and D.Bimberg,*"Spontaneous ordering of nanostructures on crystal surfaces"* Reviews of Modern Physics **71**, 1125 (1999)

148. R.Wördenweber,*"Growth of high-Tc thin films"* Superconductor Science & Technology **12**, R86 (1999)

149. X.Obradors, T.Puig, A.Pomar, F.Sandiumenge, S.Pinol, N.Mestres, O.Castano, M.Coll, A.Cavallaro, A.Palau, J.Gazquez, J.C.Gonzalez, J.Gutierrez, N.Roma, S.Ricart, J.M.Moreto, M.D.Rossell, and G.van Tendeloo,*"Chemical solution deposition: a path towards low cost coated conductors"* Superconductor Science & Technology **17**, 1055 (2004)

150. F.F.Lange,*"Chemical Solution Routes to Single-Crystal Thin Films"* Science **273**, 903 (1996)

151. M.Ohring,*"Materials Science of Thin Films, Deposition and structure"* 2nd Edition, Academic Press, New York , 412-430 (2006)

152. C.J.Lu,*"Type of dissociated misfit dislocation in perovskite films on LaAlO₃"* Appl. Phys. Lett. **85**, 2768 (2004)

153. T.G.Holesinger, P.N.Arendt, R.Feenstra, A.Gapud, E.D.Specht, D.M.Feldmann, and D.C.Larbalestier,*"Optimizing SrTiO₃ films on textured Ni subsstrates using chemical solution deposition"* J. Mater. Res. **20**, 1216 (2005)

154. P.C.McIntyre and M.J.Cima,*"Heteroepitaxial Growth of Chemically Derived Ex-Situ $Ba_2YCu_3O_{7-X}$ Thin-Films"* J. Mater. Res. **9**, 2219 (1994)

155. L.Wu, Y.Zhu, V.F.Solovyov, H.J.Wiesmann, A.R.Moodenbaugh, R.L.Sabatini, and M.Suenaga,*"Nucleation and growth of $YBa_2Cu_3O_x$ on $SrTiO_3$ and CeO_2 by a BaF_2 postdeposition reaction process"* J. Mater. Res. **16**, 2869 (2001)

156. O.Castaño, A.Cavallaro, A.Palau, J.C.Gonzalez, M.D.Rossell, T.Puig, S.Piñol, N.Mestres, F.Sandiumenge, A.Pomar, and X.Obradors,*"Influence of porosity on the critical currents of trifluoroacetate-MOD $YBa_2Cu_3O_7$ films"* IEEE Trans. on Appl. Supercond. **13**, 2504 (2003)

157. B.N.Sun, P.Hartman, C.F.Woensdregt, and H.Schmid,*"Structural morphology of $YBa_2Cu_3O_{7-x}$"* Journal of Crystal Growth **100**, 605 (1990)

158. J.T.Dawley, P.G.Clem, T.J.Boyle, L.M.Ottley, D.L.Overmyer, and E.Siegal,*"Rapid processing method for solution deposited $YBa_2Cu_3O_{7-\delta}$ thin films"* Physica C **402**, 143 (2004)

159. T.Ohnishi, R.H.Hammond, and W.Jo,*"High rate in situ $YBa_2Cu_3O_7$ film growth assisted by liquid phase"* J. Mater. Res. **19**, 977 (2004)

160. H.F.Cheng,*"Influence of the characteristics of a $SrTiO_3$ buffer layer on the superconductivity of laser-ablated $YBa_2Cu_3O_{7-\delta}$ films"* Physica C **230**, 267 (1994)

161. X.D.Wu, D.Kijkkamp, S.B.Ogale, A.Inam, E.W.Chase, P.F.Miceli, C.C.Chang, J.M.Tarascon, and T.Venkatesan,*"Epitaxial ordering of oxide superconductor thin films on $(100)SrTiO_3$ prpeared by pulsed laser evaporation"* Appl. Phys. Lett. **51**, 861 (1987)

162. H.Wang, S.R.Foltyn, P.N.Arendt, Q.X.Jia, J.L.MacManus-Driscoll, L.Stan, Y.Li, X.Zhang, and P.C.Dowden,*"Microstructure of $SrTiO_3$ buffer layers and its effects on superconducting properties of $YBa_2Cu_3O_{7-\delta}$ coated conductors"* J. Mater. Res. **19**, 1869 (2004)

163. T.Otsuki and K.Arita,*"Quantum Jumps in FeRAM technology and Performance"* Integrated Ferroelectrics **17**, 31 (1997)

164. *"Epitaxial Oxide Thin Films II"* Materials Research Society Symposium Proceeding **401**, Edited by J.S.Speck, D.K.Fork,R.W.Wolf and T.Shiosaki. Pittsburg, PA (1996)

165. P.G.Clem, B.A.Tuttle, J.A.Ruffner, R.Brinker, R.W.Schwartz, M.A.Rodriguez, and W.L.Warren,*"Investigation of PZT//LSCO//Pt//Aerogel Thin Film Composites for Uncooled Pyroelectric IR Detectors"* Materials Research Society Symposium Proceeding **541**, 661 (1999)

166. P.Chaudhari, F.K.Legoues, and A.Segmuller,*"The microstructure of high-critical current superconducting films"* Science **238**, 342-344 (1987)

167. M.P.Siegal, P.G.Clem, J.T.Dawley, R.J.Ong, M.A.Rodriguez, and D.L.Overmyer,*"All solution-chemistry approach for $YBa_2Cu_3O_{7-\delta}$-coated conductors"* Appl. Phys. Lett. **80**, 2710 (2002)

168. A.Ayala, T.G.Holesinger, P.G.Clem, V.Matias, Q.X.Jia, H.Wang, S.R.Foltyn, and B.Gibbons,*"Synthesis and Characterization of Cu-Doped SrTiO₃ Powders and Sol-Gel Processed Buffer Layers on IBAD MgO Templates"* IEEE Trans. on Appl. Supercond. **15**, 2703 (2005)

169. T.Watanabe, K.Wada, T.Ohashi, M.Ozaki, K.Yamamoto, T.Maeda, and I.Hirabayashi,*"Advances in surface-oxidation epitaxy processed substrates for YBa₂Cu₃O₇₋d film"* Physica C **378**, 911 (2002)

170. X.Z.Liu, S.M.He, D.J.Wu, K.Y.Duan, and Y.R.Li,*"Heteroepitaxial growth of YBCO/STO thin films for voltage tunable varistors"* Physica C **433**, 147 (2006)

171. C.N.L.Edvardsson, U.Helmersson, L.D.Madsen, Zs.Czigany, L.Ryen, and E.Olsson,*"Formation of secondary phases in YBa₂Cu₃O₇₋d/SrTiO₃ multilayers"* Physica C **304**, 245 (1998)

172. K.Tamura, Y.Yoshida, K.Sudoh, H.Kurosaki, N.Matsunami, I.Hirabayashi, and Y.Takai,*"Influence of the microstructure of the SrTiO₃ buffer layer on the superconducting properties of YBa₂Cu₃O₇₋ₓ films"* Physica C **357**, 1386 (2001)

173. A.Pomar, A.Díaz, M.V.Ramallo, C.Torrón, J.A.Veira, and F.Vidal,*"Measurements of the Paraconductivity in the a-Direction of Untwinned Y₁Ba₂Cu₃O₇₋δ Single-Crystals"* Physica C **218**, 257 (1993)

174. A.Diaz, A.Pomar, G.Domarco, J.Maza, and Vidal.F.,*"Critical current versus normal-state resistivity in granular YBCO"* Appl. Phys. Lett. **63**, 1684 (1993)

175. P.A.Langjahr, F.F.Lange, T.Wagner, and M.Ruhle,*"Lattice mismatch accommodation in perovskite films on perovskite substrates"* Acta Materialia **46**, 773 (1998)

176. F.F.Lange,*"Epitaxial grain growth in thin films"* Materials Science Forum **113-115**, 81 (1993)

177. O.Castaño, A.Cavallaro, A.Palau, J.C.Gonzalez, M.Rossell, T.Puig, F.Sandiumenge, N.Mestres, S.Piñol, A.Pomar, and X.Obradors,*"High quality YBa₂Cu₃O₇ thin films grown by trifluoroacetates metalorganic deposition"* Superconductor Science & Technology **16**, 45 (2003)

178. J.C.Gonzalez, N.Mestres, T.Puig, J.Gázquez, F.Sandiumenge, X.Obradors, A.Usoskin, Ch.Jooss, H.C.Freyhardt, and R.Feenstra,*"Biaxial texture analysis of YBa₂Cu₃O₇-coated conductors by micro-Raman spectroscopy"* Physical Review B **70**, 094525 (2004)

179. M.S.Bhuiyan, M.Paranthaman, S.Sathyamurhy, T.Aytug, S.Kang, D.F.Lee, A.Goyal, F.A.Payzani, and K.Salama,*"MOD approach for the growth of epitaxial CeO₂ buffer layers on biaxially textured Ni-W substrates for YBCO coated conductors"* Superconductor Science & Technology **16**, 1305 (2003)

180. Y.A.Boikov, T.Claeson, D.Erts, F.Bridges, and Z.Zvitky,*"CeO₂ compatibility with YBa₂Cu₃O₇₋δ in superconducting-film multilayers"* Physical Review B **56**, 11312 (1997)

181. T.G.Holesinger, S.R.Foltyn, P.N.Arendt, H.Kung, Q.X.Jia, R.M.Dickerson, R.F.Dowden, R.F.DePaula, J.R.Groves, and J.Y.Coulter,*"The microstructure of continuously processed YBa₂Cu₃Oᵧ coated conductors with underlying CeO₂*

and ion-beam-assisted yttria-stabilized zirconia buffer layers" J. Mater. Res. **15**, 1110 (2000)

182. B.Moenter, M.Getta, S.Kreiskott, H.Piel, N.Pupeter, and J.Pouryamout,*"High J_c YBCO films on biaxially textured Ni with oxide buffer layers deposited using evaporation and sputtering techniques"* IEEE Trans. on Appl. Supercond. **13**, 2543 (2003)

183. M.Mogensen, N.M.Sammes, and G.A.Tompsett,*"Physical, chemical and electrochemical properties of pure and doped ceria"* Solid State Ionics **129**, 63 (2000)

184. A.Trovarelli,*"Catalytic properties of ceria and CeO_2-containing materials"* Catalysis Review Science and Engineering **38**, 439 (1996)

185. B.Harrison, A.F.Diwell, and C.Hallet,Platinum Metals Review **32**, 73 (1988)

186. M.Mogensen, D.Lybye, and N.Bonanos,*"Factors controling the oxide ion conductivity of fluorite and perovskite structured oxides"* Solid State Ionics **174**, 279 (2004)

187. A.H.Morshed, M.E.Moussa, M.Bedair, R.Leonard, S.X.Liu, and N.El-Masry,*"Violet/blue emission from epitaxial cerium oxide films on silicon substrates"* Appl. Phys. Lett. **70**, 1647 (1997)

188. S.Tsunekawa, A.Fukuda, and A.Kassuya,*"Blue shift in ultraviolet absorption spectra of monodisperse CeO_{2-x} nanoparticles"* J. Appl. Phys. **87**, 1318 (2000)

189. S.N.Jacobsen, U.Helmersson, R.Erlandsson, B.Skarman, and L.R.Wallenberg,*"Sharp microfaceting of (001)-oriented cerium dioxide thin films and the effect of annealing on surface morphology"* Surface Science **429**, 22 (1999)

190. J.C.Conesa,*"Computer modeling of surfaces and defects on cerium dioxide"* Surface Science **339**, 337 (1995)

191. T.X.T.Sayle, S.C.Parker, and C.R.A.Catlow,*"The Role of Oxygen Vacancies on Ceria Surfaces in the Oxidation of Carbon-Monoxide"* Surface Science **316**, 329 (1994)

192. C.-J.Kim, H.-J.Kim, J.-W.Sun, B.Ki Ji, H.-S.Kim, J.Joo, B.-H.Jun, C.-H.Jung, S.-D.Park, H.-W.Park, and G.-W.Hong,*"Deposition of CeO_2 and NiO buffer layers for YBCO coated conductors on biaxially textured Ni substates by a MOCVD technique"* Physica C **386**, 327 (2003)

193. Y.-M.Chiang, D.Birnie III, and W.D.Kingery,*"Physical Ceramics, Principles for Ceramic Science and Engineering"* Wiley, MIT, New York , 185-217, 371-375

194. G.S.Herman,*"Characterization of surface defects on epitaxial $CeO_2(001)$ films"* Surface Science **437**, 207 (1999)

195. G.S.Herman, Y.J.Kim, S.A.Chambers, and C.H.F.Peden,*"Interaction of D_2O with $CeO_2(001)$ investigated by temperature-programmed desorption and X-ray photoelectron spectroscopy"* Langmuir **15**, 3993 (1999)

196. C.D.Wagner, W.M.Riggs, L.E.Davis, J.F.Moulder, and G.E.Muilenberg,*"Handbook of X-ray Photoelectron Spectroscopy"* **XXX**, Perking-Elmer Corporation,Eden Praire (1979)

197. G.Adachi and N.Imanaka,*"The Binary Rare Earth Oxides"* Chemical Review **98**, 1479 (2004)

198. W.Wong-Ng, Z.Yang, L.P.Cook, Q.Huang, J.A.Kaduk, and J.Frank,*"Chemical interaction between YBCO and CeO_2 at a $P_{O2}=100Pa$"* Solid State Sciences **7**, 1333 (2005)

199. J.S.Matsuda, T.Tokunaga, K.Nakaoka, R.Teranishi, Y.Aoki, H.Fuji, A.Yajima, Y.Yamada, T.Izumi, and Y.Shiohara,*"Transmission electron microscopic studies on crystallization of YBCO films deposited by advanced TFA-MOD method"* Physica C **426-431**, 1051 (2005)

200. M.Paranthaman, C.Park, X.Cui, A.Goyal, D.F.Lee, P.M.Martin, T.G.Chirayil, D.T.Verebelyi, D.P.Norton, D.K.Christen, and D.M.Kroeger,*"YBCO-coated conductors with high engineering current denisty"* J. Mater. Res. **15**, 2647 (2000)

201. D.E.Wesolowski and M.J.Cima,*"Large area quantification of $BaCeO_3$ formation during processing of MOD-derived YBCO films"* , submitted to Journal of Materials Research (2006)

202. V.F.Solovyov, H.J.Wiesmann, and M.Suenaga,*"Nucleation of YBCO on buffered metallic substrates in thick precursor films made by the BaF_2 process"* Supercond. Sci. Technol. **18**, 239 (2005)

203. G.Brorsson, E.Olsson, Z.G.Ivanov, E.A.Stepantsov, J.A.Alarco, Y.A.Boikov, T.Claeson, P.Berastegui, V.Langer, and M.Lofgren,*"$YBa_2Cu_3O_{7-X}$ Films on Yttria-Stabilized ZrO_2 Substrates - Influence of the Substrate Morphology"* J. Appl. Phys. **75**, 7958 (1994)

204. A.Palau,*"Critical Currents and dissipation of grain boundary networks in coated conductors"* Ph. D. Thesis. U. A. Barcelona-ICMAB,Spain (2005)

205. S.Kang, A.Goyal, K.J.Leonard, N.A.Rutter, D.F.Lee, and D.M.Kroeger,*"High Critical current YBCO thick films on improved rolling assisted biaxially textured substrates (RABITS)"* Jouranl of American Ceramics Society **88**, 2677 (2005)

206. H.Jarzina, S.Sievers, Ch.Jooss, H.C.Freyhardt, P.Lobinger, and H.M.Roesky,*"Epitaxial MOD-YSZ buffer layers on IBAD-YSZ substrates"* Superconductor Science & Technology **18**, 260 (2005)

207. Y.-M.Chiang, D.Birnie III, and W.D.Kingery,*"Physical Ceramics, Principles for Ceramic Science and Engineering"* Wiley, MIT, New York , 185-217, 371-375 (1997)

208. R.N.Blumenthal and R.L.Hofmaier,*"Temperature and Compositional Dependence of Electrical-Conductivity of Nonstoichiometric CeO_{2-X}"* Journal of Electrochemical Society **121**, 126 (1974)

209. T.O.Sorensen,*"Thermodynamic Studies of Phase Relationships of Nonstoichiometric Cerium Oxides at Higher Temperatures"* Journal of Solid State Chemistry **18**, 217 (1976)

210. P.L.Chen and I.W.Chen,*"Role of Defect Interaction in Boundary Mobility and Cation Diffusivity of CeO_2"* Journal of American Ceramics Society **77**, 2289 (1994)

211. P.L.Chen and Chen I.W.,*"Grain Growth in CeO_2 :Dopant Effects, Defect Mechanism, and Solute Drag"* Journal of American Ceramics Society **79**, 1793 (1996)

212. F.Esch, S.Fabris, L.Zhou, T.Montini, C.Africh, P.Fornasiero, G.Comelli, and R.Rosei,*"Electron Localization Determines Defect Formation on Ceria Substrates"* Science **309**, 752 (2005)

213. A.Tschöpe,*"Interface Defect Chemistry and Effective Conductivity in Polycrystalline Cerium Oxide"* Journal of electroceramics **14**, 5 (2005)

214. J.W.Cahn,*"Impurity-Drag Effect in Grain Boundary Motion"* Acta Metallurgica **10**, 789 (1962)

215. T.H.Etsell and S.N.Flengas,*"Electrical Properties of Solid Oxide Electrolytes"* Chemical Reviews **70**, 339 (1970)

216. T.Nakagawa, T.Osuki, T.A.Yamamoto, Y.Kitauji, M.Kano, M.Katsura, and S.Emura,*"Study on local structure around Ce and Gd atoms in CeO_2-Gd_2O_3 binary system"* Journal of Syncrotron Radiation **8**, 740 (2001)

217. A.Pomar, M.Coll, A.Cavallaro, J.Gazquez, N.Mestres, F.Sandiumenge, T.Puig, and X.Obradors,*"Interface Control in All Metallorganic deposited coated conductors: Influence on Critical Currents"* J. Mater. Res. **21**, 2176 (2006)

218. M.N.Oliveira, A.M.Botelho do Rego, and O.Conde,*"XPS investigation of $B_xN_yC_z$ coatings deposited by laser assisted chemical vapour desposition"* Surface and coatings technology **100-101**, 398 (1998)

219. F.H.Spedding, K.Gschneidner, and A.H.Daane,*"The crystal structures of some of the rare earth carbides"* Journal of American Chemistry Society **80**, 4499 (1958)

220. G.Praline, B.E.Koel, R.L.Hance, H.I.Lee, and J.M.White,*"X-Ray Photoelectron Study of the Reaction of Oxygen with Cerium 1"* Journal of Electron Spectroscopy and Related Phenomena **21**, 17 (1980)

221. S.Morlens and et al.,to be published (2006)

222. B.C.H.Steele,*"Mass transport in materials incorporated in electrochemical energy conversion systems"* Solid State Ionics **12**, 391 (1984)

223. T.S.Zhang, J.Ma, S.H.Chan, P.Hing, and J.A.Kilner,*"Intermediate-temperature ionic conductivity of ceria-based solid solutions as a function of gadolinia and silica contents"* **6**, 565 (2004)

224. H.Obayashi and T.Kudo,*"Solid State Chemistry of Energy Conversion and Storage, Advances in Chemistry Series"* American Chemical Society, Washington DC **163**, Eds. J.B. Goodenough, M.S. Wittingham, p.316 (1977)

225. K.Knoth,*"La$_2$Zr$_2$O$_7$ and Ce-Gd-O buffer layers for YBCO coated conductors using chemical solution deposition"* Physica C **426-431**, 979-984 (2005)

226. Y.Takahashi, Y.Aoaki, T.Hasegawa, T.Watanabe, T.Maeda, T.Honjo, and Y.Shiohara,*"In-plane textured oxide buffer layer for the TFA-MOD method on <100>{001} ni tapes using MOD process"* Physica C **392-396**, 887-894 (2003)

227. Z.M.Yu, P.Odier, L.ORtega, L.Zhou, P.X.Zhang, and A.Girard,*"La$_2$Zr$_2$O$_7$ films on Cu-Ni alloy by chemical solution deposition process"* Materials Science and Engineering B (2006)

228. D.J.M.Bevan and D.Summerville,*"Handbook on the Physics and Chemistry of Rare Earth"* K. A. Gschneider, L. Eyring (Eds.) North-Holland Physics Publishing, Amsterdam, Oxford, New York, Tokyo , 401 (1979)

229. D.J.Kim,*"Lattice paramters, ionic conductivities, and solubility limits in Fluorite-structure MO$_2$ oxide [M=Hf^{4+},Zr^{4+},Ce^{4+},Th^{4+},U^{4+}]solid solutions]"* Journal of American Ceramic Society **72**, 1415 (1989)

230. Z.Tianishu, P.Hing, H.Huang, and J.Kilner,*"Ionic conductivity in the CeO$_2$-Gd$_2$O$_3$ system (0.05<Gd/Ce<0.4) prepared by oxalate coprecipitation"* Solid State Ionics , 567 (2002)

231. J.M.Ralph and J.A.Kilner,Second Eur. SOFC Forum, Oberrohrdorf, Switzerland **2**, 773, B.Thorstenson (Ed.), (1996)

232. Y.Takahashi, Y.Aoki, T.Hasegawa, T.Maeda, T.Honjo, Y.Yamada, and Y.Shiohara,*"Preparation of YBCO coated conductor on metallic tapes using an MOD process"* Physica C **412-414**, 905 (2004)

233. G.Adachi, N.Imanaka, and Z.C.Kang,*"Binary Rare Earth Oxides"* Ed. Springer (2004)

234. T.Ohashi, S.Yamazaki, T.Tokunaga, Y.Arita, T.Matsui, T.Harami, and K.Kobayashi,*"EXAFS study of Ce$_{1-x}$Gd$_x$O$_{2-x/2}$"* Solid State Ionics **113-115**, 559 (1998)

235. M.F.Yan, R.M.Cannon, and H.K.Bowen,*"Space-Charge, Elastic Field, and Dipole Contributions to Equilibrium Solute Segregation at Interfaces"* J. Appl. Phys. **54**, 764 (1983)

236. D.Y.Wang and A.S.Nowick,*"The "grain-boundary effect" in doped ceria solid electrolytes"* Journal of Solid State Chemistry **35**, 325 (1980)

237. H.W.Chiang, R.N.Blumenthal, and R.A.Fournelle,*"A High-Temperature Lattice-Parameter and Dilatometer Study of the Defect Structure of Nonstoichiometric Cerium Dioxide"* Solid State Ionics **66**, 85 (1993)

238. M.Yashima, K.Morimoto, K.Ishizawa, and M.Yoshimura,*"Difussionless tetragonal-cubic transformation temperature in zirconia-ceriasolid solutions"* Journal of American Ceramics Society **76**, 2865 (1993)

239. P.Fornasiero, E.Fonda, R.Di Monte, G.Vlaic, J.Kaspar, and M.Graziani,*"Relationships between structural/textural properties and redox behavior in Ce$_{0.6}$Zr$_{0.4}$O$_2$ mixed oxides"* Journal of Catalysis **187**, 177 (1999)

240. M.Fernández-García, A.Martínez-Arias, A.Iglesias-Juez, A.B.Hungría, J.A.Anderson, J.C.Conesa, and Soria.J.,Applied Catalysis B:Environemental **31**, 39 (2001)

241. M.Shelef and R.W.McCabe,*"Twenty-five years after introduction of automotive catalysts: what next?"* Catalysis Today **62**, 35 (2000)

242. G.Balducci, J.Kaspar, P.Fornasiero, M.Graziani, M.Saiful Islam, and Gale J.D.,*"Computer Simulation Studies of Bulk Reduction and Oxygen Migration in CeO_2-ZrO_2 Solid Solutions"* Journal of Physical Chemistry B **101**, 1750 (1997)

243. E.Mamontov, T.Egami, R.Brezny, M.Koranne, and S.Tyagi,*"Lattice Defects and Oxygen Storage Capacity of Nanocrystalline Ceria and Ceria-Zirconia"* Journal of Physical Chemistry B **104**, 11110 (2000)

244. G.Vlaic, R.Di Monte, P.Fornasiero, E.Fonda, J.Kaspar, and M.Graziani,*"Redox property-local structure relationships in the ph-loaded CeO_2-ZrO_2 mixed oxides"* Journal of Catalysis **182**, 378 (1999)

245. Y.Gao, G.S.Herman, S.Thevuthasan, C.H.F.Peden, and S.A.Chambers,*"Epitaxial growth and characterization of $Ce_{1-x}Zr_xO_2$ thin films"* Journal of Vacuum Science and Technology A **17**, 961 (1999)

246. A.Goyal, L.Heatherly, and M.Paranthaman,*"RABiTS substrates research and development"* DOE Superconductivity for Electrical System 2005 Annual Peer Review , Washington, DC. (2005)

247. M.W.Rupich, W.Zhang, X.Li, T.Kodenkandath, D.T.Verebelyi, U.Schoop, C.Thieme, M.Teplitsky, J.Lynch, N.Nguyen, E.Siegal, J.Scudiere, V.Maroni, K.Venkataraman, D.Miller, and T.G.Holesinger,*"Progress on MOD/RABiTS 2G HTS wire"* Physica C **412-414**, 877 (2004)

248. H.Fuji, R.Teranishi, Y.Kito, J.S.Matsuda, K.Nakaoka, T.Izumi, Y.Shiohara, Y.Yamada, A.Yajima, and T.Saitoh,*"Progress on TFA-MOD coated conductor development"* Physica C **426-431**, 938 (2005)

249. X.M.Cui, B.W.Tao, J.Xiong, X.Z.Liu, J.Zhu, and Y.R.Li,*"Effect of annealing time on the structure and properties of YBCO films by the TFA-MOD method"* Physica C **xxx**, xxx (2005)

LIST OF PUBLICATIONS

1. X. Obradors, T. Puig, A. Pomar, N. Mestres, F. Sandiumenge, S. Piñol, O. Castaño, A.Cavallaro, A. Palau, J. C. Gonzalez, M. Coll, J. Gazquez '*Chemical Solution Growth of Superconductors: a New Path Towards High Critical Current Coated Conductors*' Physica C **408-410**, 913-914 (2004)

2. X. Obradors, T. Puig, A. Pomar, F. Sandiumenge, S. Piñol, N. Mestres, O. Castaño, M. Coll, A. Cavallaro, A. Palau, J. Gazquez, J. C. Gonzalez, J. Gutierrez, N. Roma, S.Ricart, J. M. Moreto, M. D. Rossell, G. van Tendeloo *'Chemical Solution Deposition: a Path Towards Low Cost Coated Conductors'* Supercond.Sci.Technol. **17**, 1055-1064 (2004)

3. A. Pomar, M. Coll, A. Cavallaro, J. Gazquez, J. C. Gonzalez, N. Mestres, F. Sandiumenge, T. Puig, X. Obradors *'High J_c YBCO Thin Films and Multilayers Grown by Chemical Solution Deposition'* IEEE Trans.on Appl.Supercond. **15**, 2747-2750 (2005)

4. T. Puig, J. C. Gonzalez, A. Pomar, N. Mestres, O. Castaño, M. Coll, J. Gazquez, F. Sandiumenge, S. Piñol, X. Obradors *'The influence of Growth Conditions on the Microstructure and Critical Currents of TFA-MOD $YBa_2Cu_3O_7$ Films'* Supercond.Sci.Technol. **18,** 1141-1150 (2005)

5. M.Coll, J.Gázquez, A.Pomar, T.Puig, F.Sandiumenge and X.Obradors '*Stress induced spontaneous dewetting of heteroepitaxial $YBa_2Cu_3O_7$ thin films*' Phys. Rev. B **73**, 075420 (2006)

6. A. Pomar, A. Cavallaro, M. Coll, J. Gazquez, F. Sandiumenge, T. Puig, X. Obradors, H. C. Freyhardt *'All Chemical YBaCuO Coated Conductors on IBAD/YSZ Substrates'* Supercond.Sci.Technol. **19,** L1-L4 (2006)

7. A. Pomar, M. Coll, A. Cavallaro, J. Gàzquez, J.C. González, N. Mestres, F. Sandiumenge, T. Puig, X. Obradors '*All Chemical High J_c YBCO Multilayers with $SrTiO_3$ as Cap Layer*' J. Mater. Res. **21** (5) 1106-1115 (2006)

8. A. Pomar, M. Coll, A. Cavallaro, J. Gàzquez, N. Mestres, F. Sandiumenge, T. Puig and X. Obradors ' Interface Control in all metalorganic deposited Coated Conductors: Influence on Critical Currents ' J. Mater. Res. **21**,9,2176 (2006)

9.   X. Obradors, T. Puig, A. Pomar, F. Sandiumenge, M. Mestres, M.Coll, A. Cavallaro, N. Romà, , J.Gázquez, J. C. Gonázlez, O. Castaño, J. Gutierrez, A. Palau, K. Zalamova, S. Morlens, A. Hassini, M. Gibert, S. Ricart, J. M. Moretó, S. Piñol, D. Isfort, J. Bock '*Progress towards all chemical superconducting YBCO Coated Conductor*s' Supercond. Sci. Technol. **19** S1-S14 (2006)

10. J.Gázquez, F.Sandiumenge, M.Coll, A. Pomar, N. Mestres, T.Puig and X.Obradors Y. Kihn, M. J. Casanove, and C. Ballesteros *'Precursor evolution and nucleation mechanism of YBa$_2$Cu$_3$O$_x$ films by TFA metal-organic decomposition'* Chemistry of Materials, accepted (2006)